2018-04-12

Indirect Detection of Explosive Vapours by Thermal Dissociation Cavity Ring-Down Spectroscopy

Taha, Youssef Mohamad

UNIVERSITY OF CALGARY

Indirect Detection of Explosive Vapours by Thermal Dissociation Cavity Ring-Down Spectroscopy

by

Youssef Mohamad Taha

A THESIS

SUBMITTED TO THE FACULTY OF GRADUATE STUDIES

IN PARTIAL FULFILMENT OF THE REQUIREMENTS FOR THE

DEGREE OF DOCTOR OF PHILOSOPHY

GRADUATE PROGRAM IN CHEMISTRY

CALGARY, ALBERTA

APRIL, 2018

Abstract

This thesis describes two explosive detection methods capable of detecting explosives indirectly in ambient air. The first of the explosive detection methods utilizes a platinum catalyst heated to 350 °C to catalyze the thermal dissociation of nitroaromatic explosives, such as 2,4,6-trinitrotolune (TNT), to NO_2 prior to detection. The catalytic thermal dissociation (cTD) CRDS was found to have a (1s, 3σ) limit of detection (LOD) of 0.5 ppbv. The LOD was sufficient for the detection of TNT in ambient air but lacked the sensitivity to detect less volatile nitro aromatic explosives such as 2,4,6-trinitrophenylmethylnitramine (Tetryl). Efforts to improve the sensitivity of the instrument via a trap and purge pre-concentration scheme were of limited success largely due to poor sample recoveries from the Tenax traps used.

The second explosive detection technique exploited radicals generated during the thermal decomposition of triacetone triperoxide (TATP), a peroxide explosive, for detection. These radicals were amplified via a peroxide radical chemical amplification scheme (PERCA) that required the addition of NO and a radical chain carrier, commonly CO, to generate NO_2. A modelling study was conducted to assess alternative radical chain carriers as well as the effect of TD on amplification chemistry. Dimethyl ether and ethane were found to be appropriate chain carriers. Additionally, the modelling study suggested that elevated TD temperatures slow down radical chemistry and reduce chemical amplification (CL) while reducing the dependence of CL on relative humidity and radical sinks. A TD-PERCA-CRDS instrument was constructed and its temperature dependent chain length calibrated using peroxyacyl nitrates and peroxy nitric acid. The TD-PERCA-CRDS was found to have a CL up to 69±5 at 250 °C and an LOD (1s, 1σ) of 1.3 pptv. The instrument's relative humidity dependence was reduced compared to that of room temperature PERCA but the instrument was found to suffer from an ozone interference at

temperatures greater than 150 °C. A sample of TATP was synthesized in the lab and its identity and purity established using FTIR. TATP decomposition resulted in an NO_2 signal that was 22±3 times larger than that expected from TATP saturation vapour pressure, and the LOD was 5 pptv.

Acknowledgements

First and Foremost, I would like to thank my supervisor, Dr. Hans D. Osthoff, for his endless guidance, support and encouragement. His work ethic and commitment to sound scientific methodology has been a source of inspiration throughout my graduate studies. Likewise, I would also like to thank my committee members, Dr. Kevin Thurbide and Dr. Yujun Shi, for their continued time and feedback on my thesis project.

Secondly, a special thanks to the Osthoff group members, past and present, whom I have had the pleasure working with over the years. To Travis, Nick, Natasha, Connie, Ting, and Dr. Charles Odame-Ankrah, thank you for the collaborative work environment and the wonderful memories. Our conversations and office discussions have been enlightening and enriching if at times distracting.

Finally, I would like to thank my wife, my family, and my friends, for their encouragement, support, and patience over the years.

Dedication

To Kauthar

and Safiyah,

and to my parents, Mohamad and Awatef.

Table of Contents

List of Tables

List of Figures and Illustrations

List of Symbols, Abbreviations and Nomenclature

Symbol	Definition
ACN	Acetonitrile
AN	Alkyl nitrate
APCI	Atmospheric pressure chemical ionization
AWG	American Wire Gauge
CAPS	Cavity attenuated phase-shift spectroscopy
CIMS	Chemical ionization mass spectrometry
CL	Chain length/amplification factor
CRDS	Cavity ring-down spectroscopy
cTD	Catalytic thermal dissociation
DADP	Diacetone diperoxide
DFT	Discreet Fourier Transform
DNB	1,3-dinitrobenzene
DNT	2,4-Dinitrotoluene
Ea	Activation energy
ECD	Electron capture detector
EGDN	Ethelene glycol dinitrate
FEP	Fluorinated ethylene propylene
FTIR	Fourier Transform Infrared Spectrometer
GC	Gas chromatography
HMTD	Hexamethylene triperoxide diamine
i.d.	Inner diameter

IMS	Ion mobility spectrometry
KPP	Kinetic preprocessor
LIDAR	Light detection and ranging
LIF	Laser-induced fluorescence
LM	Levenberg-Marquardt
LRS	Linear regression of the sum
MCM	Master Chemical Mechanism
MFC	Mass flow controller
MPN	Methyl peroxy nitrate
MS	Mass spectrometry
n.o	Normally open
NASA	National Aeronautic and Space Administration
NB	Nitrobenzene
nc	Normally closed
NI	National Instruments
o.d.	Outer diameter
O_3	Ozone
PA	Picric acid (2,4,6-trinitrophenol)
PAN	Peroxyacyl nitrate
PCU	Pre-concentration unit
PERCA	Peroxy radical chemical amplification
PETN	Pentaerythritol tetranitrate
PFA	Perfluoroalkoxy

PNA	Peroxy nitric acid
PNNL	Pacific Northwest National Laboratories
ppbv	Parts per billion by volume (10^{-9})
ppmv	Parts per million by volume (10^{-6})
pptv	Parts per trillion by volume (10^{-12})
RDX	1,3,5-trinitro-1,3,5-triazinane
RH	Relative humidity
sccm	Standard cubic centimeter
slpm	Standard liter per minute
SPME	Solid-phase microextraciton
TATP	Triacetone triperoxide
TD	Thermal dissociation
Tetryl	Trinitrophenylmethylnitramine
TNB	Trinitrobenzene
TNT	2,4,6-trinitrotoluene
USB	Universal serial bus
ZA	Zero air

Chapter One: Introduction

1.1 History of Explosive Substances

The earliest example of an explosive composition dates back to 220BC when a procedural error during gold ore extraction led to an explosion and the invention of blackpowder.[1] Blackpowder is a mixture of powdered charcoal which contains sulfur and potassium nitrate. Nitroglycerine, much more powerful than its predecessor, was discovered in the 19th century by the Italian professor Ascanio Sobrero. The explosive found widespread usage after the Swedish inventor Immanuel Nobel developed a safer, more reasonable manufacturing process and licensed the construction of plants near mining operations.[1] Since then, more advanced and ultimately safer explosives have been developed for use in mining. Additionally, explosives have since found usage in engineering, construction, quarrying, and devastatingly in military operations. A more detailed history of explosives is provided in chapter one of Akhavan's *The Chemistry of Explosives*.[1]

Chemical explosives may be defined by their ability to undergo rapid highly exothermic chemical reactions over an extremely short period of time generating large amounts of gas.[1] The resultant explosion is characterized by a localized accumulation of heat preceding a sudden release of energy.[1-2] The sudden release of energy and gas is commonly accompanied by a shock wave and or the propulsion of debris.

To undergo such rapid reactivity explosives are commonly characterized by the presence of oxygen in close proximity to oxidizable fuel, mainly carbon and hydrogen.[1-2] Many classes of compounds have been studied that exhibit explosive behaviour. An overview of explosive materials and their classifications is provided below.

1.1.1 Classification of explosives

There have been several attempts in the past to classify explosives based on their chemical compositions and elemental makeup. The renowned Dutch scientist van't Hoff tried developing a classification method in 1909.[1] An 8 class classification was also proposed by Plets in 1953 that attempted to link molecular makeup with explosive power.[1] Neither of these systems was comprehensive, perhaps a result of the large variety of compounds capable of undergoing explosive processes, and none were able to predict the explosive capacity of explosive compounds.

The simplest high-level classification system links explosive capacity to the physical coexistence of oxidizable elements near oxygen in molecules.[1] Many traditional explosives appear to obey this rule (Figure 1.1) including nitro compounds, nitric esters, nitramines, peroxides and derivatives of perchloric acid. Unfortunately, many compounds appear to disobey this basic rule in that they do not contain any oxygen atoms, such as azides, yet show high explosive capacity.

Perhaps due to the lack of a molecular basis for classification, explosives are most commonly classified based on the ease with which they may undergo a detonation process. Here, detonation is defined as the propagation of decomposition, following an initiation phase, at a rate faster than the speed of sound through the unreacted explosive material.[1-2] The pressure increase caused by detonation, as a result of the rapid production and expansion of gases, leads to a shockwave and in turn the sharp, loud noise associated with an explosion event.[1-3] Three classes of explosives are defined by their detonation potential: primary explosives, secondary explosives, and propellants.

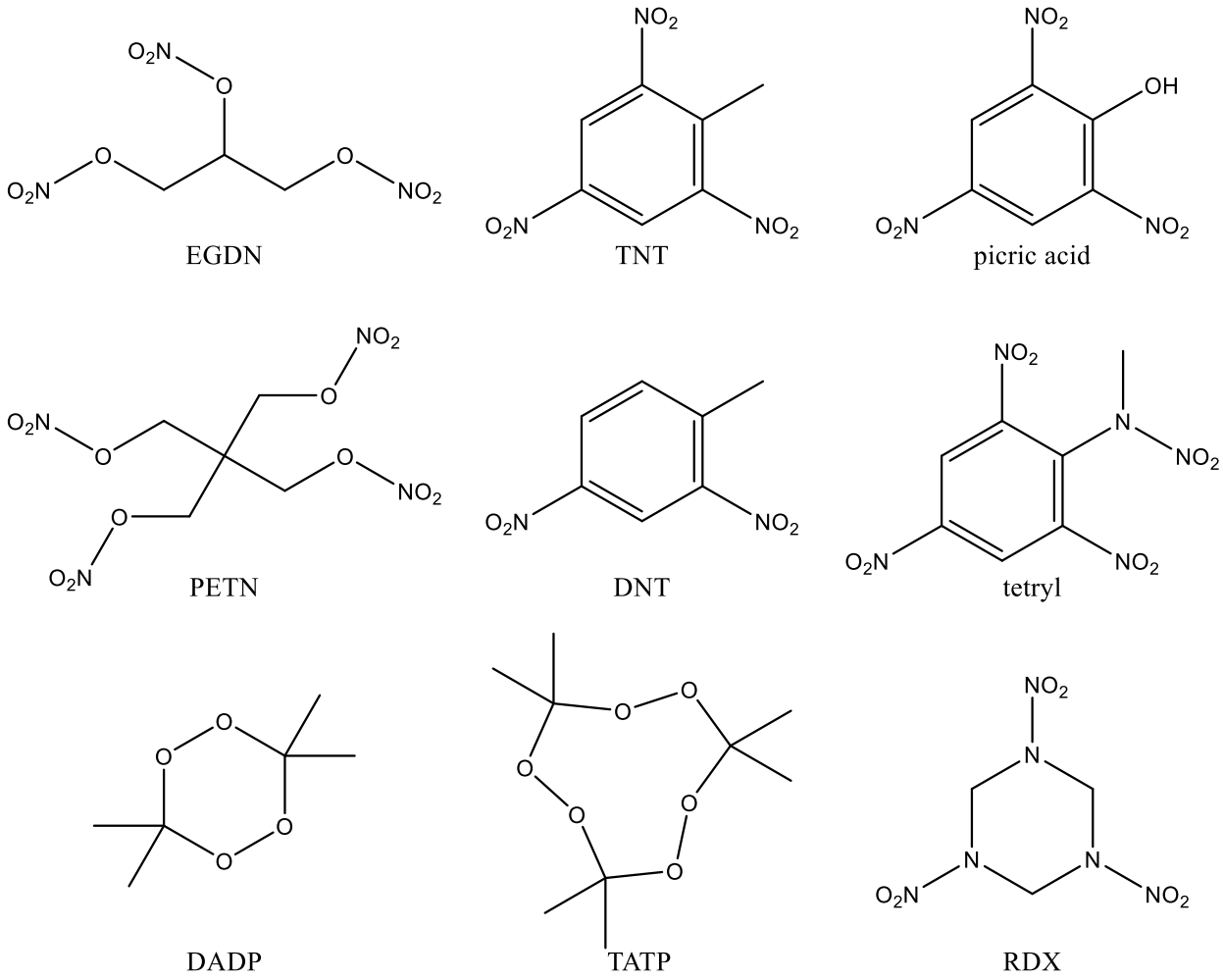

Figure 1.1 Structures of some organic explosive compounds that have oxygen collocated to carbon

Primary explosives are the least stable and undergo rapid transitions from thermal decomposition, either induced by burning, friction or a spark, to detonation. Examples of primary explosives include lead azide ($Pb(N_3)_2$) and mercury fulminate ($Hg(CNO)_2$). Secondary explosives differ from primary explosives in that they are not easily detonated, at least when not confined, through heat and are not shock sensitive. Secondary explosives also tend to be more powerful explosives. The lack of sensitivity of secondary explosive towards detonation translates into their

usage alongside primary explosives that are used to initiate the detonation of the secondary explosive. Secondary explosives, also referred to as high explosives, include compounds most commonly associated with explosions including nitroglycerine (1,2,3-trinitroxypropane), picric acid (2,4,6-trinitrophenol), and 2,4,6-trinitrotoluene (TNT). Finally, propellants are combustible materials that contain within themselves all the material necessary for their combustion. Although they burn with vigour they do not produce a shockwave when unconfined. Thus, they technically do not detonate, instead undergoing what is commonly termed deflagration, a combustion process that does not produce the same sharp, loud bang associated with an explosion.[1, 4] Propellants include formulations such as black powder and ammonium nitrate as well as many commonly used pyrotechnics.

1.1.2 Thermal decomposition of explosives

Due to the large number of chemical species that can undergo explosive decomposition and their varied chemical composition it is difficult to generalize a simple decomposition scheme. Additionally, several explosives undergo decomposition mechanisms that are highly dependent on reaction conditions including pressure and temperature.[1] Nonetheless, several generalized decomposition schemes[1, 5-8] have been proposed to enable the estimation of explosive capacity and volume of gas produced from organic explosives.

A comprehensive exploration of the thermochemistry of explosives is beyond the scope of this thesis, but essentially explosive decomposition normally proceeds to produce carbon dioxide, water and nitrogen gas. Any oxygen imbalance, between the number of carbon and oxygen atoms present in a molecule, leads to the formation of CO during decomposition.[1, 5-6] More modern

approaches also tend to account for a small amount of solid carbon (i.e. soot), hydrogen gas or NO_x ($NO + NO_2$) formed during the decomposition process.[1, 9-10] In addition to shedding light onto the decomposition products these schemes can be used to approximate the thermal decomposition energies observed experimentally. Upon making assumptions about the products of the explosion, a simple Hess' law approach may be used to approximate enthalpy of detonation.[1] Those who employ explosives are more commonly concerned with detonation velocity (the stable velocity of the shock front) and pressure (the pressure that is developed behind the front). [8] The Kamlet-Jacobs method, for example, is also able to approximate these detonation parameters by additionally taking into account the molecular mass of the gaseous products, the number of moles of gaseous products generated per gram of explosive, and the loading density of the explosive.[6] More recently, quantum mechanical calculations have been used to improve predictions of explosive capacity and better constrain thermal decomposition mechanisms and products.[11-13]

1.1.2.1 TATP undergoes an entropic explosion

Although most explosives tend to decompose through pathways that are, at least to a first approximation, captured by the explosive decomposition schemes mentioned above this is not the case for peroxide explosive decomposition. Lacking any nitrogen, triacetone triperoxide (TATP) would be expected to produce a combination of water, carbon dioxide and carbon monoxide as decomposition products. However, analysis of the post blast residue of TATP reveals that 2-3 equivalents of acetone are produced during TATP decomposition.[12, 14] The unexplained acetone ultimately led to a theoretical study by Dubnikova et. al. in 2005 that determined that TATP undergoes stepwise decomposition in what the authors dubbed an entropic explosion.[12] The entropic explosion proceeds via radical intermediates and produces three equivalents of acetone in

succession as well as an ozone (O_3) molecule. A similar decomposition process occurs for diacetone diperoxide (DADP) decomposition as post blast residue from DADP has also been found to contain acetone.[14]

1.1.2.2 Explosive formulations

As has been alluded to earlier, secondary explosives are commonly employed alongside a small amount of primary explosive that acts as a component of detonator, or colloquially a "cap".[2] Additionally, to achieve certain explosive capacity at particular pressures and with particular sensitivity to detonation mixtures of explosives are commonly employed. Furthermore, high heat of combustion additives, such as aluminum, may be added to further increase the energy produced during decomposition. These mixtures in turn complicate decomposition chemistry as well as headspace analysis of explosive vapours.

1.1.3 Explosives pose an increasing threat to society

Improvised explosive devices are finding increased use in attacks against people and infrastructure.[15] Compounding factors include the availability of precursor materials, the relative ease of synthesis and the resultant destructive capacity of the explosive devices.[1-2] Although the use of explosive substances is highly controlled, some precursor materials have become ubiquitous in the modern world (e.g., acetone, citric acid, etc.) and as such remain unregulated.[16] The availability of these precursors along with the continued threat of attacks has led to a strong demand and interest in new devices that can be used for the rapid and reliable detection of explosives.[17-24]

1.2 Aspects of explosive detection

The need for better instrumentation capable of rapid and accurate detection of explosive threats has led to an explosion of research being conducted and published on the topic. This explosion in research is particularly apparent when considering the number[9, 22-27] of review papers that have been published on the topic of explosive detection in the past three years alone. Of these reviews a particularly good overview of the current state of the science is provided by the two-part review published by Brown et. al.[23-24] in Analytical and Bioanalytical Chemistry in 2016. Earlier reviews of note include the 2008 text Aspects of Explosive Detection by Marshal and Oxley[2] and the 2004 seminal review by Moore[19] published in Review of Scientific Instruments.

Most broadly explosive detection techniques may be categorized as bulk and trace detection. Bulk detection aims to find the explosive device itself and usually does so by keying into bulk properties of the explosive device.[2, 9] By far the most common bulk detection method at transportation hubs is X-ray screening. The method relies on the fact that as a general rule the denser an explosive material is the greater its performance; most explosives have a density greater than 1.6 g/cm^3.[1-2] X-ray screening is quite effective but there are, however, exceptions to the high density rule (e.g. nitromethane and triacetone triperoxide).[2] More recently, X-ray diffraction, neutron activation and Raman spectroscopy have been explored for bulk detection of explosives.[24]

Trace detection (trace here being defined as non-detonable quantities)[23] techniques, commonly used in conjunction with bulk detection methods, attempt to detect residues stemming from the handling of the explosive materials. By its nature trace detection is limited by the vapor pressure of explosives along with the limit of detection of available analytical techniques. Many explosives,

particularly those that contain nitrogen, are semi- or non-volatile (see Table 1.1) necessitating the need for instrumentation with sub parts per billion by volume (ppbv) limits of detection.[28-29]

Many modern explosive detection techniques employ pre-concentration, usually in the form of a swab or solid-phase microextraction (SPME),[24, 30-32] to achieve these low detection limits. By swabbing surfaces suspected to have explosive residues on them, collecting explosive residue directly or extracting explosive vapors and allowing volatilization of explosives directly into instrumentation, the low vapor pressure of explosives may be overcome. More recently, novel planar SPME probes have been employed that offer superior collection efficiencies and easier interfacing with common instrumentation.[32] Although effective, and widely used, swabbing is by its nature highly inefficient and time consuming.

Table 1.1 Vapour pressure of some organic explosives at 25 °C.

Explosive	IUPAC name	Vapour pressure (atm)[28]	Vapour pressure (ppbv)[28]
DADP	3,3,6,6-tetramethyl-1,2,4,5-tetraoxane	$(2.4\pm0.9) \times 10^{-4}$	244 000
TATP	3,3,6,6,9,9-hexamethyl-1,2,4,5,7,8-hexaoxonane	$(6\pm2) \times 10^{-5}$	63 100
nitroglycerine	1,3-dinitroxypropan-2-yl nitrate	$(6\pm2) \times 10^{-7}$	645
DNT	1-methyl-2,4-dinitrobenzene	$(4\pm1) \times 10^{-7}$	411
TNT	2-methyl-1,3,5-trinitrobenzene	$(9\pm4) \times 10^{-9}$	9.15
Picric acid	2,4,6-trinitrophenol	9.7×10^{-10}	0.971
PETN	[3-nitrooxy-2,2-bis(nitrooxymethyl)propyl] nitrate	$(1.1\pm0.5) \times 10^{-11}$	0.0107
Tetryl	N-methyl-N-(2,4,6-trinitrophenyl) nitramide	7.4×10^{-12}	0.00741
RDX	1,3,5-trinitro-1,3,5-triazinane	$(5\pm2) \times 10^{-12}$	0.00485

1.2.1 A note on the use of animals and insects for explosive detection

Perhaps most surprising is the remaining utility of service dogs for the detection of explosive vapors. Highly trained dogs can simultaneously detect explosives, as well as illicit drugs, in ambient air and often outperform available analytical instrumentation in terms of limits of detection.[2, 19, 23, 33] However there is some uncertainty associated with which exact odors a dog may be associating with a specific explosive, a matter which could potentially be exploitable with changes in synthetic process or reagents. Furthermore, cross contamination during training could also lead to misidentification of explosive materials beyond training.[34] Although cross-contamination is a common analytical issue, dogs are not analytical instruments, and learned errors may be difficult to identify and correct. Nonetheless, dogs remain the gold standard for explosive detection in many situations.[34]

African giant rats and bees have also been trained in the detection of explosives. In a similar fashion to training dogs, rats and bees may be conditioned to associate explosive vapours with a treat or food.[23] Both rats and bees have been used for detecting explosives in landmines. In the case of bees, tracking bee clustering above a landmine field using light detection and ranging (LIDAR) will indicate landmine locations.[35] Great ingenuity and utility but the same issues that arise with training dogs hold true for both rats and bees.

1.2.2 Analytical methods for trace detection of explosives

Of the numerous analytical approaches that have been attempted for the measurement of explosives, those that are able to detect a substantial subset of explosive compounds are the most useful. Literature examples of molecularly imprinted polymers, metal organic frameworks and immunosensors for the measurement of specific explosive compounds exist and offer great

sensitivity but at the cost of being compound specific.[23] Offering a little bit more utility are colorimetric approaches, particularly those employing colorimetric sensor arrays, that are able to identify a wider array of explosive compounds simultaneously.[36-37] Spectroscopic and more recently smartphone based camera analysis of colorimetric array pallets and the color changes therein offers quantification and ppb limits of detection.[23]

1.2.2.1 Ion detection methods

Offering the most utility for explosive detection are the ion detection methods: ion mobility spectrometry (IMS) and mass spectrometry (MS). Both techniques offer the ability to detect most, if not all, explosive compounds while offering some insight into the chemical structure via either the ion mobility or the mass to charge ratio of the compound.

IMS is currently the most ubiquitous explosive detection method and separates gas phase species based on their ion drift velocity, after acceleration in an electric field, through a drift tube, against an opposing flow of neutral, ambient pressure drift gas.[9, 18, 23, 38-41] Drift times through the tube are on the orders of milliseconds to seconds and depend on the strength of the electric field, the mass to charge ratio of the ion, as well as the physical size of the molecule as it needs to navigate the drift tube opposing the neutral drift gas flow. Direct sampling is possible, as the IMS does not require reduced pressure, yet most IMS instruments are not sensitive enough to detect most explosives which are semi- or non-volatile (Table 1.1). Swabbing and the subsequent thermal desorption act as an initial preconcentrating step. Depending on the ionization method used, fragmentation of certain explosives can complicate IMS peaks. The interpretation of results is further complicated by the broadness of IMS peaks relative to the total drift time. Comparison to extensive and well established IMS libraries is common but false positives are still an issue. To

reduce these false positives IMS has been used after a GC column,[42] adding a second separation dimension albeit with loss of temporal resolution. An alternative approach to overcoming these false positives has been to use a second identification dimension by placing IMS ahead of a MS detector.[43] IMS-MS is quite successful at reducing false positive but the need for MS adds the need for a high vacuum and its associated implications on cost and instrument footprint. Finally, further complicating modern instruments is the need to constantly switch between positive and negative modes to detect TATP and other organic peroxides which may only be detected in positive mode unlike most other explosives (e.g. TNT, PETN, etc.).[18, 41-42]

MS undoubtedly provides the most concrete identification method for the broadest range of explosive vapours. Until recently, the need for implementation of expensive high vacuum systems associated with MS has been prohibitive to uptake in explosive detection.[23] More recent advances in atmospheric pressure ionization methods (e.g., (desorption) electrospray ionization, atmospheric pressure chemical ionization, direct-analysis-in-real-time, etc.) and miniaturized vacuum systems, particularly ion-trap mass spectrometry, have allowed MS to gain traction in explosives detection. The technique appears to be currently undergoing further development and will undoubtedly make up a larger chunk of explosive detection moving forward.

1.2.2.2 Spectroscopic methods

Spectroscopic explosive detection methods also offer reasonable utility, at least theoretically, with many explosive compounds having strong absorption lines in the IR.[23] Attenuated-total-reflectance, particularly in stand-off configurations, has the potential to measure explosive residues without the need for sampling from the surface and surface imaging applications have been demonstrated.[44] Furthermore, employing quantum cascade lasers offers the resolution to measure

the explosive gases directly.[44-46] UV-Visible (i.e., electronic) spectroscopy is not as well researched as explosives tend to have broad and indistinct features complicating detection.[23]

1.2.2.2.1 Cavity ring-down spectroscopy for explosive detection

A promising spectroscopic technique that has recently been employed in explosives detection is cavity ring-down spectroscopy (CRDS). Both direct and indirect explosive detection schemes have been presented.[47-51] The optical absorption technique is well suited for the task due to its high sensitivity, accuracy, and speed.[52-53]

The earliest usage was an UV-CRDS developed by Usachev et al. (2001) that was tuned to TNT in the spectral region of 225-235 nm.[49] The technique did not require preconcentration, and a detection limit of less than 1 ppbv for TNT was demonstrated. More recently, Ramos et al. (2007) developed another UV-CRDS and demonstrated its detection of dinitrotoluene (DNT) and dinitrobenzene (DNB) by scanning the spectral region between 230 and 250 nm.[47] Similarly, no preconcentration was necessary and a detection limit for DNT of 0.1 ppbv was reported. The shortfall of the two UV-CRDS instruments is their inability to detect the majority of nitroaromatic explosives. Another disadvantage of UV-CRDS is their disposition to interferences from other UV-absorbing gases (including the ubiquitous trace gas O_3) raising the possibility of frequent false alarms.

The most successful usage of CRDS for explosive detection is the prototype built by Todd et al. (2002).[51] Their mid-IR CRDS employed a broadly tuneable (6-8 μm) optical parametric oscillator that allowed for the selective detection of several explosives: TNT, RDX, PETN, tetryl and TATP. Preconcentration on a cold finger was necessary to provide a 75 parts per trillion by volume (pptv) detection limit for TNT. More recently, Snels et al. (2010) utilized a near IR-diode

laser to detect TNT and DNT.[48] Although the detection of the two compounds was indeed demonstrated, experiments involved flash heating solid samples for the detection to take place. Although this would provide little utility outside of the lab the instrument was able to differentiate between TNT, 2,4- and 2,6-DNT.

1.2.3 Considerations for Detection of Explosives outside of the laboratory

Detection of explosives outside of the lab must take into account its environment and target. Employment of explosive detection techniques for safety purposes at checkpoints, or at an airport or transportation hub must consider potential interferences and is ultimately limited by the flow of individuals through an indoor environment that although controlled will normally employ circulating air flows. On the other hand, an explosive technique employed by the military in a war zone needs to contend with high background mixing ratios and as such a large dynamic range may be necessary. Finally, in field explosive detection techniques (e.g., screening for land mines) are highly limited by portability and power consumption. For each of these specific roles a variety of techniques and methods may be more well suited.

As alluded to earlier, explosives are commonly used in combination. For example, picratol is a combination of picric acid and TNT while Amatol is a mixture of TNT and NH_4NO_3.[1] Explosive used as components in mixtures may be targeted to detect the presence of explosive mixtures. However, due to the large library of distinct explosive compounds that an explosive composition may draw from, the task of attempting to identify all explosive mixtures remains a challenge.

As explosive detection matures and attempts to intercept explosives before they are placed, armed and detonated, trace detection has become more important. Unfortunately, even with the

renewed research focus on trace detection there still does not exist a single method that is capable of the low detection limits, high selectivity, and portability required for explosive detection in the real world.[23-24]

1.3 Thesis Motivation/Overview

The work outlined in this thesis was motivated by the need to develop improved explosive detection instrumentation. Current explosive detection technologies often fail to provide a real-time measure of the explosive threat. Additionally, commonly employed explosive detection schemes require random grab samples or swabs be obtained. This process is inefficient and leaves those places employing current technology open for potential attack. The current work aimed to develop a real-time explosive sensor based on the indirect detection of explosive vapours in the gas phase. Two commonly encountered classes were targeted for detection, nitroaromatic and peroxide explosives. Both were detected in the form of NO_2 whose concentration was monitored by CRDS. CRDS provides an established rapid, reliable and sensitive trace measurement of NO_2 mixing ratios.

For nitroaromatic explosives, catalytic conversion on a Pt catalyst was explored (chapter 2). Preconcentration of less volatile nitroaromatics on Tenax prior to catalytic thermal dissociation was also attempted (chapter 3). For peroxide explosives, an ethane based thermal dissociation peroxide radical chemical amplification scheme (PERCA) was investigated. PERCA chemistry was modelled and different PERCA chain carriers were considered (chapter 4). An ethane based TD-PERCA-CRDS prototype was built and characterized with peroxy carboxylic nitric anhydride,

peroxy propionic nitric anhydride and peroxy nitric acid (chapter 5). Finally, a TATP sample was synthesized and analyzed using TD-PERCA-CRDS (chapter 6).

Chapter Two: Development of a catalytic thermal dissociation cavity ring-down spectrometer

Part of this chapter has been published in *Chemical Physics Letters* **2013**, *582*, 15-20, doi: 10.1016/j.cplett.2013.07.040.[54]

In this chapter, the design and preliminary testing of a catalytic thermal dissociation cavity-ringdown spectrometer for detection of nitroaromatic compounds will be discussed.

2.1 Catalytic thermal dissociation of nitroaromatic explosives

Many explosives contain one or more nitro functional groups (See Figure 2.1). Some, e.g., nitroglycerine, ethylene glycol dinitrate (EGDN), or pentaerythritol tetranitrate (PETN)) are alkyl nitrates and are hence, at least in principle, detected by thermal dissociation (TD) in a TD-CRDS inlet operated at a temperature of ~450 °C.[55] Most explosives (e.g., 1,3-dinitrobenzene (DNB), 2,4-dinitrotuluene (DNT), 2,4,6-trinitrotoluene (TNT), picric acid (PA), or 2,4,6-trinitrophenylnitramine (Tetryl)), however, are nitroaromatic compounds whose activation energies for thermal dissociation to NO_2 are in the range of 270 to 300 kJ mol^{-1} (Brill and James, 1993)[56] and substantially higher than those of alkyl nitrates, whose activation energies for thermal dissociation are between 150 and 180 kJ mol^{-1}.[57-59] Detection of nitroaromatic explosives by TD-CRDS would require an inlet heated to above 700 °C (calculated from reported activation energies and a residence time of 0.1 s), which is not practical. Furthermore, nitric acid (HNO_3) would dissociate (to NO_2 and OH) at such high temperatures interfering with the measurement of NO_2.[60]

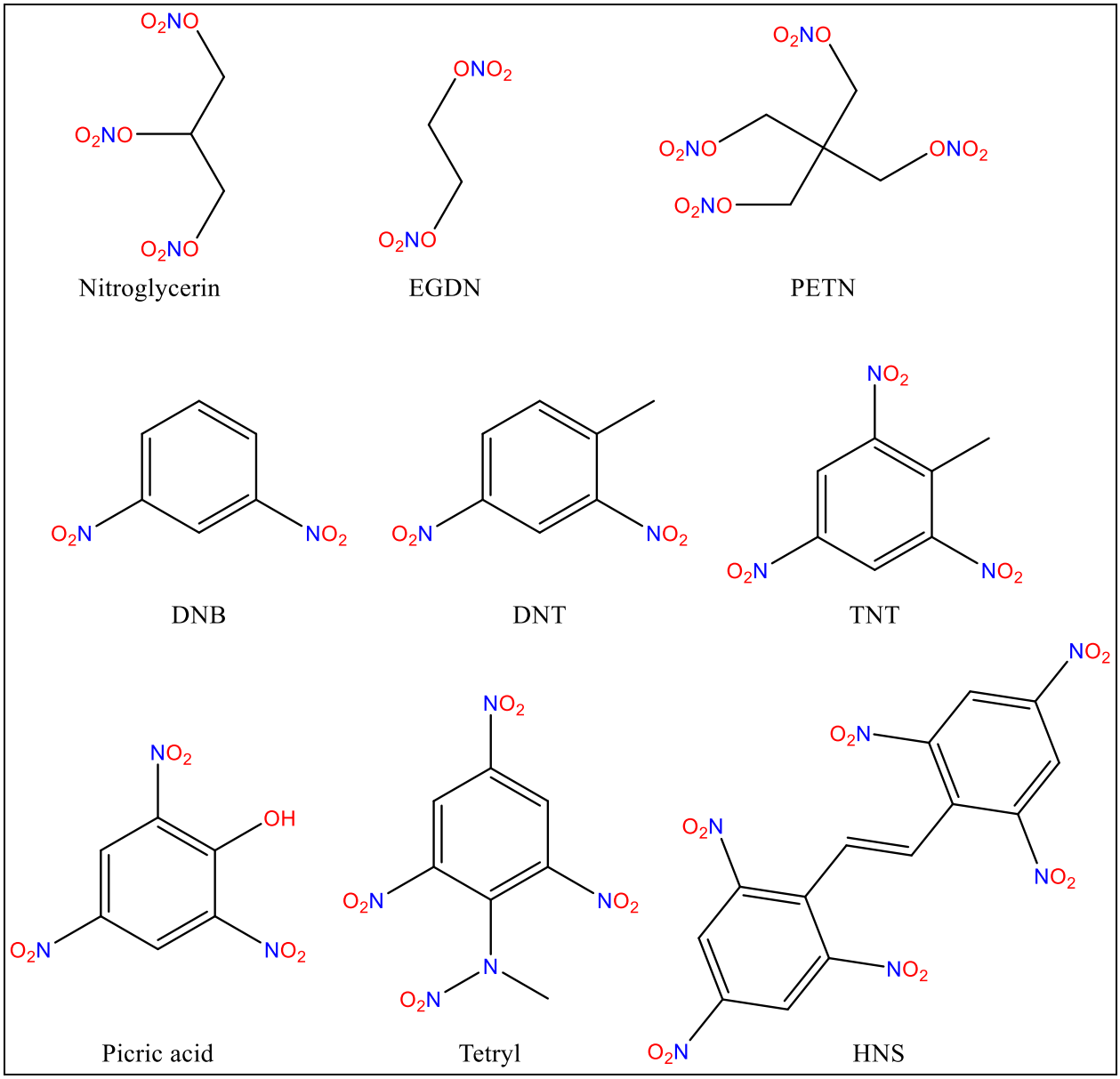

Figure 2.1 Examples of explosive compounds that contain nitro functional groups. Nitroglycerin, Ethylene glycol dinitrate: EGDN, pentaerythritol tetranitrate: PETN, 1,3-dinitrobenzene: DNB, 2,4-dinitrotoluene: DNT, 2,4,6-trinitroluene: TNT, picric acid, N-methyl-N,2,4,6-tetranitroaniline: tetryl, and 1,3,5-trinitro-2-[2-(2,4,6-trinitrophenyl)ethenyl]benzene: HNS.

However, the thermal conversion of nitroaromatic compounds to NO_2 can be catalyzed. For example, Content et al.[61] reported quantitative yields of NO_2 from oxidation of nitroaromatics in the presence of either PdO or PtO_2 heated to 250 °C, e.g., for oxidation of nitrobenzene (NB):

$$4C_6H_5NO_2 + 29O_2 \xrightarrow[\Delta, catalyst]{} 24CO_2 + 10H_2O + 4NO_2 \qquad \text{(Reaction 2.1)}$$

As such, outfitting the TD-CRDS with a catalytic inlet converter should allow for the detection of these nitroaromatic species with catalytic thermal dissociation cavity ring-down spectroscopy (cTD-CRDS). The CRDS used in this work was constructed by a previous member of the Osthoff group. Details including schematics of the CRDS are shown in section 2.1.1 and as Figure 2.1 of the Paul thesis and as Figure 1 of Odame-Ankrah and Osthoff [62].

2.2 Experimental

2.2.1 Converter design and construction

The catalytic converter (Figure 2.2) was constructed from a 54 cm long, 0.635 cm outer diameter (o.d.), 0.476 cm inner diameter (i.d.) quartz tube in which 0.15 to 0.18 g of catalyst was placed. Two types of catalysts were evaluated: Palladium (5% on alumina, Strem) and Platinum(IV) oxide hydrate (>99.9%, Sigma-Aldrich). The catalyst powder was adsorbed onto quartz wool held in place using an 18 cm long, 0.159 cm o.d. quartz tube which was placed inside the larger one and pushed against a perfluoroalkoxy (PFA) Teflon elbow compression fitting (Entegris Fluid Handling). Quartz was chosen as, unlike Pyrex or stainless steel, it does not scrub NO_2 when heated. The converter was heated using 30 American Wire Gauge (AWG) Nichrome wire (~60 Ω) coiled around 24 cm of the quartz tube and held in place by a thermal conductive ceramic adhesive (Resbond 919), in which a K-type thermocouple was embedded. A Teflon filter holder (Cole Parmer) and a 25.4 mm diameter filter (2 μm pore size, Pall Life Sciences) were

placed downstream of the converter to prevent contamination of the CRDS or FTIR sample cell with catalyst.

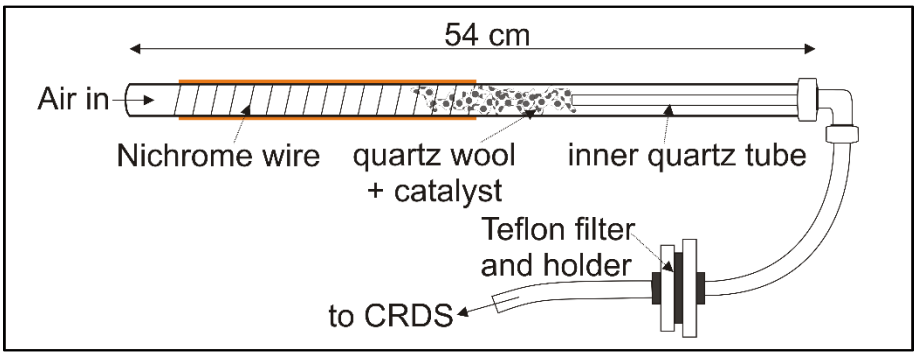

Figure 2.2 Sketch of the quartz catalytic converter.[54]

2.2.2 Determination of nitrobenzene to NO_2 conversion efficiency using FTIR

To determine the conversion efficiency of nitroaromatic compounds to NO_2, the conversion of reactants to gas-phase products was monitored by FTIR. The FTIR was a Bruker Tensor 27 equipped with a Gemini "Venus" multi-pass gas cell with 6.4 m optical path length, Pyrex cell walls, CaF_2 windows, and internal volume of 0.75 L. The cell pressure was monitored using a pressure transducer (Omegadyne PX419-015A5V) connected to a display (Omega CNi32). The FTIR was operated using Bruker's "Opus" software at a resolution of 0.5 cm^{-1}, in Mertz phase correction mode and Blackman-Harris-3-term apodization. Typically, 16 spectra were averaged. Background spectra were taken after the cell had been flushed with ultrapure ("zero" grade) air (Praxair) for at least 30 min. Concentrations of residual IR absorbing gases in the zero air were below the FTIR's detection limit. The sampling compartment outside the sample cell was continuously flushed by a small flow of N_2, but a small portion of the IR beam (next to the globar source and the DTGS detector) was not kept under a controlled atmosphere. Hence, the background

at the dominant atmospheric absorbers (CO_2 and H_2O) drifted slightly following the changes of their concentrations in room air.

Concentrations of gas-phase species were determined using the Beer-Lambert law and infrared absorption cross-sections obtained from the Pacific Northwest National Laboratory (PNNL) vapor phase infrared spectral library (https://secure2.pnl.gov/nsd/nsd.nsf/Welcome).[63] Nitrobenzene (NB) (Aldrich, ACS grade, >99%) was chosen as a model nitroaromatic compound as it is sufficiently volatile to be quantifiable by FTIR and because the infrared absorption cross-sections of NB are in the PNNL database.

The Beer-Lambert law is, strictly speaking, not obeyed when the FTIR resolution is lower than the width of the absorption lines,[64] i.e., for CO_2 and H_2O in this work. The FTIR was therefore calibrated for CO_2 against a commercial Li-COR 7000 CO_2 analyser by sampling room air diluted with zero air. At either 0.5 or 1.0 cm^{-1} resolution, the scatter plots were linear ($r > 0.998$), and the slope was 0.178±0.003 (data not shown). Additionally, off-line experiments verified that the NO_2 mixing ratios measured by FTIR were in quantitative agreement with those observed in parallel by blue diode laser CRDS. Nitroaromatic compounds typically have broad and unresolved absorption features and are hence not affected by this limitation.

NB was placed in a 3-neck trap and eluted with zero air (Figure 2.3). Typically, the flow rate through the trap, set using mass flow controller (MFC) 1, was 5.0 standard cubic centimeters per minute (sccm). The trap output was further diluted using a 1.8 standard liter per minute (slpm) zero air dilution flow using MFC 2. This gave a residence time of ~0.3 s in the converter and of ~0.5 min in the absorption cell.

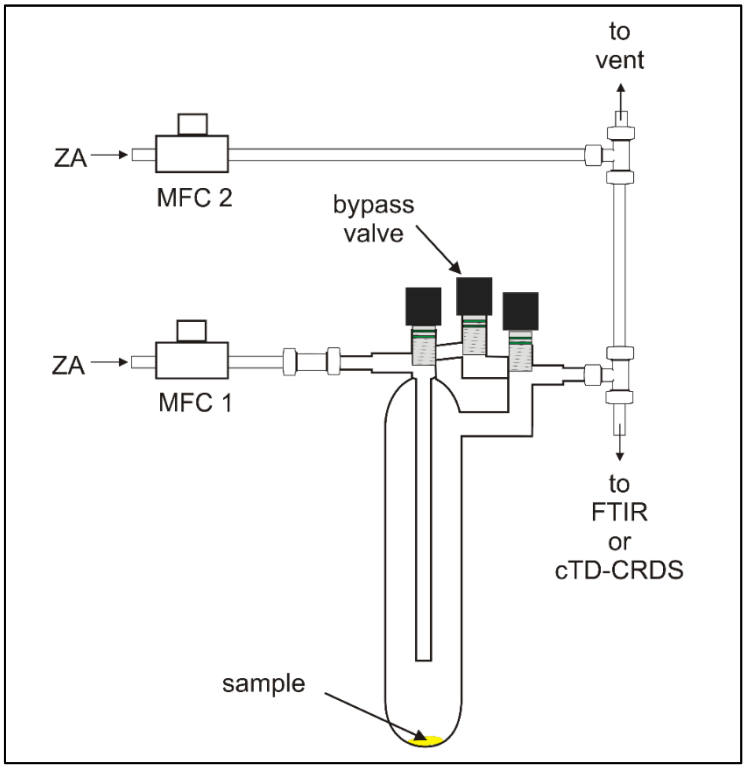

Figure 2.3 Sketch of the sample delivery system. When the FTIR was used, the vent was plugged, MFC = mass flow controller.[54]

In the experiments whose results are described in section 2.3.1 below, the catalyst was initially operated at near-ambient temperature. The trap was flushed for ~10 min to remove room air, after which the concentration of NB was quantified. Then, the temperature of the converter was increased to ~400 °C, and the production of NO_2, CO_2, and H_2O and the disappearance of NB were monitored by FTIR. At the end of the experiment, the concentration of NB was measured again to verify that the trap output had not significantly changed during the experiment.

2.2.3 cTD-CRDS prototype

The cTD-CRDS is a modified version of the 2-channel instrument described by Odame-Ankrah and Osthoff.[62] It hence has the same external dimensions and optical layout and inherited many

components from its predecessor. The main changes from the previous version are: (1) the replacement of the original 662 nm laser and optics with a 405 nm blue diode laser and optics similar to those described by Paul and Osthoff,[65] (2) the implementation of a non-linear Levenberg-Marquardt (LM) fitting routine (described in section 2.2.4 below), and (3) the addition of a catalytic converter inlet as described in section 2.1 to one of the sample channels.

Briefly, the instrument is mounted in an aluminum frame (80/20; 53 cm width × 74 cm depth × 85 cm height). Two 55 cm long CRDS sample channels were constructed from 3/8" (0.953 cm) o.d. and 5/16" (0.794 cm) i.d. FEP Teflon tubing held in place by insulated, built-to-fit aluminum casing. The CRDS mirrors were protected from sampled air via a "purge" flow of zero air generated using 50 μm critical orifices and a backpressure of 20 psi. The CRDS cells, laser and turning optics are aligned such that the laser beam is coupled on-axis. To protect (i.e., isolate) the laser from the front mirrors' back reflections, a polarizing cube and ¼ - wave plates were used (Thorlabs). The laser, external optics, and the two CRDS cells were mounted on a 1' × 2' (0.30 m × 0.61 m) aluminum breadboard (Thorlabs MB1224). Each channel is equipped with a pressure transducer (Omegadyne PX419-015A5V) and a 5 slpm mass flow controller (Celerity 180) connected to a common twin head diaphragm pump (KNF Neuberger N026.1.2ATP). Typically, the cTD-CRDS was operated at a flow rate of 0.80 slpm in the reference channel (which was heated to 250 °C but operated without a catalyst in the experiments presented here) and 0.60 slpm in the catalytic converter channel.

The pressure transducers and mass flow controllers were mounted beneath the optical table and controlled and monitored via a custom-built control box, containing a pair of National Instruments (NI) Universal Serial Bus (USB) 2.0 interface cards (USB-6008 OEM) connected to a laptop running NI LABVIEW. Light exiting the optical cavities was collected by collimating

optics (Thorlabs F220SMA-B) and carried via multimode optical fibers (Thorlabs M25L01) to the photomultiplier tubes (PMTs; Hamamatsu H9433-03MOD) and digitized at a sampling rate of 0.5 MHz per channel (1 MHz aggregate) using a USB 2.0 data acquisition board (NI USB-6251). The communication protocol of the USB data acquisition board effectively limits the data transfer to ~30 cycles per second.[62] Consecutive ring-down traces were thus collected in the on-board memory and transferred (in 0.5 MByte packets of data) to the computer twice per second. Once transferred, the data from consecutive ring-down decays were co-added to 0.5 s data. The ring-down parameters were fitted to the averaged data in between data transfers, while the data acquisition was acquiring new data, and then averaged to 1 s data before presentation.

A Teflon filter holder (Cole Parmer) containing a 2 μm pore size, 25.4 mm diameter Teflon filter (Pall Life Sciences) was placed between the catalytic converter and the CRDS cell. A second filter and filter holder were placed at the tip of the common inlet. All wetted inlet lines and fittings were constructed from PFA or FEP Teflon (supplied by Saint Gobain Plastics or Entegris Fluid Handling).

Number densities of NO_2 were calculated using equation (2.1):

$$N = \frac{R_L}{\sigma}\frac{1}{c}\left(\frac{1}{\tau} - \frac{1}{\tau_0}\right) \qquad \text{(equation 2.1)}$$

Here, σ is the NO_2 absorption cross-section at the laser wavelength (5.8×10^{-19} cm^2 $molecule^{-1}$),[65] R_L = 1.44 is a correction factor to account for the fact that only a fraction of the optical path is occupied by sample gas with the remainder occupied by purge gas, c is the speed of light, and τ and τ_0 are ring-down time constants in the presence and absence of NO_2, respectively. Number densities are converted to mixing ratios using the ideal gas law and are corrected for dilution with purge gas.

2.2.4 Cavity ring-down fitting routines

Once the cells are aligned, the digitized voltage, V(t), can be fitted to the parameters of a first-order exponential equation:

$$V(t) = A \times e^{-t/\tau} + B \qquad \text{(equation 2.2)}$$

Here, A is the signal amplitude, and B is the signal offset. Previously, the instrument used a linear LM fitting algorithm to determine the CRDS cell ring-down times (τ) from a fit of the logarithm of the observed signal,

$$\ln(V(t) - B) = \ln(A) - t/\tau, \qquad \text{(equation 2.4)}$$

and measured the offset (B) directly by averaging data at the "end" of each exponential decay (immediately prior to the next ring-down cycle).[55, 62, 65-66] This approach limits the number of ring-down experiments that can be conducted per second as one has to wait for the signal to fully decay; for this instrument operated with previous linear LM fitting algorithm, that limit was approximately 300 Hz. A greater frequency is highly desirable to achieve greater precision through signal averaging.

For this work, non-linear LM fitting algorithm was programmed to directly determine the parameters A, B, and τ of equation (2.2) from the observed ring-down data. The non-linear LM algorithm is computationally expensive but affordable as there are 0.5 s between data transfer steps. Discreet Fourier transform algorithms DFT-1 and DFT-5 and the "linear regression of the sum" (LRS) algorithm, graciously supplied and described by Everest and Atkinson[67] were also implemented. With any of the new algorithms, effective laser pulse and data acquisition rates of up to 2.5 kHz could be achieved.

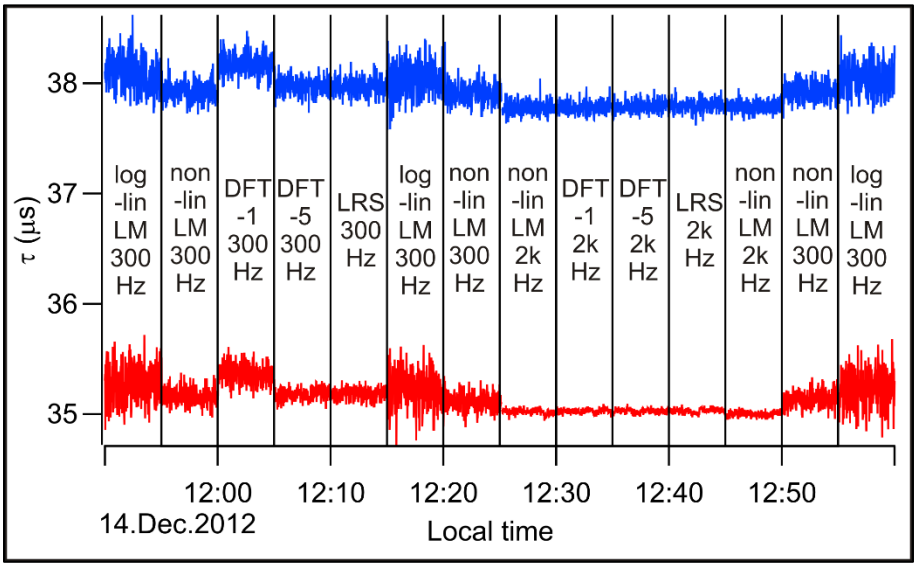

Figure 2.4 Time series of ring down time constants, τ, recovered by the heated sample cell (red) and the ambient temperature cell (blue) using different fitting routines. Log-lin LM = log-linear Levenberg-Marquardt. Non-lin LM = non-linear Levenberg-Marquardt. DFT = Discreet Fourier Transform algorithm. LRS = linear regression of the sum algorithm.

Tables 2.1 and 2.2 and Figure 2.4 show the results of a sample time series of ring-down time constants recovered by different fitting routines while the instrument was sampling zero air with all inlet heaters engaged. The CRDS was operated at either 300 Hz or 2 kHz laser pulse and effective ring-down data acquisition rate. Using the precision of consecutive ring-down time constants, $\sigma(\tau)$, as the main diagnostic of algorithm performance, it was found that the LRS, DFT-5 and non-linear LM fitting algorithms performed approximately equally well and outperformed the previous log-linear LM fitting routine and DFT-1. The latter showed a consistent trend in the residual plot (data not shown) and hence produced somewhat inaccurate ring-down time constants, likely for the same reasons as discussed by Everest and Atkinson[67]. In general, the LRS and DFT-5 are preferred over the non-linear LM fitting algorithm, as the latter is computationally expensive (a fit typically took ~10 ms).

The non-linear LM fitting algorithm was (arbitrarily) chosen for this work, in part because high time resolution was not required and because the non-linear LM algorithm generally produced the least systematic noise in the residual plot. Compared to the previous log-linear LM fitting routine, the improved fitting routines and high number of ring-down decays averaged per second resulted in a considerable gain in the signal-to-noise ratio by a factor of ~6, corresponding to a 1σ precision in the NO_2 mixing ratio as low as ±0.16 ppbv.

Table 2.1. Average ring-down time constants ($\tau \pm \sigma(\tau)$), average standard fit errors ($d\tau$), and NO_2 measurement precision (1σ) while sampling zero air as a function of fitting method and number of ring-down traces averaged per second, as observed in the heated sample cell. The standard fit errors for DFT-1, DFT-5 and LRS were calculated using the method by *Halmer et al.*[68]

Method	Frequency (Hz)	$\tau \pm \sigma(\tau)$ (μs)	$d\tau$ (μs)	$\sigma(NO_2)$ (ppbv)
linear LM [55, 62, 65-66]	300	35.275±0.158	±0.102	±821
non-linear LM (this work)	300	35.158±0.073	n/d	±473
DFT-1 [67]	300	35.366±0.087	±0.004	±526
DFT-5 [67]	300	35.185±0.050	±0.001	±419
LRS [67]	300	35.183±0.050	±0.002	±418
non-linear LM (this work)	2,000	35.021±0.024	n/d	±184
DFT-1 [67]	2,000	35.029±0.020	±0.235	±165
DFT-5 [67]	2,000	35.026±0.021	±0.006	±162
LRS [67]	2,000	35.030±0.022	±0.006	±186

Table 2.2. Average ring-down time constants ($\tau \pm \sigma(\tau)$), average standard fit errors ($d\tau$), and NO_2 measurement precision (1σ) while sampling zero air as a function of fitting method and number of ring-down traces averaged per second, as observed in the ambient temperature cell. The standard fit errors for DFT-1, DFT-5 and LRS were calculated using the method by *Halmer et al*.[68]

Method	Frequency (Hz)	$\tau \pm \sigma(\tau)$ (μs)	$d\tau$ (μs)	$\sigma(NO_2)$ (ppbv)
linear LM [55, 62, 65-66]	300	38.080±0.141	±0.079	±1220
non-linear LM (this work)	300	37.923±0.083	n/d	±563
DFT-1 [67]	300	38.175±0.094	±0.008	±669
DFT-5 [67]	300	37.974±0.074	±0.002	±396
LRS [67]	300	37.969±0.074	±0.002	±390
non-linear LM (this work)	2,000	37.784±0.058	n/d	±308
DFT-1 [67]	2,000	37.781±0.054	±0.210	±283
DFT-5 [67]	2,000	37.790±0.049	±0.007	±291
LRS [67]	2,000	37.793±0.050	±0.006	±283

2.2.5 Detection of 1,3-DNB, 2,4-DNT and 2,4,6-TNT by cTD-CRDS

1,3-DNB (97%) and 2,4-DNT (97%) were purchased from Sigma-Aldrich and used as received. 2,4,6-TNT was purchased as 1 mg / 1 mL solutions in 50% methanol / 50% acetonitrile from Accustandard. In offline experiments, it was established that the cTD-CRDS was sensitive to acetonitrile which was at least partially converted to NO_2 by the catalyst. Therefore, the solvents were evaporated using a gentle stream of O_2 overnight to obtain dry, solid samples of TNT for analysis.

In a typical experiment, the nitroaromatic was placed in a 3-neck flask, which was temperature controlled using an external circulating heater, and eluted and diluted with zero air (Figure 2.3). The flow through the trap (MFC 1) was set to 100 sccm and the dilution flow through MFC 2 to 2.4 slpm. Prior to loading trap with sample, the trap was purged with zero air while the effluent was observed by cTD-CRDS to verify the absence of memory effects from previous experiments. To obtain a stable trap output after loading, it was necessary to keep the trap under flow for several hours prior to analysis and to not modify the trap's bypass valves. Once the trap had been conditioned, it was tee'd into the main inlet, which was flooded with zero air.

In initial experiments (not shown), the cTD-CRDS performance was less reproducible and there was often less efficient conversion of nitroaromatics to NO_2 than had been anticipated based on the FTIR results. This was eventually traced to the fact that the catalyst in the FTIR experiments had been periodically exposed to room air, whereas in the cTD-CRDS experiments, on the other hand, the catalyst was conditioned, over prolonged periods, using (dry) zero air. The catalyst's performance improved considerably once the zero air (used to dilute trap output) was humidified using a bubbler containing deionized water. The bubbler was deployed in all cTD-CRDS experiments shown below.

2.3 Results

2.3.1 Catalytic oxidation of nitrobenzene to NO_2

Figure 2.5 shows FTIR spectra before and after oxidation of NB with PtO_2 catalyst heated to 350 °C. Before the oxidation, the spectrum contains all absorption features expected for NB but also those of trace moisture and CO_2, likely originating from residual room air eluting from the sample trap. When the catalyst was heated to 350 °C (Figure 2.5, bottom), there was no evidence of NB, and only the expected oxidation products, H_2O, CO_2, and NO_2, were observed. This shows that NB had been completely oxidized. In both IR spectra in Figure 2.5, the spectrum is noisy near 1000 cm^{-1}, likely a result of the cut off of the CaF_2 windows.

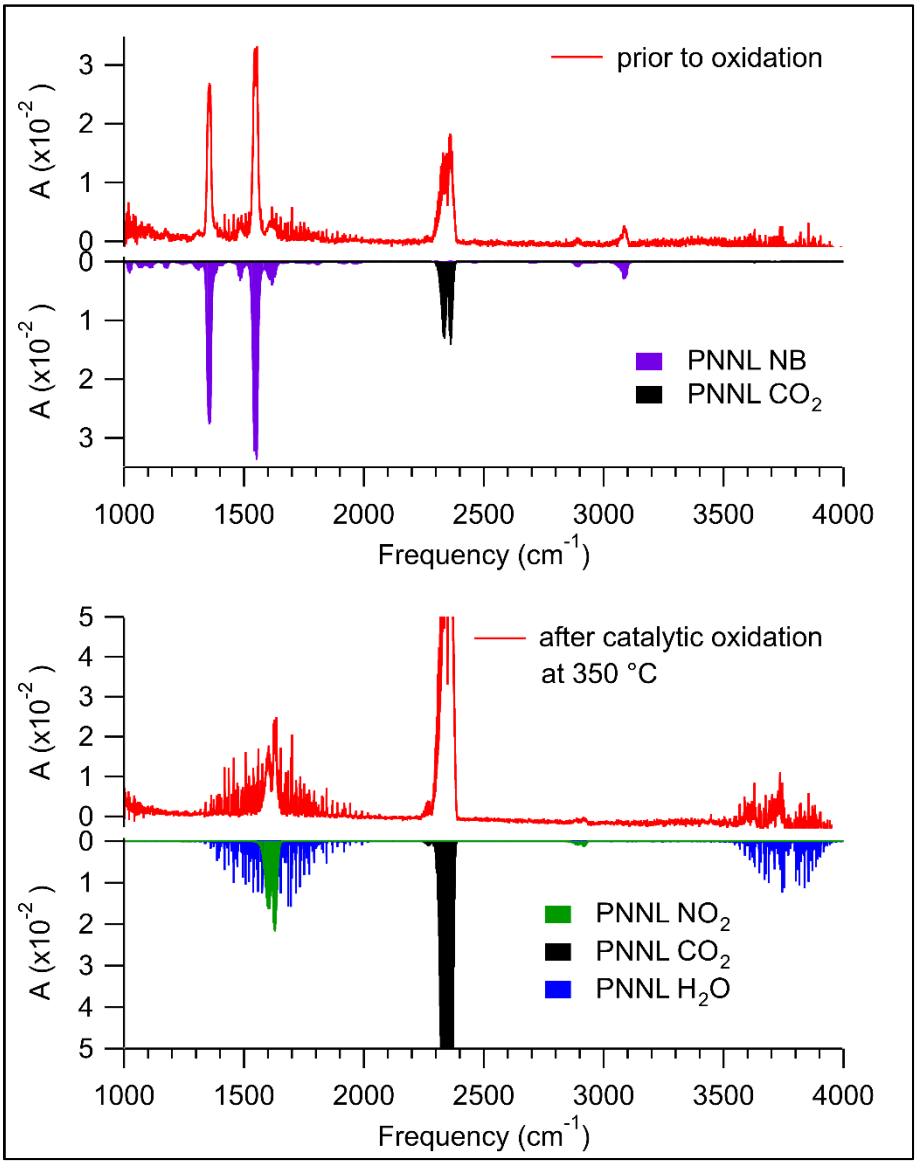

Figure 2.5 Catalytic oxidation of nitrobenzene (NB). (top) FTIR spectrum prior to oxidation. The lower plot (inverted axis) shows the reference spectra of NB, and CO_2 from the PNNL database. (bottom) FTIR spectrum observed after catalytic oxidation at 350 °C. The PNNL reference spectra of NO_2, CO_2, and H_2O are shown at the bottom.

Figure 2.6 shows a time series of NB and NO_2 mixing ratios, calculated from absorption spectra as shown in Figure 2.5. The NB mixing ratios were (248±26) ppbv before the catalyst was heated, and (220±12) ppbv after the catalyst had been heated and allowed to cool again (the error indicates

the 1σ measurement precision). The NO_2 mixing ratio at catalyst temperatures >250 °C was (245±35) ppbv, consistent with quantitative production of NO_2 (see reaction (2.1) for the stoichiometry of the reaction). This quantitative ratio was reproduced in several experiments conducted over a period of several months. On the other hand, the measured CO_2 mixing ratios were generally not consistent with the expected stoichiometric ratio of 6:1 and often greater than expected, for reasons that are not clear. As other C containing species (such as CO) were not observed by IR, I speculate that variability in the CO_2 background, which is orders of magnitude higher than the concentration being measured, or perhaps CO_2 produced by oxidation of partially oxidized hydrocarbon residues from preceding experiments contributed to variability in the measured CO_2.

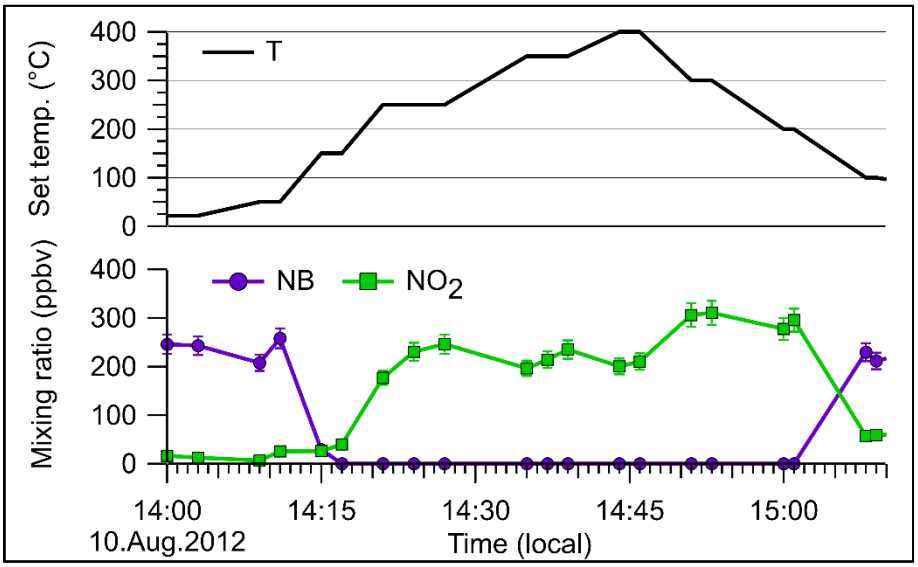

Figure 2.6 Time series of catalytic oxidation of NB as a function of catalyst temperature (shown on top).

Palladium sorbed on alumina was also evaluated with mixed success (data not shown). The IR spectra generally showed less than quantitative yield of NO_2 from NB oxidation, and in some cases revealed the production of NO. Thus, PtO_2 was chosen as the catalyst for the cTD-CRDS.

2.3.2 Real-time detection of explosives by cTD-CRDS

2.3.2.1 Detection of 2,4-DNT

Figure 2.7 shows sample measurements of 2,4-DNT by cTD-CRDS. The source was repeatedly taken offline to determine the baseline ring-down time constants, τ_0 (white underlay). A small amount of room air was usually observed by the CRDS (as spikes in the data) when the source was connected or disconnected. Nitroaromatic compounds are apparently retained on Teflon surfaces, as indicated from the slow (~15 min) approach to a stable signal when the trap is put inline (shown in gray underlay) or taken offline. The same behavior was observed for 1,3-DNB (Figure 2.8) and, to a lesser extent, for 2,4,6-TNT (Figure 2.9).

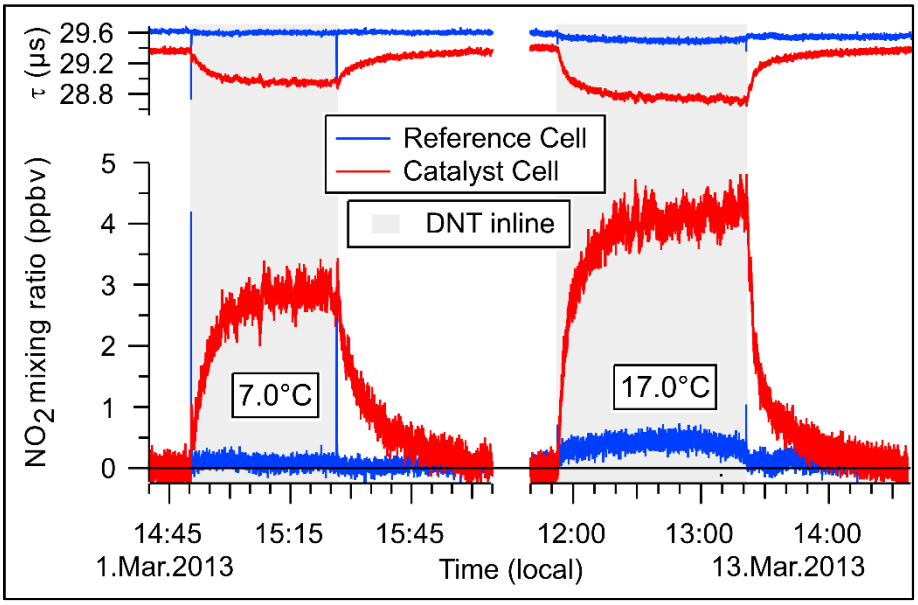

Figure 2.7 Detection of 2,4-DNT by cTD-CRDS. The catalyst channel (shown in red) was operated at 350 °C.

2,4-DNT has saturation vapor pressures of 1.8×10^{-5} Torr at 7.0 °C and 7.5×10^{-5} Torr at 17.0 °C,[69] which correspond to mixing ratios of 28 ppbv and 120 ppbv, respectively. Flow dilution reduces these concentrations by a factor of 14.0 in our experiments. Assuming that the air flowing through the trap saturates with 2,4-DNT, and 2 molecules of NO_2 are produced from each molecule of 2,4-DNT in the converter, 4.0 ppbv of NO_2 at 7.0 °C and 17 ppbv at 17.0 °C are to be expected. The data shown in Figure 2.7 are below those values (2.9±0.2 ppbv at 7.0 °C (73% of 4.0 ppbv) and 4.2±0.2 ppbv at 17.0 °C (25% of 17 ppbv)). A comparison of observed with expected values for 2,4-DNT, 1,3-DNB, and 2,4-6-TNT is shown in Figure 2.10 and is discussed further below.

There was an unexpected response in the reference channel (Figure 2.7, blue) due to absorption by 2,4-DNT, which is slightly yellow in appearance. The reference channel signal implies a 2,4-DNT absorption cross section at 405 nm of ~2.5×10^{-20} cm^2 $molecule^{-1}$. A similar response in the reference channel was observed for 1,3-DNB (Figure 2.8) and 2,4,6-TNT (Figure 2.9).

2.3.2.2 Detection of 1,3-DNB

Figure 2.8 shows detection of 1,3-DNB by cTD-CRDS. This experiment was conducted with the trap at room temperature (23.4 °C). 1,3-DNB was as "sticky" as 2,4-DNT as judged from the slow rise and recovery of the ring-down time constants (~15 min), observed in both the catalytic and reference channels. Further, since a considerable portion of the cTD-CRDS inlet is not heated and hence at or near room temperature, 1,3-DNB must equilibrate with all those surfaces, leading to a gradual approach to a stable concentration. Using the 1,3-DNB vapor pressures reported by *Ferro et al.* [70], the expected 1,3-DNB mixing ratio was 6.0 ppbv, or 12 ppbv of NO_2 if fully converted. Again, the observed mixing ratios are below the maximum value (max. 7.5±0.2 ppbv, or 15±0.3 ppbv if fully converted). The response in the reference channel implies an 1,3-DNB absorption cross-section of ~2.5×10^{-20} cm^2 $molecule^{-1}$ at 405 nm, a value similar to that of 2,4-DNT.

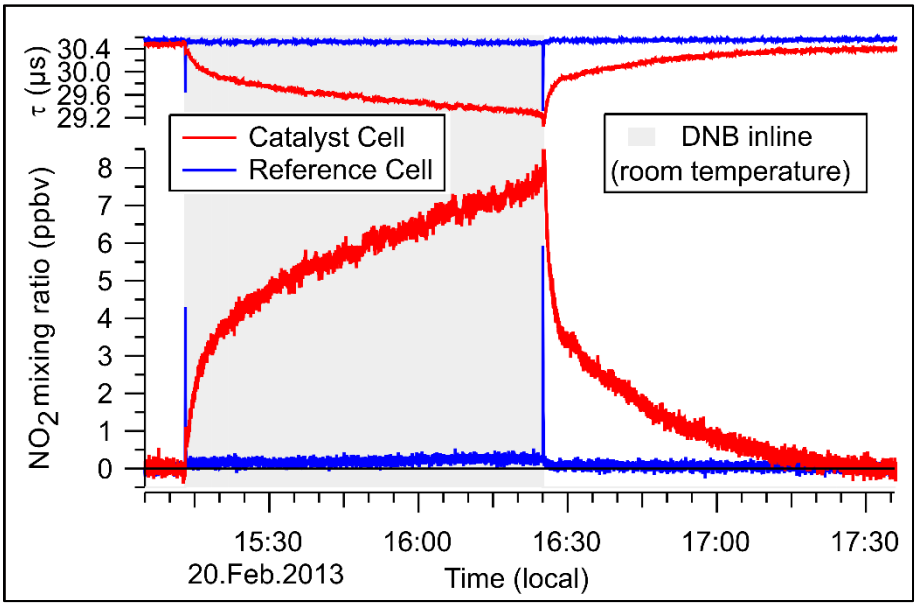

Figure 2.8 Detection of 1,3-DNB by cTD-CRDS. The glass trap containing the 1,3-DNB was at the same temperature as the room, 23.4 °C. The catalyst channel (shown in red) was operated at 350 °C.

2.3.2.3 Detection of 2,4,6-TNT

Figure 2.9 shows a time series of cTD-CRDS demonstrating detection of 2,4,6-TNT. The signal is smaller than for either 1,3-DNB or 2,4-DNT because at the trap temperature in the experiment shown (25.0 °C), 2,4,6-TNT only has a vapor pressure of 6.4×10^{-6} Torr.[69] Assuming equilibration within the trap with the gas flow, this vapor pressure corresponds to a mixing ratio of 0.88 ppbv after dilution. Following conversion to NO_2, a mixing ratio of 2.7 ppbv is expected, which is greater than observed (1.2 ± 0.1 ppbv). There is also a small response in the reference channel, from which the cross-section of 2,4,6-TNT at 405 nm is estimated as 6.6×10^{-20} cm^2 $molecule^{-1}$.

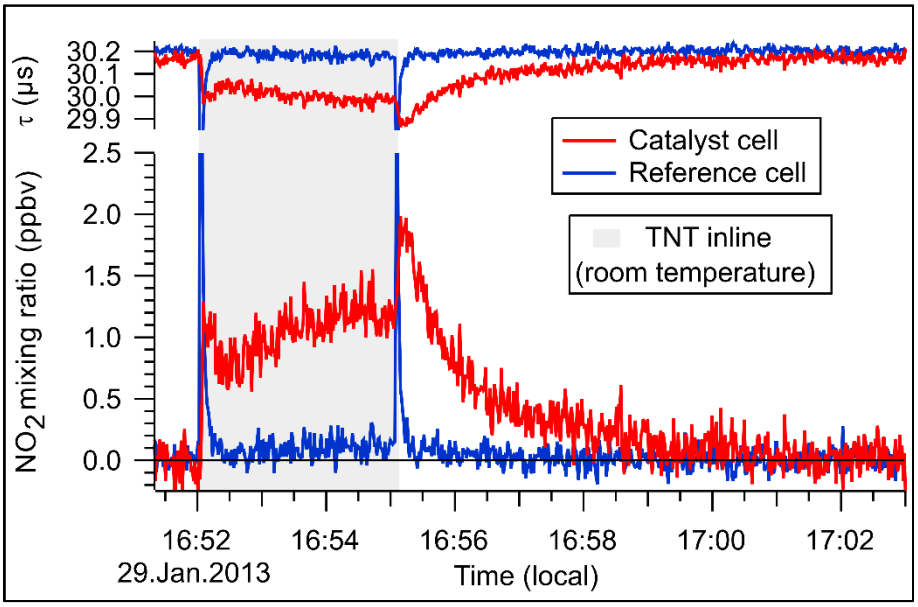

Figure 2.9 Detection of 2,4,6-TNT by cTD-CRDS. The temperature of the glass trap containing the sample was 25.0 °C; the catalyst channel was operated at 350 °C.

2.3.3 Quantitative assessment of catalytic conversion

For this evaluation, it was assumed that the zero-air passing through the glass trap saturated with the nitroaromatic compound before making its way to the CRDS. However, the accuracy of the saturation vapor pressures is not well constrained as the Clausius-Clapeyron parameters reported in the literature for the compounds tested are fairly uncertain,[69-70] with resulting error bars as large as factors of two (the large error bars in Figure 2.10).

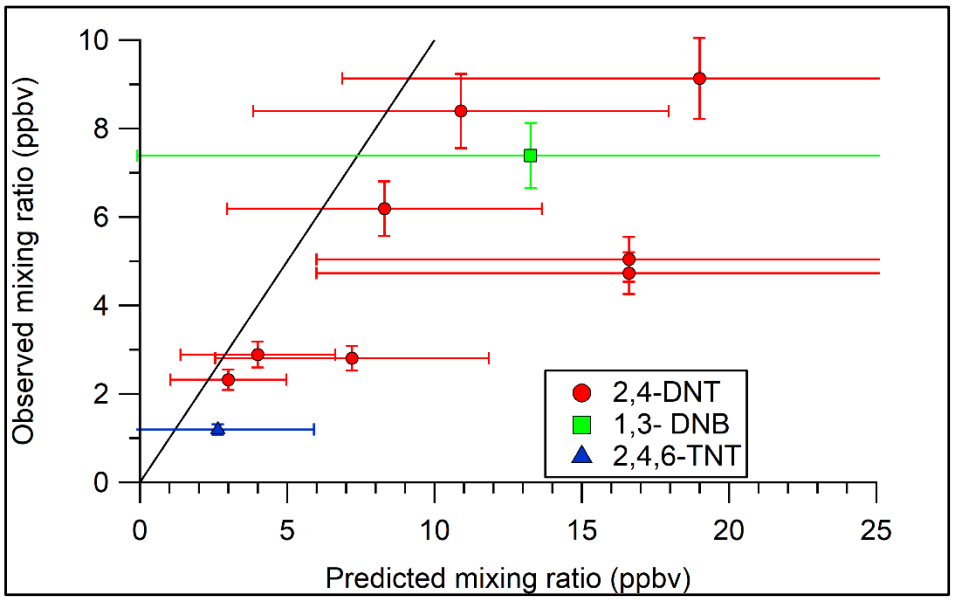

Figure 2.10 Scatter plot of NO_2 mixing ratios observed by cTD-CRDS against mixing ratios predicted from the saturation vapor pressures of 1,3-DNB, 2,4-DNT, and 2,4,6-TNT. The one to one line has been displayed on the plot as well. Error bars are obtained from propagating the error associated with the literature Clausius-Clapeyron parameters.

2.4 Discussion

2.4.1 Catalytic conversion of nitroaromatic compounds to NO_2

The FTIR results show that NB is quantitatively converted by heated Pt(IV)O_2 to NO_2, at least at the ppmv level. With Pd catalyst, formation of NO was observed, which likely stemmed from reduction of NO_2. I speculate that the alumina support may have contributed to NO formation, as we observed partial loss of NO_2 on alumina surfaces in off-line experiments. It was concluded that Pd(0) adsorbed on alumina is less suitable than Pt(IV)O_2 for detection of nitroaromatic compounds by cTD-CRDS. The results presented here are consistent with those by Content et al.[61], who reported similar performance of Pd and Pt catalyst but had not evaluated the catalyst's performance on alumina support. Further, it was found that the presence of trace moisture is needed for efficient catalytic oxidation of nitroaromatic compounds. The dependence of catalyst performance on

humidity was not further investigated, since the catalyst performed reproducibly, for several months, once the humidity of the dilution gas was controlled.

When the catalytic converter was coupled to the CRDS and evaluated at up to three orders of magnitude lower sample concentrations than had been used in the FTIR experiments, its performance was less clear, since the nitroaromatic compounds could no longer be directly monitored, and because the product monitored (NO_2) was no longer specific to a particular molecule. Furthermore, 1,3-DNB, 2,4-DNT, and 2,4,6-TNT are much less volatile than NB and can thus condense within the inlet tubing, leading to significant inlet transmission (e.g., Figure 2.7) and memory effects. To deliver stable and reproducible concentrations of nitroaromatic compounds under these circumstances, the glass traps containing the explosive under investigation was controlled to temperatures below that of the inlet (i.e., below ambient) to prevent condensation of the eluted explosive. In addition, it was necessary to purge these glass traps with zero air for extended periods of time (usually overnight) and to keep the sample traps under continuous flow. In this manner, an evaluation of the catalyst's performance under trace conditions became possible (Figure 2.10).

Figure 2.10 shows that the observed NO_2 mixing ratios correlated with the predicted amounts, but were lower than expected from quantitative conversion of the nitroaromatic compounds. For 2,4-DNT, the data suggest that only between 0.5 and 1.5 molecules of NO_2 were generated per molecule. Similar yields were also observed for 1,3-DNB and 2,4,6-TNT (Figure 2.10). It is unclear whether these results are biased because the trap flow did not achieve saturation vapor pressure or whether the catalyst's performance was reduced. It is highly likely that detection of NO_2 in the CRDS cell itself is quantitative;[55, 65, 71] however, it is possible that the NO_2 produced

from oxidation of the nitroaromatic is partially scrubbed after its catalytic production, for example by reaction of NO_2 with the organic oxidation products (which are highly functionalized). Such scrubbing was not observed when alkyl nitrates were thermally decomposed, which had been rationalized by the short lifetimes of the organic fragments,[55] and would be inconsistent with the (high concentration) FTIR results presented above, but cannot be ruled out at the lower concentrations in the cTD-CRDS experiments where minor reaction pathways may be more dominant. The latter stresses the importance of evaluating the efficiency of catalytic conversion at the concentration levels used, rather than relying on results obtained at high concentrations. Fortunately, quantitative conversion to NO_2 is not required for detection of nitroaromatic explosives at a check point or above land mines.

2.4.2 Comparison of cTD-CRDS with existing CRDS explosive sensors

While detection of nitroaromatic explosives by detection of their thermal decomposition products is not novel (e.g., [50, 61, 72-74]), the combination of catalytic thermal dissociation with CRDS detection of NO_2 presented in this work is new and delivers a faster inherent response (<1 s) and higher sensitivity (<0.5 ppbv, without sample preconcentration) than earlier methods. It is also the first to utilize the visible region of the electromagnetic spectrum for explosives sensing (Table 1.2). Earlier CRDS instruments have utilized the mid-[51] or near-IR,[48] which, unlike the visible region, enables identification of compounds and still achieves sub-ppbv detection limits, in particular when a preconcentrator is used.[51] However, identification of the type of explosives present would only be a secondary objective at a security checkpoint. The UV region has also been utilized.[47, 49] UV-CRDS, is slightly more sensitive (detection limits of 0.1 ppbv without preconcentration have been reported)[47] than the other methods. However, it also does not allow

differentiation amongst explosives and is more prone to atmospheric interferences than the visible region, e.g., due to absorption by ozone, which is a strong absorber whose concentration is highly variable in ambient air.

Table 2.3: Summary of CRDS explosive sensors.

Method	Compound(s) detected	Specific	concentration	LOD (3σ)
UV[49]	TNT	no	none	1 ppbv
Mid-IR[51]	TNT, TATP, RDX, PETN, Tetryl	yes	cold finger	1.2 ppbv (TNT)
Mid-IR[51]	TNT	yes	cold finger	75 pptv
UV[47]	1,2-, 1,3-, 1,4-DNB, 2,4-, 2,6-DNT	no	none	0.1 ppbv
Near-IR[48]	2,4-DNT, 2,6-DNT, TNT	yes	none	75 ng
Visible (cTD-CRDS	1,3-DNB, 2,4-DNT, TNT	no	none	0.5 ppbv

2.4.3 Design Considerations for real world deployment

The cTD-CRDS in its present form suffers from a relatively large dilution factor (of ~14) due to its large sample flow rate requirements. A flow restriction nozzle on the inlet of the cTD-CRDS would aid in lowering these flows, reducing the dilution factor and in turn reducing the instruments limit of detection. It is also necessary to heat the transfer lines and inlet tubing ahead of the catalytic converter to improve the inlet response times. Alternatively, using alternatives to Teflon tubing (e.g., PEEK tubing) could help reduce stickiness on the inlets and improve inlet response times. Finally, preconcentration (as described in Chapter 3) could help improve detection limits while helping reduce inlet transmission problems.

It is important to note that several other factors would also need to be optimized for the instrument to be applicable for real world deployment. For instance, the catalyst's long-term stability needs to be assessed. During this work, the catalyst conversion efficiency was stable for periods of several months when the bubbler was used, which suggests that the current converter design is suitable, or close to. A remaining parameter to be fine-tuned is the quantity of catalyst used, which has not yet been systematically optimized for continuous cTD-CRDS operation.

Interferences from ambient compounds needs to also be examined. At 405 nm, the main optical absorber in the atmosphere is NO_2, which is a highly variable trace gas in the atmosphere. In addition, thermal dissociation of peroxyacyl nitrates (PANs) and alkyl nitrates (ANs)[55, 65] will also be a source of NO_2 in the CRDS. While this has not been evaluated, it is expected that the heated, uncatalyzed reference channel will enable the subtraction of most of these interfering species. Hence, only compounds that dissociate into NO_2 upon catalytic oxidation (and are not dissociated by the elevated temperatures alone) are expected to interfere.

2.5 Conclusion

An explosives sensor based upon the catalytic thermal dissociation of nitroaromatic explosives to NO_2 and subsequent detection using blue diode laser CRDS has been described and detection limits of 0.5 ppbv (1 s data) have been demonstrated. Interferences, although limited by the heated reference channel still need to be fully explored and assessed. Additionally, the instrument lacks the sensitivity required for the less volatile nitroaromatic explosives and would benefit from some form of pre-concentration. Pre-concentration is further explored in chapter 3.

Chapter Three: Measurements of nitroaromatics by cTD-CRDS with purge and trap pre-concentration

3.1 cTD-CRDS limited inadequate limit of detection

As shown in chapter two, the 2-channel cTD-CRDS is capable of real-time indirect detection of the nitroaromatic explosives TNT and DNT via catalytic thermal dissociation in a heated inlet containing PtO_2 hydrate. However, the detection limit of 500 pptv was too high for real-time detection of RDX, PETN, or Tetryl, which are three orders of magnitude less volatile than TNT (Table 3.1). The detection of tetryl, for instance, requires an instrument capable of detecting < 7 pptv.

Table 3.1 Maximum concentration expected for selected explosives.

Explosive	Type	Saturation Mixing Ratios at 298 K.[28] (pptv/ 10^{-12})
TNT	Aromatic	$(9\pm4) \times 10^3$
PETN	Alkyl nitrate	11±5
Tetryl	Aromatic	~7
RDX	Nitramide	4.9±1.6

To overcome the inadequate limit of detection a pre-concentration unit (PCU) utilizing Tenax-TA polymer (poly(2,6-diphenyl-p-phenylene oxide)) as a solvent material was constructed and utilized. Tenax was chosen as a sorbent material as it had been demonstrated to work with organic nitrates[75-77] and has been reported to have a higher adsorption efficiency for TNT and RDX

compared to other sorbents (e.g., Carboxen 1000).[78] Explosive samples were pre-concentrated prior to being sampled by the cTD-CRDS.

3.2 Experimental

3.2.1 Design of the pre-concentration unit

A custom PCU was constructed by bending a ~35 cm long tube into a "U" shape of ~5 cm width and ~15 cm height (Figure 3.1). Four tube materials were tested: two stainless steel tubes with 0.312 cm o.d. (0.160 cm i.d.) and 0.635 cm o.d. (0.365 cm i.d), one Silcosteel tube (Restek, 0.635 cm o.d., 0.365 cm i.d.), and one quartz tube (0.635 cm o.d., 0.365 cm i.d.). A 30 AWG nichrome wire (cut to length to a resistance of 70 Ω) was coiled around each trap for resistive heating. The wire and traps were then coated with a layer of thermally conductive adhesive cement (Resbond 919). A K-type thermocouple was embedded into the cement at the lower end of the "U".

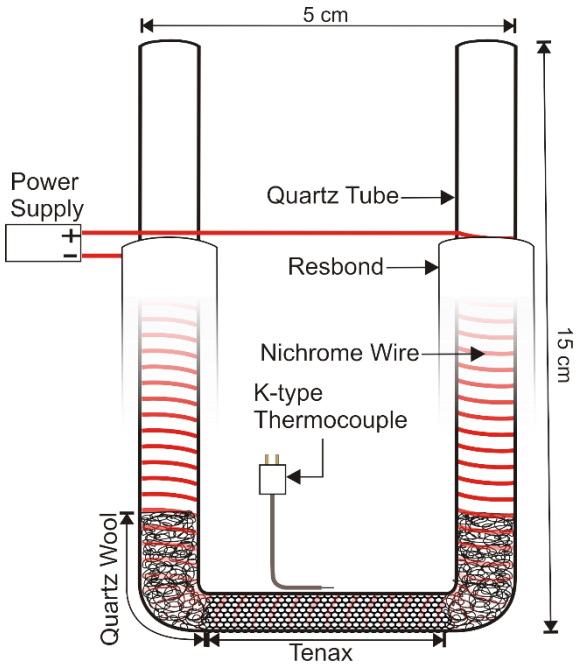

Figure 3.1 Design of the Tenax-TA pre-concentration unit (PCU)

The cement coating was cured at 523 K for several hours in a fume hood as it off gasses an unknown vapor when first heated. The U-tube was then cooled to room temperature and filled with ~0.15 g of Tenax-TA (Sigma-Aldrich, 60-80 mesh (i.e. size selected using mesh with 60 and 80 pores per inch resulting in particles that are ~180 - 250 μm in size)) in the case of the larger traps and ~0.02 g in the case of the smaller o.d. stainless steel trap. Quartz was chosen over Pyrex wool as Pyrex has been observed to reduce NO_2 to NO. The sorbent was packed at the bottom of the U-tube. Quartz wool (length ~ 1 cm) was added to either side to secure the Tenax in place. The sorbent was conditioned under a flow of 60 standard cubic centimeters per minute (sccm) of ECD-grade N_2 (Praxair) at 523 K for 2 hours followed by a flow of ~1 sccm of He at 523 K for 12 hours and capped until use. Between experiments, the U-tube was disconnected and capped to prevent contamination.

The U-tube was connected on one end to the cTD-CRDS inlet and sample delivery setup via 0.635 cm o.d. and 0.476 cm i.d. fluorinated ethylene propylene (FEP) Teflon tubing and polytetrafluoroethylene (PFA) Teflon compression fittings (Entegris Fluid Handling, Figure 3.2). This section of tubing (and fittings) was wrapped with a line heater (Watlow STRETCH-TO-LENGTH® series, not depicted) and heated to 100 °C to prevent re-condensation of high concentrations of sample gasses desorbed from the trap. The other end was connected to a pair of 3-way solenoid operated diaphragm valves (Entegris Galtek® series) whose common ports were connected to the ends of a 5-slpm MFC (purchased from MKS) as shown in Figure 3.2. The normally closed (nc) port of one of two 3-way valves was connected to a line containing ECD-grade N_2 (Praxair) at a pressure of ~5 psi, and the normally open (n.o.) port of the other 3-way valve was connected to vacuum pump (Figure 3.2).

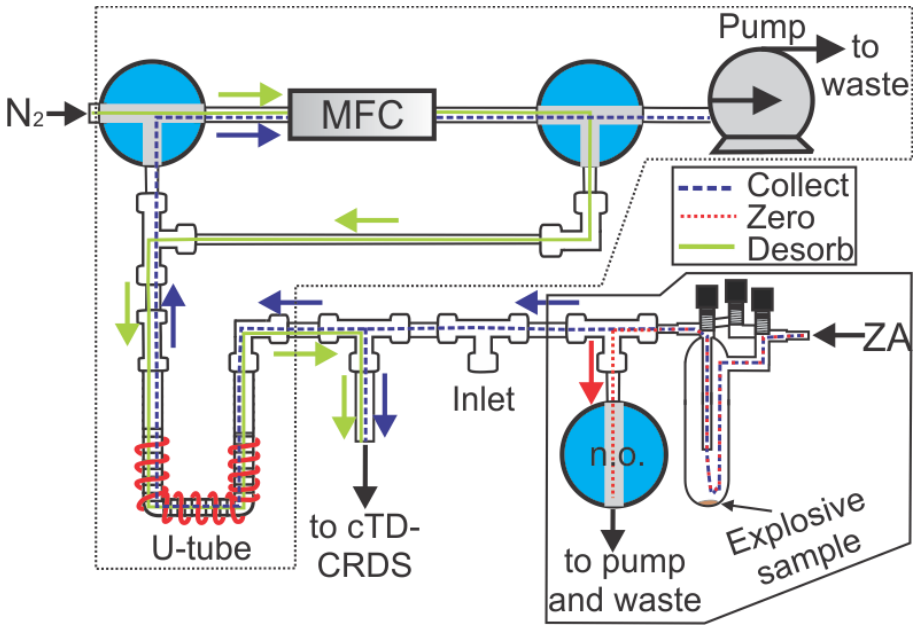

Figure 3.2 Schematic of the pre-concentration unit (PCU, surrounded by dashed line) and sample delivery setup (solid line). ZA = zero air. MFC = mass flow controller. n.o. = normally open. schematic is not to scale.

3.2.2 Generation of explosive vapors

A 3-neck glass vessel (Figure 3.2) was used for sample delivery. Before loading a sample, the vessel was cleaned with acetone (Sigma-Aldrich, HPLC grade) and flushed with O_2 gas at a flow rate of ~50 sccm set using a regulator back pressure of 20 psi and a 50 μm i.d. critical orifice (Lennox Laser) for 24 hours. Before loading of a new sample, the output of the empty glass vessels was analyzed (by cTD-CRDS) to verify that no NO_2 producing residues were present from prior runs.

Solutions containing TNT, Tetryl, RDX, or PETN at a concentration of 1000 μg/mL in a 1:1 mixture of methanol and acetonitrile solvent were obtained from AccuStandard and refrigerated until use. To prepare a sample for experiments, the solution was transferred to a glass vessel which was then flushed with O_2 for ~1 week to remove the solvent and precipitate the explosive. Removal

of acetonitrile was necessary as it gave rise to signal in the cTD-CRDS (chapter 2.2.5). Dried TNT appeared as small, dark yellow globules. Tetryl was yellow and crystalline when dried. RDX was a translucent white powder. PETN was a white crystalline solid.

Sample vapor was eluted from the vessel using ultrapure, or "zero", air (ZA, Praxair) at a flow rate of ~50 sccm set using a regulator back pressure of 20 psi and a 50 μm i.d. stainless steel critical orifice (Lennox Laser). The flow through the vessel was continuous and not interrupted to achieve a stable output concentration. Delivery of the gas was on/off modulated with a 2-way normally open (n.o.) solenoid valve (Cole Parmer EW-01540-10) connected to a vacuum pump. With this setup, sample delivery could be square-wave (i.e., on/off) modulated with a response time of < 1 s.[62]

The main inlet was "overflown" with up to 2 slpm of ZA with the aid of a MFC (MKS, not depicted in Figure 3.2). This overflow diluted the gas concentrations below their saturation pressures and minimized condensation and memory effects within the cTD-CRDS inlet.

3.2.3 Automated pre-concentration procedure

Valve operation was automated using LABVIEW™ software in a cycle that consisted of six intervals: "Sample" (variable duration), "Zero" (30 s), "Flush" (5 s), "Heat" (85 s), "Desorb" (30 s), and "Recover" (240 s). The software allowed the duration of each interval to be changed "on the fly", if desired.

During the "Sample" period, both the cTD-CRDS and the PCU drew air from the inlet (blue arrows, Figure 3.2), i.e., the cTD-CRDS monitored ambient air while the trap was being loaded. This preserved the ability of the cTD-CRDS to monitor more volatile explosives (e.g., TNT[54]) in

real time. The MFC was set to a flow of 200 sccm during all periods; the flow rate was limited by the conductance of air through the sorbent material.

During the "Zero" period, the sample was taken offline (red arrow in Figure 3.2) to determine the ring-down time constants in the absence of optical absorbers (τ_0).

Next, the PCU was back-flushed with ECD grade N_2 (Praxair) to remove the oxygen present in air that would degrade the Tenax polymer when heated.[76] Flow through the trap was then stopped and the trap was heated at a rate of ~10 °C /s to 190 °C.

Once this temperature was reached, N_2 carried the sample to the cTD-CRDS during the "Desorb" stage (green arrows, Figure 3.2). The delayed flow sharpened the desorption peak, improving sensitivity.

During the "recovery" period, an external fan was activated (not shown in Figure 3.2), to speed up recovery of the trap's temperature to ambient. The trap was back-flushed with N_2 during this period.

3.2.4 Detection of nitrogen containing explosives by cTD-CRDS

The explosive vapors were detected using a modified version of the 2-channel cTD-CRDS described in chapter 2. To prevent low vapor pressure compounds from condensing and in turn minimizing (inlet) memory effects and speeding up instrument response (e.g., the earlier version required approximately 2 min to obtain a stable sample signal and about 3 min to achieve a zero) the inlet was externally heated to ~90 °C with a line heater (Watlow).

The thermal decomposition of TNT, PETN, and RDX has been reported to yield NO (in addition to NO_2).[50] Further, partial reduction of NO_2 to NO in the heated quartz tubing was observed on several occasions. The reasons for the reduction of NO_2 are not clear but the intermittency suggests

a matrix effect might be the issue. The reduction of NO_2 by atomic oxygen generated from O_3 is possible.[60] For the PCU cTD-CRDS experiments, a 20 sccm flow of ~1 ppm O_3 in O_2 (which is well in excess of the amount of NO that might be present) was added after the quartz converter and prior to the CRDS measurements cells; this excess O_3 oxidized any NO that may have formed back to NO_2.[79] The O_3 was produced by flowing O_2 past a 185 nm pen ray mercury lamp (Jelight) and splitting the flow evenly between the two channels using a pair of critical orifices (20 μm, Lennox Laser).

3.3 RESULTS

3.3.1 Pre-concentration of TNT

Figure 3.3 shows a sample time series of a TNT pre-concentration cycle.

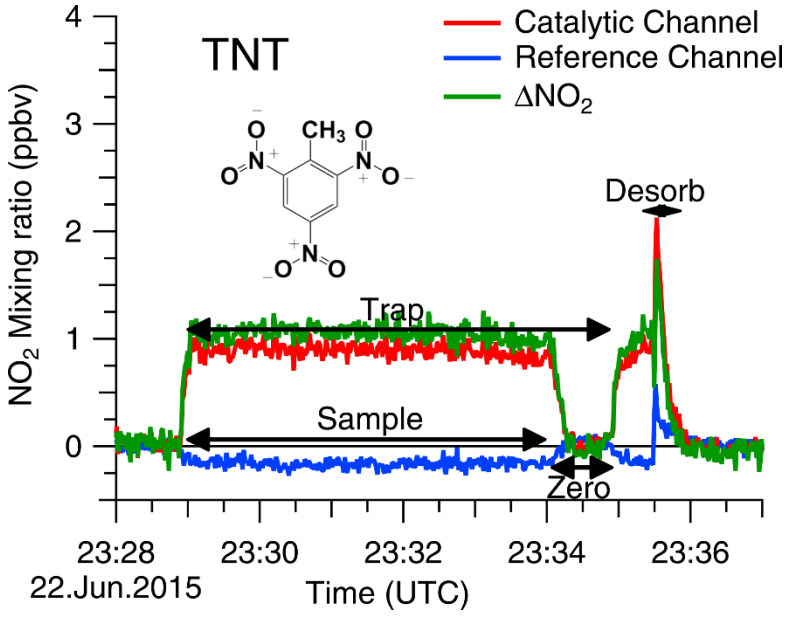

Figure 3.3 Sample time series of TNT pre-concentration. A TNT sample (0.8±0.1 ppbv) was preconcentrated for 300 s before being desorbed and detected by the cTD-CRDS.

In the example presented in Figure 3.3, TNT was preconcentrated for 300 s prior to being desorbed in ~8.5 seconds. During sampling the catalytic channel measured 0.8±0.1 ppbv of TNT from the source. The small negative signal (-0.16±0.05 ppbv) observed in the reference channel during sampling and desorption coincides with pressure changes in the system upon switching flows in the pre-concentration MFC. Additionally, during desorption the reference channel also measured NO_2. To account for the negative offset as well as the reference channel NO_2, the difference between catalytic and reference channels (ΔNO_2) was used for all further analysis.

In the sample time series presented above, the TNT preconcentrated in the desorption stage (area sampled) was integrated and was approximately equal to the average mixing ratio multiplied by the time sampled ((1.05±0.08) ppbv × 300 s = 315 ppbv × s). The signal observed due to desorption (area desorbed), after subtracting the TNT from the source, was integrated and found to be 2.1 ppbv × s. Upon factoring in the rates of the sample flow (200 sccm) over instrument flow (1.1 slpm), the corrected area observed (corrected area desorbed) was 11.3 ppbv × s of desorbed TNT. Only a fraction (3.6±0.3 %) of the sampled TNT was recovered from the trap. Nonetheless, the peak observed during recovery was larger

3.3.1.1 Pre-concentration of TNT as a function of time

For a well-behaved purge and trap system the area desorbed is expected to increase with sample pre-concentration time. Experiments, similar to the example presented in Figure 3.3, were performed using different sample pre-concentration times. Pre-concentration times were randomly selected to avoid a possible consistent memory effect from skewing the data. A plot of the desorbed area, after flow correction, as a function of area sampled (a proxy for sample pre-concentration time given that the TNT signal was relatively stable) is provided in Figure 3.4. The trapping

efficiency remains low even at lower pre-concentration times. Comparing the corrected area desorbed to the area sampled (see above) the trapping efficiency was found to be 16±4 % for TNT when less than 75 ppbv × s (60 s pre-concentration time) was sampled. Above 60 seconds of pre-concentration linearity was lost and the trapping efficiency decreased. As the instrument was capable of obtaining zeros when only ZA was sampled the fit was forced through zero.

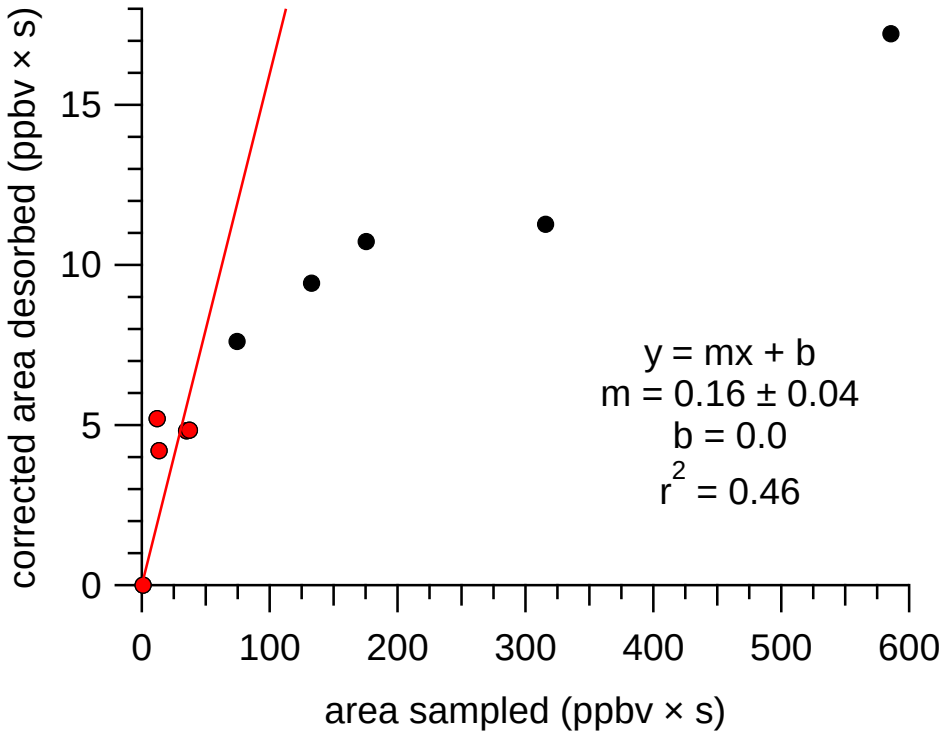

Figure 3.4 Corrected area desorbed as a function of area sampled for TNT. Black data points were excluded from the fit as they are not in the linear portion of the graph.

3.3.2 Conversion efficiency with modified cTD-CRDS

If saturation vapour pressure (9±4 ppbv)[28] was achieved in the 3-neck glass vessel, and factoring in the dilution of the TNT source flow with the instrument flow of 0.046 (50 sccm/ 1091 sccm), 0.41±18 ppbv of TNT are expected to reach the cTD-CRDS inlet. Here 1.05±0.08 ppbv were observed during sampling, providing a ratio of 2.5±1.1. Complete conversion of TNT, to NO_2,

would yield 3 equivalents of NO_2 (if complete conversion is assumed). When the instrument was operated without O_3 addition after the converter lower conversion efficiencies were observed (chapter 2.4.1).

3.3.3 Pre-concentration of PETN, Tetryl, and RDX

Figure 3.5 shows sample time series of pre-concentration and desorption of PETN, Tetryl and RDX. Experimental conditions were the same as those described in section 3.31. In each case there is no response during pre-concentration and a large signal during desorption. A non-zero reference is seen in the reference channel for all desorption peaks.

As the instrument was unable to measure mixing ratios during the sampling phase, an estimate of the sampled area was made possible by assuming that saturation vapour pressure was reached in the 3-neck glass vessel and factoring in flow dilution. For PETN, a saturation vapour pressure of 11±5 pptv is expected. Upon factoring in the dilution of the source flow by the instrument flow, accounting for the 300s sampling time, and a possible 4 NO_2 equivalents per PETN molecule sampled, an upper limit of the sampled area is 605±275 pptv × s (11±5 pptv × 4 × 0.046 (flow dilution factor) × 300 s). The signal observed during desorption was much larger (15.0×10^3 pptv × s) then this upper limit. Similarly, the observed desorption areas for Tetryl and RDX were greater than can be rationalized by the compounds' respective saturation vapor pressures (Table 3.2).

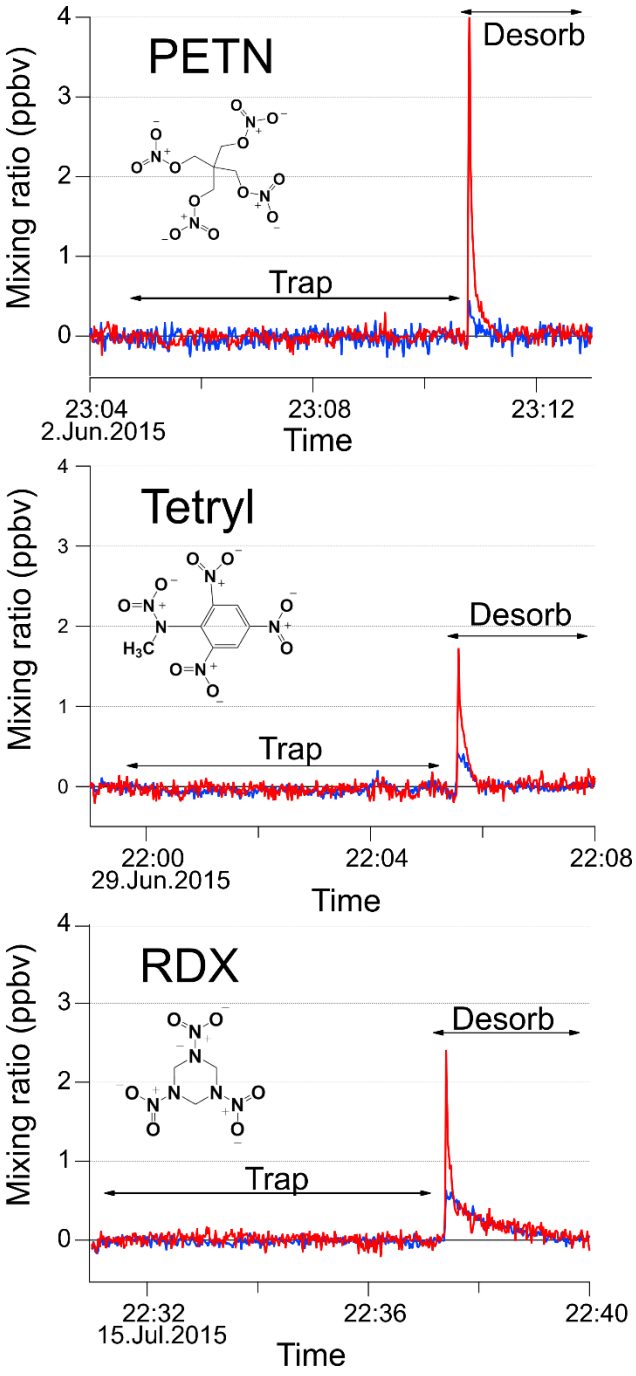

Figure 3.5. Sample time series of (A) PETN, (B) Tetryl, and (C) RDX pre-concentration. Samples were preconcentrated for 300 s before being desorbed and detected by the cTD-CRDS.

Table 3.2 Upper limit of sampled area based on saturation vapor pressure for TNT, PETN, Tetryl and RDX when sampled for 300 s.

Explosive	NO_2 equivalents	Upper limit of sampled area (pptv × s)	Observed desorption area (pptv × s)
PETN	4	605±275	15.0×10^3
Tetryl	4	385	5.4×10^3
RDX	6	404±132	7.6×10^3

3.4 Discussion

3.4.1 Improved cTD-CRDS conversion efficiency

An improved TNT to NO_2 conversion efficiency of 2.5±1.1 was observed with the modified TD-CRDS. As had been noted in chapter 2, quantitative conversion of TNT should yield 3 equivalents of NO_2 but only 1 equivalent of NO_2 was observed during analysis with cTD-CRDS. Titrating the cTD-CRDS inlet with O_3 upon catalytic conversion led to an increase in this efficiency. As O_3 reacts with NO to form NO_2, this confirms suspected[50] NO formation during TNT conversion in the cTD-CRDS inlet either directly or via reduction of NO_2. In either case, adding O_3 to the inlet allowed a greater conversion efficiency to NO_2 and further improved the instrument response to TNT.

3.4.2 Pre-concentration of TNT

Results of TNT pre-concentration on Tenax show disappointing trapping efficiency with only 3.6±0.3 % of the trapped TNT being recovered during desorption. Although Tenax was anticipated to exhibit a high recovery based on previous effective pre-concentration of organic nitrates,[75] it failed to perform adequately with TNT, a nitroaromatic compound. This result is consistent with Wojtas et al.[78] who reported a trapping efficiency of "~10%" for TNT on Tenax after 5 minutes of preconcentration. Furthermore, upon sampling from the Tenax trap, the trap outflow was diluted

prior to reaching the cTD-CRDS. This mismatch between the flows through the Tenax trap, limited by the flow through the packed Tenax, and the instrument flow greatly reduced the signal to noise ratio. Pre-concentration on Tenax failed to provide a signal to noise enhancement while reducing the time resolution of the instrument. The utility of cTD-CRDS for the measurements of TNT is as such very limited.

3.4.2.1 Sample recovery may be influenced by heating temperature/mechanism

The observations presented for TNT in chapter 2 and in section 3.2 above demonstrates that TNT may be converted to NO_2 and NO using the PtO_2 catalyst employed. Brill and Keneth[56] found that the temperature used and the rate at which energy was added to nitroaromatic explosives can affect the decomposition mechanism. Lower temperatures (perhaps similar to those present during desorption) promote pathways with smaller activation energies and more exothermicity.[56] Similarly, slower heating gives more time for intermediates to form and change the product distribution compared to faster heating or higher temperatures.

While the catalytic channel replicates very high temperature conditions for a short residence time, the heat applied to the sample during desorption can promote alternate decomposition. For example, TNT thermally dissociates below 573 K with isolatable quantities of 1,3,5-trinitrobenzene (TNB), 2,4-dinitroanisole, 2,4,6-trinitrobenzyl alcohol, 2,4,6-trinitrobenzoic acid and NO_2.[80] At 473 K, TNB was not formed and instead 2,4,6-trinitrobenzaldehyde and a variety of azo dimers were observed.[81] Although all of these products would be expected to dissociate themselves in our converter they could potentially do so without producing NO_2 (e.g. proceed to produce N_2O as has been observed for PETN).[82] Such behaviour during desorption (or in the cTD-CRDS converter) could be contributing to the low concentrations recovered. Additionally,

this mechanistic variation could help explain the varying levels of success preconcentrating explosives with Tenax.[78, 83]

3.4.2.2 Background signal in reference channel

The reference channel responded to desorption of TNT from the pre-concentration trap. The source of this response is uncertain but is perhaps a by-product of Tenax decomposition. Tenax has been demonstrated to produce degradation products under oxidizing conditions and heat.[76] Heating the Tenax trap when sampling zero air alone gave no observable signal in either of the cTD-CRDS channels indicating that the presence of trapped TNT contributed to the signal observed in the reference channel. If TNT trapped on the Tenax began to fragment, due to a heterogenous decomposition process, decomposition fragments could be responsible for inducing Tenax deterioration at the low temperatures employed for desorption. This is consistent with the proposed decomposition of TNT during the heating phase proposed in section 3.4.2.1.

3.4.3 Pre-concentration of PETN, Tetryl and RDX

Although pre-concentration results appear at first glance promising, with PETN, Tetryl and RDX all giving signals upon pre-concentration, a more detailed examination is troubling. Firstly, the trend in the size of the desorption peaks (PETN>RDX> Tetryl) did not track with the trend in saturation vapour pressures (PETN>Tetryl>RDX). However, even upon assuming saturation vapour pressure was achieved in the sample glass traps the expected upper limit preconcentrated was smaller than the areas observed during desorption from the trap. As it is unlikely that all three molecules have such large errors in their literature reported saturation vapor pressures it is likely that the cTD-CRDS is responding to one or more interferences.

As care was taken to ensure that species were dried and free of acetonitrile it is possible that the drying process allowed some explosive degradation/decomposition to occur. As no measurable signal was observed prior to desorption the measured species appears to be formed during desorption from the Tenax trap or because of the interaction of the explosive vapors or their degradation products with the Tenax material. The absence of a response also suggests there was no cross-contamination or memory effects in connecting tubing. Further testing would be required to gain more insight into the nature of these interfering species. Until such time as this interference is understood, the cTD-CRDS is not suitable for the measurement of PETN, Tetryl, or RDX.

3.4.4 A note regarding the Tenax trap and its durability

The current setup uses an Omega CSi32 bench top controller that was used to ramp heat as fast as possible to reach a set point. The ramp rate varied by up to 5 K/s for different trials and often overshot the setpoint. The final desorption temperature also varied by ±5 K. As temperature may be critical to the products distribution and the mechanism of decomposition, a fast and consistent ramp rate is ideal. The cTD-CRDS setup would as such benefit from a more precise heating system.

The repeated heating of Tenax at high temperatures leads to irreversible background noise by thermal and oxidative degradation.[76] The increasing background noise during recovery was noticed slightly during TNT sampling towards the end of the sampling period. The background signal was noticeable with the trap after approximately 80 desorption cycles. The lifetime of the Tenax pre-concentration unit should be investigated further under the experimental conditions to evaluate the long-term durability of the trap.

Oxidative degradation of Tenax polymer forms many artifacts that have not fully been characterized.[76] The effect of strong oxidizing agents on Tenax is discussed throughout literature

and O_3 and NO_2 are among the most common oxidizing agents that reduce the longevity of the Tenax sorbent.[76, 84] All three of these gasses may potentially form in the Tenax trap during desorption if decomposition of the explosive is initiated. Furthermore, these gases are produced in the cTD-CRDS converter. When not in operation or during the shut down procedure, the mirror purge flows create a very small flow of zero air in the reverse direction through the instrument. Residual amounts of O_3, NO_2, and NO may be directed towards the Tenax pre-concentration unit and cause it to degrade. Such degradation pathways must be reduced (e.g. by capping the trap when not in use) and an alternative sorbent material utilized if possible (e.g. a nitroaromatic selective cavitand sorbent material[85]).

3.5 CONCLUSIONS

Trace detection of TNT vapors by cTD-CRDS with automated pre-concentration has been described and demonstrated. Preconcentration did not provide the anticipated signal to noise whilst reducing the time resolution of the instrument making it ineffectual. Furthermore, Tenax was found to degrade upon use with TNT and a more robust sorbent material is needed. Finally, trapping PETN, Tetryl, and RDX on Tenax gave rise to an unexplained interference. Understanding the nature of the interference and its formation chemistry is required prior to pursuing further trapping studies with Tenax.

Chapter Four: Peroxy Radical Chemical Amplification for the Detection of TATP

In this chapter the feasibility of utilizing peroxide radical chemical amplification (PERCA) for the detection of TATP is explored. A modelling study on PERCA chain carriers demonstrating the utility of ethane as a chain carrier was examined. The effect of elevated temperature on PERCA chemistry was also investigated.

4.1 TATP and other organic peroxide explosives

Organic peroxide explosives are increasingly common in terrorist attacks.[15] Some examples are shown in Figure 4.1. Their usage by the military and industry has been limited due to the relative ease with which peroxide explosives detonate.[2, 12] This hazardous property of peroxide explosives makes them an ideal candidate for illegal use by those who are capable of safely formulating them or accept such risks.[2] The most notorious peroxide explosive is TATP (also referred to as the "mother of Satan"); it's detection will be the focus of this chapter.

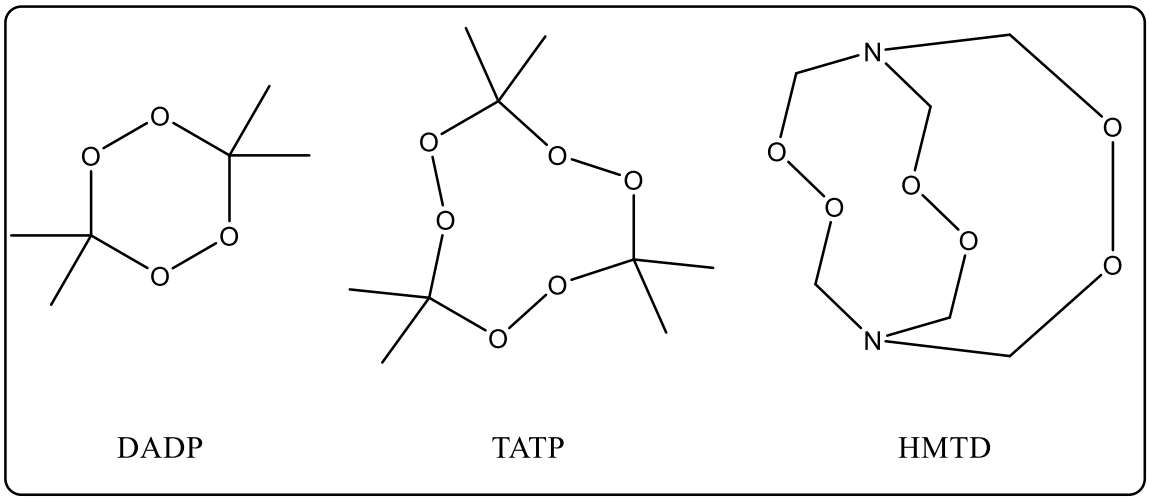

Figure 4.1 Organic peroxide explosives 3,3,6,6-tetramethyl-1,2,4,5-tetraoxane (DADP), 3,3,6,6,9,9-hexamethyl-1,2,4,5,7,8-hexaoxonane (TATP), and 3,4,8,9,12,13-hexaoxa-1,6-diazabicyclo[4.4.4]tetradecane (HMTD).

In spite of TATP's relatively high room-temperature vapor pressure of ~50 mTorr,[28, 86-87] its detection at security check points remains a challenge because it does not contain distinguishing features such as a nitro group, metallic elements, or characteristic UV-Vis or fluorescence spectra which are utilized to detect other classes of explosives.[88-92] Because of this need, a variety of instrumental techniques for detection of TATP vapors have been developed. These include ion mobility spectrometry (IMS),[30, 39] atmospheric pressure chemical ionization mass spectrometry (APCI-MS),[39] cold electron impact ionization mass spectrometry coupled to fast gas chromatography,[93] photoacoustic spectroscopy,[89] stand-off detection in the mid-infrared,[94] hydrogen peroxide indicators,[95] chemiluminescence following digestion with horseradish peroxidase,[96] high performance liquid chromatography,[97] and electrochemical,[98] colorimetric,[99] biochemical,[100] and semiconductor[101] sensors. However, none of these methods has found widespread use with security agencies to date due to either high acquisition costs, requirement for a skilled operator, and/or lack of robustness in the field. Additionally, many of these techniques

require swabbing an individual or their luggage and are as such inefficient. Hence, the development of new and improved methods for real-time detection of TATP vapor continues to be of interest.

4.1.1 Triacetone Triperoxide (TATP) undergoes an entropic explosion

Our fundamental understanding of peroxide explosives is not as complete as our understanding of other classes of explosives.[1-2] Although the O-O bond is a source of oxygen, the stoichiometry is insufficient to oxidize the majority of the carbon and hydrogen atoms in the molecule. Organic peroxides such as DADP, HMTD, and TATP contain several peroxide linkages and are as such more explosive. This was initially thought to be a result of more appropriate stoichiometry allowing for a greater extent of oxidation. However, a recent study discovered large proportions of acetone in the post-blast residues of DADP and TATP.[12, 14, 90] A theoretical study that followed proposed that the explosion of peroxide explosives is not a rapid oxidation but an extremely efficient multistep entropic explosion.[12] TATP was studied as the model organic peroxide explosive and was found to thermally dissociate via several acetone losses. The dissociation scheme presented (Figure 4.2) included peroxy radical intermediates. Their detection will be attempted in the following chapters.

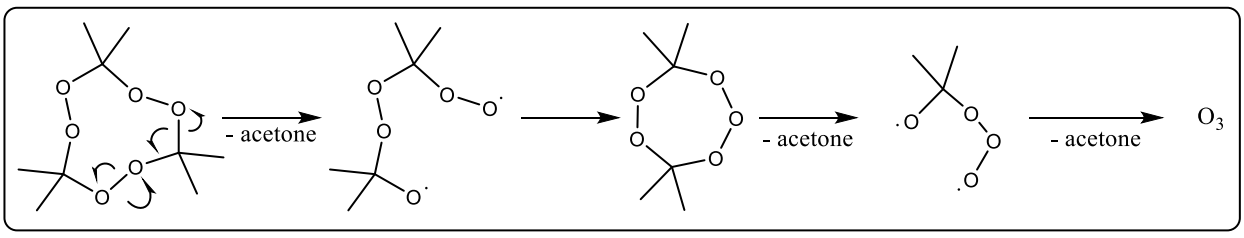

Figure 4.2 TATP thermal decomposition scheme as proposed by Dubnikova et al.[12]

4.1.2 Peroxy radical chemical amplification (PERCA) of atmospheric peroxy radicals

Peroxy radicals such as the hydro and methyl peroxyl radicals (HO_2 and CH_3O_2) are important trace constituents of the atmosphere.[102-103] Derived mainly from reaction of the atmosphere's chief oxidant, the hydroxyl radical (HO), with either carbon monoxide (CO) or hydrocarbons (RH), they are involved in the photochemical production of ozone (O_3) in the troposphere,[104-105] the catalytic destruction of O_3 in the stratosphere,[106-107] and the chemistry of organic aerosol formation.[108-110] In spite of their central role in atmospheric chemistry, concentrations of HO and HO_2 are small and peak from ~10^6 to ~10^7 molecules cm^{-3} and from ~10^8 to ~10^9 molecules cm^{-3}, respectively,[111] such that highly sensitive and specialized methods are required for their quantification. One such method is PERCA.[112]

In PERCA, concentrations of atmospheric RO_x (= HO + HO_2 + ΣRO_2) radicals are amplified by factors of between ~20 to ~190 through a series of catalytic reaction steps, usually involving parts-per-million by volume (ppmv) concentrations of nitric oxide (NO) and percent levels of either carbon monoxide (CO)[112-130] or more recently a short chain hydrocarbon such as ethane (C_2H_6)[118, 131] (Figure 4.3). Under these conditions, the peroxy radicals catalytically convert NO to NO_2, and the amount of NO_2 produced over a constant reaction period is proportional to the number of radicals that were present originally.

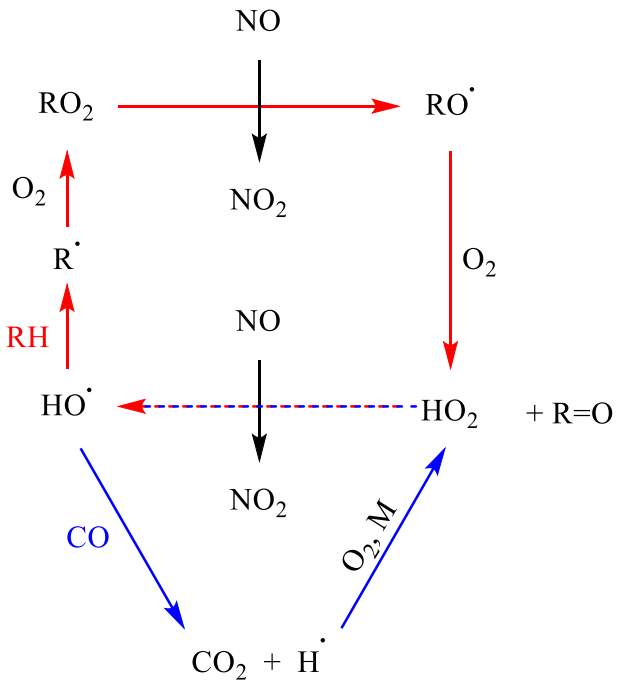

Figure 4.3. Peroxy radical chemical amplification cycle with a hydrocarbon (shown in red) or carbon monoxide (shown in blue). Radical sinks are not shown.

A key operational parameter of any PERCA instrument is the radical chain length or amplification factor ($CL = \frac{NO_2\ produced\ by\ PERCA}{RO_2 + HO_2\ input}$) which must be carefully calibrated. This chain length is suppressed by water vapor, whose presence increases the rates of radical loss on the inner walls of the PERCA chamber and the rates of certain gas-phase reactions, e.g., the reaction between the hydroperoxyl radical - water dimer ($HO_2 \cdot H_2O$) with NO to form peroxynitrous acid (HOONO) which can isomerize to nitric acid ($HONO_2$).[118, 132, 133]

The most obvious way to minimize wall reactions is to apply heat. However, this is usually avoided as heating the inlet dissociates thermolabile radical reservoir species, i.e., peroxy nitrates (PN, RO_2NO_2) which include peroxynitric acid (HO_2NO_2, PNA), methyl peroxynitrate ($CH_3O_2NO_2$, MPN), and the peroxycarboxylic nitric anhydrides ($RC(O)O_2NO_2$, PANs). These

molecules are generated in the atmosphere from reactions between RO_2 radicals with NO_2, which, amongst other things, moderates the rate of photochemical O_3 production by (at least temporarily) removing the active species (i.e., HO_2, RO_2, and NO_2) involved. The PN and PANs are generally more abundant than their free radical precursors in the troposphere: daytime mixing ratios peak in the range from 10s to a few 100s of parts-per-trillion by volume (pptv, 10^{-12}) for HO_2NO_2 to several parts-per-billion by volume (ppbv, 10^{-9}) in the case of peroxyacetic nitric anhydride (PAN). Thus, these molecules have considerable interference potential even if only a small fraction dissociates in a heated PERCA inlet.

4.1.2.1 Considerations for TATP detection using PERCA

Coupling a thermal dissociation inlet to a PERCA instrument potentially provides a novel means of TATP detection. TATP's thermal dissociation has been previously characterized and TATP has an activation energy (Ea) of 151 kJ mol^{-1} and a pre-exponential factor of 3.75×10^{13} s^{-1}.[14] This is similar to the thermal dissociation of alkyl nitrates (Ea of 150-180 kJ mol^{-1}, A of ~10^{14} s^{-1})[57-58, 134-135] which are commonly measured using thermal dissociation inlets.

The nature of the PERCA method, particularly when coupled to a fast NO_2 measurement such as CRDS, should allow for continuous and rapid measurement of TATP. Employing a TD inlet should help reduce wall losses and improve radical chain lengths. However, these improved radical chain lengths will be at the expense of increased interferences from PNA and PAN in ambient air. Nonetheless, PNA and PAN are not expected to vary drastically on the time scales needed for rapid screening of explosives at a transportation hub or checkpoint.

As TATP is relatively volatile (~70 ppm at room temperature),[86-87, 136] conversion of a small fraction of the peroxide radicals, produced during decomposition, to NO_2 via reaction with NO

should allow for indirect detection of TATP as NO_2 instrumentation is capable of sub-ppbv measurements. However, deliberate concealment of explosives can reduce their observed mixing ratios by an estimated factor of ~1000,[17] increasing the need for highly sensitive instrumentation. Amplification of the signal generated by TATP radicals with PERCA should provide adequate sensitivity for detection of TATP even after deliberate concealment.

4.1.2.2 Alternative chain carriers

Perhaps one of the most important considerations for a TATP measurement using TD-PERCA is the choice of chain carrier. The chain carrier needs to be highly reactive towards HO (by having both high mixing ratios and rate coefficients with respect to reaction with HO) to compete with chain terminating HO reactions such as wall losses. An appropriate chain carrier needs to be safely deployed alongside the instrument at an airport or security checkpoint. As such, CO, although a commonly employed chain carrier is not an attractive choice because of its high toxicity. A modelling study by Anastasi, Gladstone and Sanderson[137] examined ethene, propene, ethanol, and dimethyl ether as alternative chain carriers. The Anastasi study found all alternative chain carriers were predicted to have higher chain lengths than CO. Alkenes, however, are not feasible as PERCA chain carriers as they can react with O_3 in ambient air and generate Criegee biradicals. Ethanol, was deemed too non-volatile and the authors speculated that introducing elevated mixing ratios into the PERCA reactor would be an issue. Dimethyl ether was suggested as an appropriate alternative although no papers since appear to have attempted PERCA with dimethyl ether. A modelling study focusing on alternative chain carriers, mainly alkanes, was conducted and is detailed below. Recently, Wood et al.[131] published their work successfully utilizing ethane as a

PERCA radical chain carrier. This led to a focus on ethane as a radical chain carrier in the remaining modelling work.

4.1.2.3 Effect of increased temperature on PERCA

Besides the choice of chain carrier, the other key factor contributing to radical chain lengths and amplification is temperature. By its nature TD-PERCA will require heating to induce thermal dissociation. As this is novel, the effect of these elevated temperatures on radical chemistry in the PERCA reactor will be explored through modelling (this chapter) and experiment (chapter 5). As ethane was ultimately used as a chain carrier in experimental work, it was the focus of the elevated temperature modelling study (sections 4.2.2 and 4.3.2).

The chemistry in an ethane PERCA reactor is outlined in Table 4.1 below. The main radical chain carrying reaction between HO and C_2H_6 (R4.4) has a positive activation energy and is expected to proceed more rapidly upon addition of heat to the PERCA reactor. However, all NO radical reactions, those that produce NO_2 (R4.1, R4.3, R4.5), including the reaction between HO_2 and NO the ultimately produced HO, have negative activation energies and are expected to slow down upon the addition of heat. In addition, one major limitation is that kinetic data for many reactions are based on measurements at room temperature or colder and, therefore, rate constants are only extrapolated to the high temperatures explored here.

4.1.2.4 General PERCA modelling considerations

Models simulating PERCA reaction chambers need to make assumptions about the magnitudes and temperature dependencies of wall loss rates and rate coefficients for chain-terminating reactions such as RONO formation[131] to reproduce experimental data. Thus, simulations are poor

a priori predictors of experimental chain lengths and should not be viewed as such. Nonetheless, the modelling results here were used to shed some light onto experimental results and trends. The experimental work is discussed in detail in Chapter 5.

Table 4.1 List of chemical reactions*

Number	Reaction	k (cm^3 $molecule^{-1}$ s^{-1})	k_{298K} (cm^3 $molecule^{-1}$ s^{-1})
R4.1	$CH_3O_2 + NO \rightarrow CH_3O + NO_2$	$2.3\times10^{-12} \times e^{(360/T)}$	7.7×10^{-12}
R4.2	$CH_3O + O_2 \rightarrow HCHO + HO_2$	$7.2\times10^{-14} \times e^{(-1080/T)}$	1.9×10^{-15}
R4.3	$HO_2 + NO \rightarrow HO + NO_2$	$3.5\times10^{-12} \times e^{(270/T)}$	8.5×10^{-12}
R4.4	$C_2H_6 + HO + O_2 \rightarrow H_2O + C_2H_5O_2$	$6.9\times10^{-12} \times e^{(-1000/T)}$	2.4×10^{-13}
R4.5	$C_2H_5O_2 + NO \rightarrow C_2H_5O + NO_2$	$2.55\times10^{-12} \times e^{(380/T)} \times 0.99$***	9.1×10^{-12}
R4.6	$C_2H_5O + O_2 \rightarrow CH_3CHO + HO_2$	$2.4\times10^{-14} \times e^{(-325/T)}$	8.1×10^{-15}
R4.7	$HO + NO + M \rightarrow HONO + M$	$7.4\times10^{-31} \times (T/300)^{-2.4} \times [M]$	9.7×10^{-12} **
R4.8	$HO_2 + NO_2 + M \rightarrow HO_2NO_2 + M$	(termolecular)	(termolecular)
R4.9	$HO_2 + HO_2 + M \rightarrow H_2O_2 + M$	(termolecular)	(termolecular)
R4.10	$CH_3O_2 \rightarrow 0.330\ CH_3O + 0.335\ HCHO + 0.335\ CH_3OH$	$1.8\times10^{-13} \times e^{(416/T)} \times \Sigma RO_2$	$7.4\times10^{-13} \times \Sigma RO_2$
R4.11	$C_2H_5O_2 \rightarrow 0.6\ C_2H_5O + 0.2\ CH_3CHO + 0.2\ C_2H_5OH$	$3.1\times10^{-13} \times \Sigma RO_2$	$3.1\times10^{-13} \times \Sigma RO_2$

* Rate constant expressions are from the Master Chemical Mechanism (MCM),[138-139] version 3.3.1, except R7 and R9, which are from Kabir et al. [140]

** calculated using $[O_2] = 4.2\times10^{18}$ molecules cm^{-3}

4.2 Model Description

4.2.1 Role of chain carriers on amplification

To assess the efficacy of different molecules as PERCA chain carriers box model simulations were carried out using a subset of reactions in the "Master Chemical Mechanism" (MCM) V3.3.1 obtained from http://mcm.leeds.ac.uk/MCM and simulated using AtChem online (V1.5).[138-139, 141] The chain carriers examined were: CO, methane (CH_4), ethane (C_2H_6), propane (C_3H_8), butane (C_4H_{10}), pentane (C_5H_{10}), hexane (C_6H_{14}), ethene (C_2H_4), ethyne (C_2H_2), propene (C_3H_6), ethanol (C_2H_5OH), and dimethyl ether (CH_3OCH_3). The MCM subset was obtained by "marking" the chain carriers that were examined and extracting the mechanism from the MCM. This resulted in a subset of the MCM with 531 species and 1648 reactions.

As per Wood and Charest,[125] model simulations were initiated with 8.7 % of the chain carrier and 3.3 ppmv of NO. In a similar fashion to the simulations carried out by Anastasi et al.[137] and others, plug flow modelling was used. The model simulations were initiated with an input of 15 pptv CH_3O_2 and allowed to proceed for 30 seconds. The model assumes a static reaction vessel without non-chemical addition or removal of species (i.e. no transport or wall exchange reactions).

As mentioned above, models are poor a priori predictors of experimental chain lengths particularly when they do not account for radical losses. However, incorporating radical losses requires assumption about the magnitudes and temperature dependencies of wall loss rates. Nonetheless, models greatly overestimate chain lengths when wall losses are not incorporated into the model. To get some sense of the effect of wall losses on the various PERCA chain carriers examined, wall losses were added to the model with a wall loss rate of 2.5 s^{-1} (as per Hastie et al. [114]) for all radical species.

Table 4.2 Model inputs for simulations run with the different chain carriers at 25 °C

	Mixing Ratio	Number density (molecules cm^{-3})
M	-	2.14×10^{19}
NO	3.3 ppmv	7.06×10^{13}
chain carrier	8.7%	1.86×10^{18}

4.2.2 Effect of heat on ethane radical chemistry and amplification

4.2.2.1 MCM only simulations

Box model simulations were carried out using a subset of the MCM V3.3.1 and the Kinetic Preprocessor (KPP).[142] KPP was used instead of AtChem online for the remaining simulations as it allowed more control over the model (e.g. time steps less than 1s, extra model subroutines that run alongside the chemistry, etc.). The chemistry taking place in the PERCA reactor was modelled at temperatures of 25 °C or 250 °C. The ethane subset was selected from the MCM by adding ethane to the marked list and extracting the subset in KPP format along with inorganic reactions and generic rate coefficients. The resultant subset of the MCM contained 58 species and 163 reactions. Once again, a plug flow modelling approach was used where initial conditions and mixing ratios were set and the model allowed to proceed without any additional inputs or outputs.

Simulations were performed using the optimized PERCA reagent gas concentrations (i.e., 650 ppbv NO; 1.65 % ethane (see chapter 5 section 5.3.3)) at either 25 °C or 250 °C. Table 4.3 provides an overview of the model inputs. The model runs were also initialized with an initial input of 15, 100, 300, 600, 900, or 1200 pptv of either HO_2 or CH_3O_2.

Table 4.3 Model inputs for simulations run at 25 °C and 250 °C

	Mixing Ratio	Number density at 25 °C (molecules cm^{-3})	Number density at 250 °C (molecules cm^{-3})
M	-	2.14×10^{19}	1.22×10^{19}
NO	650 ppbv	1.39×10^{13}	7.92×10^{12}
C_2H_6	1.65%	3.53×10^{17}	2.01×10^{17}
O_2	20.1%	4.29×10^{18}	2.45×10^{18}
N_2	77.6%	1.66×10^{19}	9.46×10^{18}

4.2.2.2 Inclusion of $HO_2 \cdot H_2O$ cluster formation in the mechanism

Mihele and Hastie [132] identified the HNO_3 forming reaction between $HO_2 \cdot H_2O$ and NO as an important relative humidity dependent radical sink reaction. Formation of $HO_2 \cdot H_2O$ is not part of the MCM. To estimate the temperature dependent formation of $HO_2 \cdot H_2O$ cluster, it was assumed that equilibrium between the cluster and HO_2 and H_2O was established at every model time step (0.1 s). The equilibrium rate constant reported by Kanno et al. [143]: $6.6 \times 10^{-17} \times T \times e^{(3700/T)}$ was used. Two reactions of $HO_2 \cdot H_2O$ were added: reaction with HO_2 leading to loss of radicals ($k = 6.0 \times 10^{-13}$ cm^3 $molecule^{-1}$ s^{-1}) [143] and reaction with NO leading to HNO_3 formation ($k = 5.4 \times 10^{-11} e^{(-410/T)}$ cm^3 molecule-1 s^{-1}).[144-145]

4.2.2.3 Inclusion of wall losses in the mechanism

In a separate simulation radical wall losses were added to the KPP model with the rate constants reported by Mihele et al. [133] of 2.8 s^{-1} and 0.8 s^{-1} for HO_2 and RO_2, respectively.

4.2.2.4 Inclusion of ethyl nitrite and ethyl peroxy nitrate formation in the mechanism

A potentially important radical chain termination reaction not included in the MCM is that between C_2H_5O and NO:[118, 131]

$$C_2H_5O + NO \rightarrow C_2H_5ONO \qquad \text{R4.12}$$

The rate of this reaction decreases slightly with temperature: At a pressure of 660 Torr and using kinetic parameters from NASA's Jet Propulsion Laboratory's Chemical Kinetics and Photochemical Data evaluation #18 (Burkholder, et al. [146]), the rate coefficient decreases from 4.8×10^{-11} to 3.9×10^{-11} cm^3 $molecule^{-1}$ s^{-1} between 25 °C and 250 °C. Ethyl nitrite thermally decomposes:

$$C_2H_5ONO \underset{\Delta}{\rightarrow} C_2H_5O + NO \qquad \text{R4.13}$$

The activation barrier for TD is ~157 kJ mol^{-1} (Steacie and Shaw [147]) and has a lifetime with respect to thermal decomposition of ~40 s at 250 °C; this implies that for temperatures between 25 °C and 250 °C, ethyl nitrite will not significantly decompose and constitutes a radical sink.

Another potentially important radical chain termination reaction not included in the MCM is that between $C_2H_5O_2$ and NO_2:[131]

$$C_2H_5O_2 + NO_2 \rightarrow C_2H_5O_2NO_2 \qquad \text{R4.14}$$

The rate of this reaction also decreases slightly with temperature: at a pressure of 660 Torr and using the kinetic parameters from Burkholder, et al. [146], the rate coefficient decreases from 8.8×10^{-12} to 8.5×10^{-12} cm^3 $molecule^{-1}$ s^{-1} between 25 °C and 250 °C. Ethyl peroxy nitrate thermally decomposes:

$$C_2H_5O_2NO_2 \underset{\Delta}{\rightarrow} C_2H_5O_2 + NO_2 \qquad \text{R4.15}$$

The activation barrier for TD is ~86.8 kJ mol^{-1}. This corresponds to lifetimes with respect to thermal decomposition of ~0.2 s and ~5×10^{-8} s at 25 °C and 250 °C, respectively. Formation of this molecule is hence expected to be a radical sink at 25 °C but not at 250 °C.

4.3 Results

4.3.1 Amplification as a function of chain carrier selection

Figures 4.4 and Table 4.4 show the radical chain lengths obtained after 1s of simulation when the model was initiated with 15 pptv of CH_3O_2 for different radical chain carriers at 25 °C. A time of 1s was chosen as this corresponds to the residence time in most PERCA reactors in literature. The highest chain lengths, prior to inclusion of wall losses, were observed for ethanol (CL = 537), ethyne (CL = 419), CO (CL = 387), and ethene (CL = 314). The trend observed for CO, ethanol, ethene and dimethyl ether agrees qualitatively with the simulation results published by Anastasi et al.[137] Sensitivity to wall losses increases with CL before the inclusion of wall losses. For the n-alkanes, apart from ethane, the CL decreases with increasing size of the molecule. Of the alkanes, ethane has the highest CL and was therefore chosen as chain carrier for experimental and modelling work.

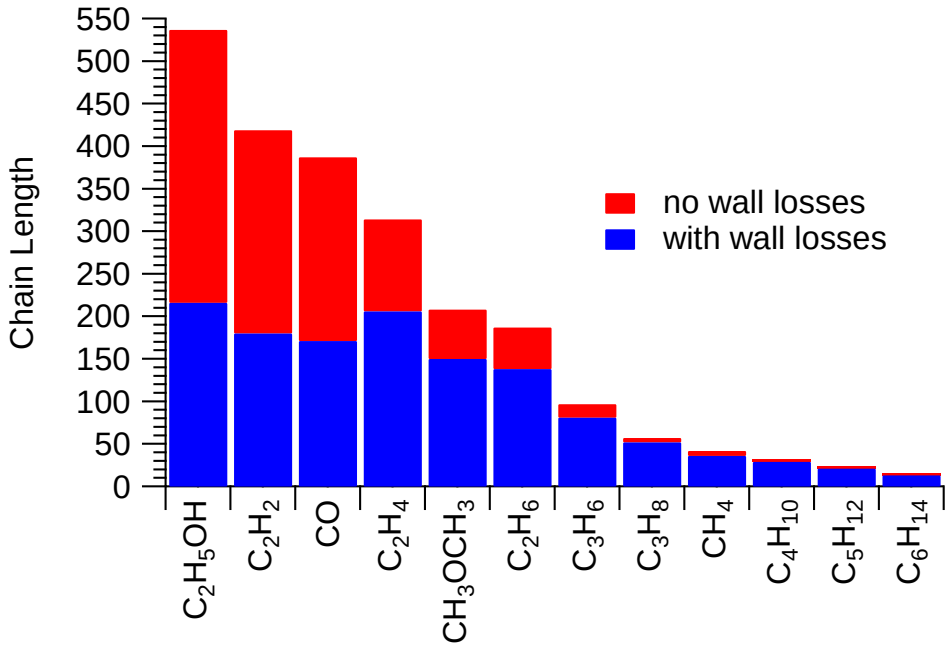

Figure 4.4. Bar graph with chain lengths obtained after 1s of amplification for simulation initiated with 15 pptv of CH_3O_2 and 8.7 % chain carrier at 25 °C.

Table 4.4 Chain lengths obtained after 1s of amplification for simulations initiated with 15 pptv CH_3O_2 at 25 °C

Chain Carrier	Chain Length (no wall losses)	Chain Length (wall losses)
C_2H_5OH	537	216
C_2H_2	419	180
CO	387	171
C_2H_4	314	206
CH_3OCH_3	208	150
C_2H_6	187	138
C_3H_6	97	81
C_3H_8	57	52
CH_4	42	36
C_4H_{10}	30	29
C_5H_{12}	22	21
C_6H_{14}	13	13

4.3.2 Effect of temperature on PERCA radical chemistry

4.3.2.1 MCM gas phase chemistry model runs

Figures 4.5 and 4.6 show time series of peroxy and hydroxyl radical concentrations during simulations initiated with 15 pptv of HO_2 at 25 °C and 250 °C, respectively. Due to the lower gas density at higher temperatures, lower concentrations of RO_2 radicals are present initially (even though the initial mixing ratios are the same in both cases). Reactions of HO_2 and RO_2 with NO have negative activation energies and are hence slower at higher temperatures, leading to a lower rate of HO radical production and, since HO loss rates are similar, to lower HO concentrations (maximum of ~1.9×10^4 molecules cm^{-3} at 250 °C vs. 2.2×10^5 molecules cm^{-3} at 25 °C) and lower turnover numbers at higher temperatures. Simulations initiated with HO_2 radicals gave identical results to simulations initiated with CH_3O_2 radicals.

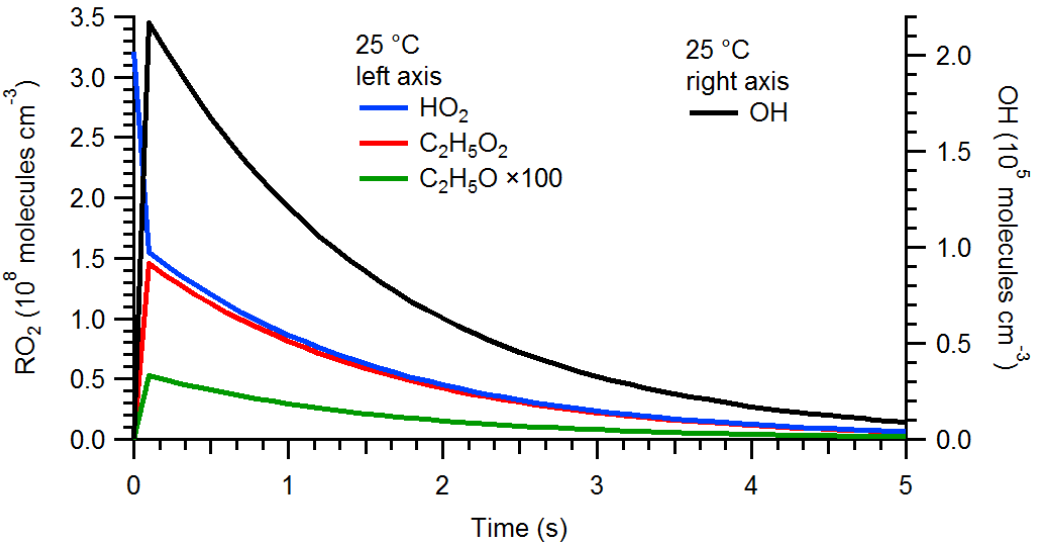

Figure 4.5 Time series of peroxy radicals (left-hand axis) and hydroxyl radicals for a simulation initiated with 15 pptv of HO_2 at 25 °C.

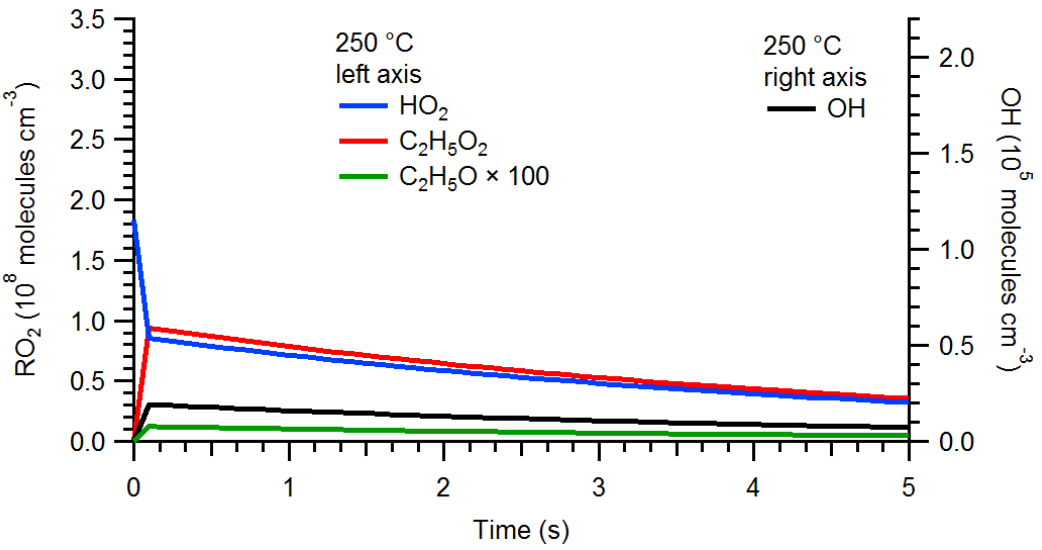

Figure 4.6 Time series of peroxy radicals (left-hand axis) and hydroxyl radicals for a simulation initiated with 15 pptv of HO_2 at 250 °C.

Figure 4.7 shows the CL (number of NO_2 molecules produced divided by molecules of RO_2 present originally) as a function of temperature and mixing ratio of radicals added initially. For simulations conducted at 25 °C the chain length appears to be highly concentration dependent. For simulations conducted at 250 °C the chain length appears to still be concentration dependent albeit to a much lesser extent. Upon consideration of radical losses due to wall reactions, chemistry is expected to conclude before these significant differences in chain length are observed experimentally. However, the CL in the initial ~1 s of reaction time was generally well below the CL obtained at the lower temperature.

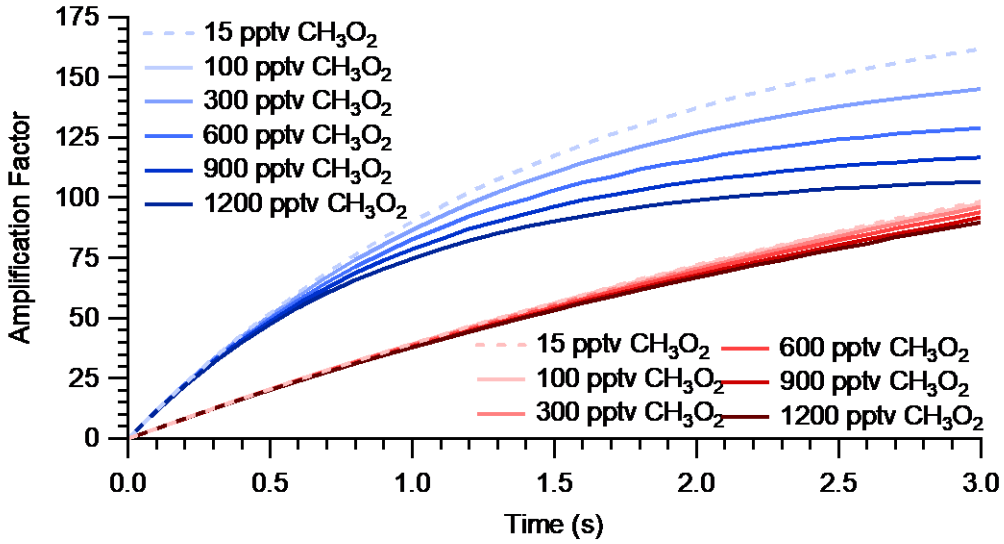

Figure 4.7 Time series of CL for simulations initiated with 100, 300, 600, 900, and 1200 pptv of CH_3O_2 at 25 °C (blue colors) and 250 °C (red colors).

4.3.2.2 Effect of $HO_2 \cdot H_2O$ cluster

Figure 4.8 shows the CL obtained after the inclusion of $HO_2 \cdot H_2O$ cluster as a function of relative humidity (RH) at 25 and 250 °C with model runs initiated with 15 pptv CH_3O_2. The model simulations displayed in Figure 4.8 clearly demonstrate the higher sensitivity of the CL at 25 °C to changes in RH.

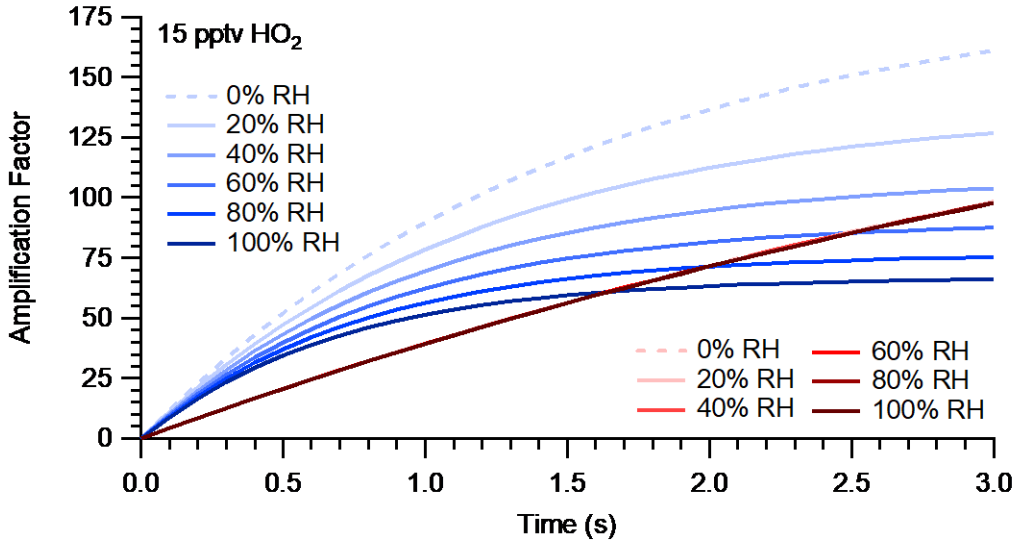

Figure 4.8 Time series of CL for simulations at different RH and initiated with 15 pptv of HO_2 at 25 °C (blue colors) and 250 °C (red colors).

Figure 4.9 shows the concentration dependence at a RH of 20% after inclusion of water clusters in the model simulations. Ultimately, lower CL are observed in the 25 °C system while the 250 °C system chemistry, and associated CL, are relatively unchanged. Furthermore, CLs at 250 °C and in the initial ~1 s of reaction time were generally well below CLs obtained at the lower temperature.

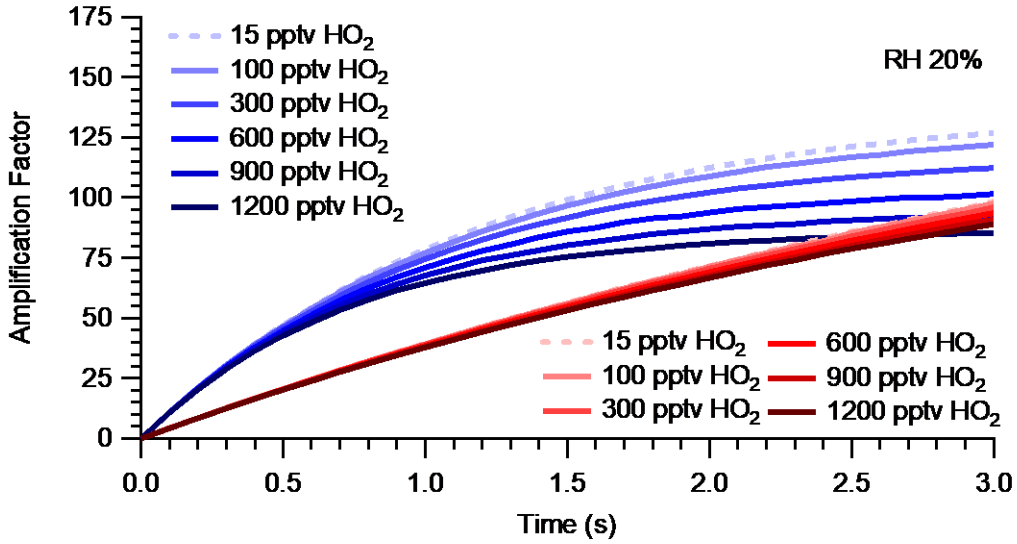

Figure 4.9 Time series of CL for simulations at 20% RH initiated with different HO_2 mixing ratios at 25 °C (blue colors) and 250 °C (red colors).

4.3.2.3 Effect of wall losses

Figure 4.10 shows a time series of the CL for simulations conducted at 20% RH after inclusion of wall losses in the model. Due to increased radical losses, radical chemistry ceases after ~ 1s. Furthermore, the CL dependence on radical concentration is reduced.

Inconsistent with experiment (Chapter 5), the CL is still predicted to be larger at 25 °C than at 250 °C. This may be a result of the use of temperature-independent wall loss rates that should be reduced at elevated temperatures. Assuming, as a lower limit, no wall losses at 250 °C, and factoring in the 2.3 second residence time of our PERCA chamber, the simulations predict larger CL at elevated temperatures (a CL of 80 at 250 °C and a CL of 44 at 25 °C – shown as a green trace in Figure 4.10).

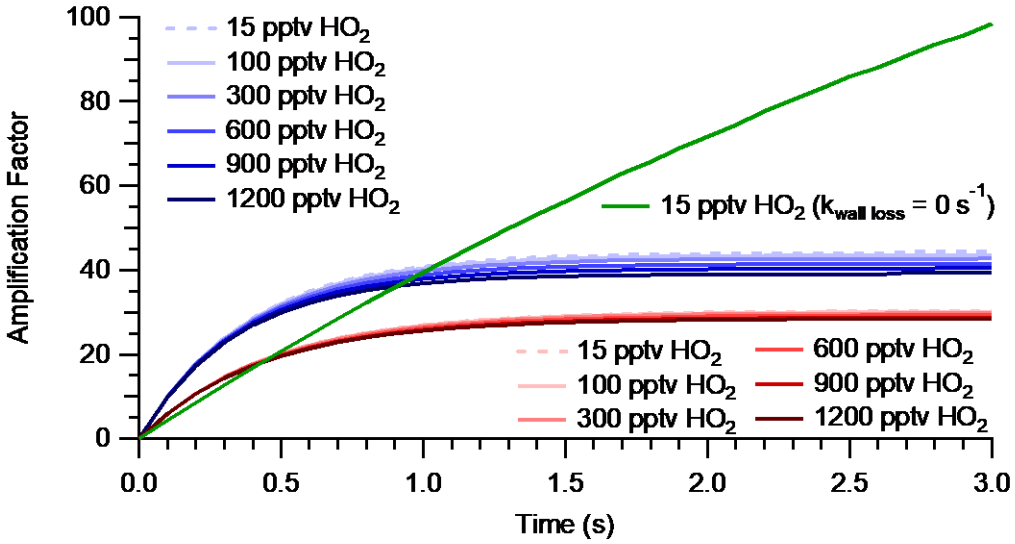

Figure 4.10 Time series of CL for simulations at 20% RH initiated as a function of HO_2 mixing ratios at 25 °C (blue colors) and 250 °C (red colors) with $k_{wall}(HO_2)$ and $k_{wall}(RO_2)$ of 2.8 s^{-1} and 0.8 s^{-1}, respectively.

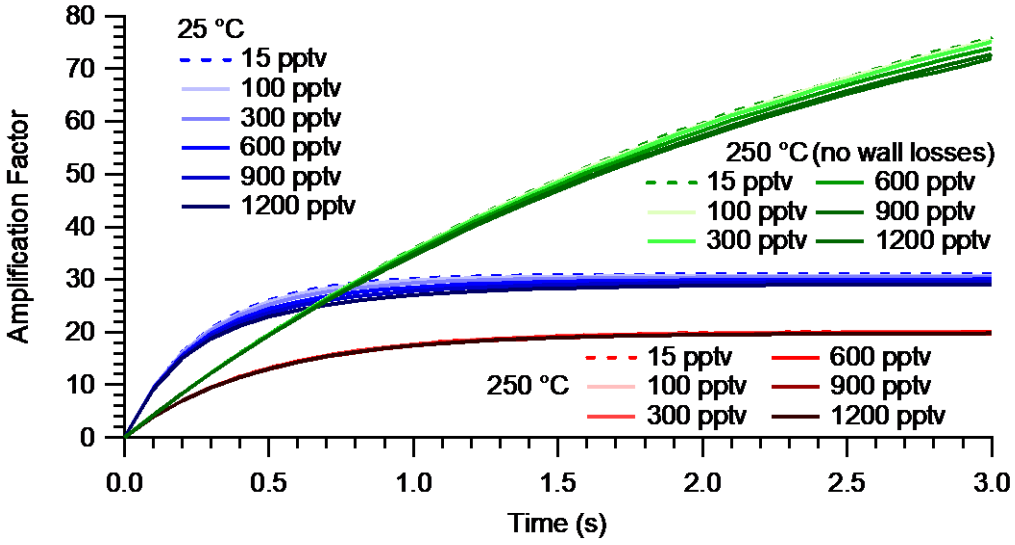

Figure 4.11 Same as Figure 4.10 but with C_2H_5ONO and $C_2H_5O_2NO_2$ formation and thermal decomposition included in the mechanism.

4.3.2.4 Effect of the inclusion of ethyl nitrite and ethyl peroxy nitrate formation and decomposition

Shown in Figure 4.11 are the simulations of Figure 4.10 with C_2H_5ONO and $C_2H_5O_2NO_2$ formation and thermal decomposition added to the mechanism. For both simulations at 25 °C and 250 °C, the CLs were reduced. This reduction in CL is due to the loss of radicals to ethyl nitrite formation which is expected to occur irreversibly, in the 2.3 s residence time, in both the 25 °C and the 250 °C simulations.

Assuming, as a lower limit, no wall losses at 250 °C, and factoring in the 2.3 s residence time of our PERCA chamber, the simulations predict larger CL at elevated temperatures (a CL of 65 at 250 °C and a CL of 30 at 25 °C – shown as a green trace in Fig. 4.11).

4.4 Discussion

The first goal of the modelling study was to examine the efficacy of different molecular species as radical chain carriers. Large CLs were observed for CO as well as ethene, ethyne, dimethyl ether and ethanol. This is consistent with the results of Anastasi et al.[137] although their less explicit reaction schemes appear to underestimate radical losses since these CLs are generally lower. Nonetheless, many of these species are unsuitable as radical chain carrier alternatives to CO. Unsaturated hydrocarbons are prone to reaction with O_3, which is present in ambient air at variable quantities.[148] This would translate into the PERCA reactor generating its own radicals. Ethanol is not sufficiently volatile (7.8 % at 298K)[149] to achieve high enough gas phase mixing ratios in the PERCA reactor[137] upon dilution with instrument flows. Dimethyl ether (and perhaps other ethers) appears to provide a CL similar to that of CO without the toxicity and potential for interference from O_3 reactivity.

As for the alkane series, ethane provides for the highest CL. This is partially the result of the slower reactivity of the more stable larger radical chain carriers. Additionally, upon reaction with NO, peroxy radicals with longer alkyl chains are more likely to form alkyl nitrates (as opposed to NO_2 and an alkoxy radical).[150] Furthermore, the larger alkanes would not be volatile enough to deliver in sufficient quantities to sustain a PERCA reactor. Hence, ethane appears to be the most suitable radical chain carrier alternative to CO. Wood et al.[131] appear to have arrived at the same conclusion and chose ethane for their PERCA reactor.

A major point of disagreement between this modelling study and that of Wood et al.[131] is the time it takes for radical chemistry to conclude: In the Wood et al. model, the chemistry concludes after ~0.25 s, whereas in the model utilized for this work, the chemistry concludes after ~1 s (Figure 4.11 blue traces). This disagreement may arise partially due to the inclusion of a much more detailed and explicit chemical scheme in this work. Additionally, Wood et al. initiated their model with 10^6 molecules cm^{-3} of HO and $C_2H_5O_2$ and 10^5 molecules cm^{-3} of C_2H_5O to simulate typical ambient air abundances. This appears to reduce the initial spike in HO radical concentrations and may cause resultant chemistry to subside sooner.

Upon the addition of heat, the CL is expected to decrease because reactions of NO with peroxy radicals have negative activation energies (Table 4.1). This reduced NO reactivity leads to lower radical mixing ratios and ultimately reduces amplification and in turn limits of detection.

The simulations in this chapter suggest that TD-PERCA with ethane as a chain carrier is feasible and will provide modest CLs. Furthermore, TD-PERCA is expected to be less sensitive to relative humidity. A large uncertainty in the model are wall loss rates as high temperature experimental data are not available. If radicals behave differently upon collision with the hot walls of a TD-

PERCA reactor, these wall losses may be reduced. This would lead to improved CLs in a TD-PERCA reactor, increasing CL to beyond that achievable in a room temperature PERCA reactor.

4.5 Conclusion

A modelling study was conducted examining the effectiveness of different PERCA radical chain carriers. Dimethyl ether or ethane both produced adequate chain lengths in the simulations and are viable alternatives to CO. The effect of temperature on radical chain length for an ethane based TD-PERCA reactor was also examined. Increased temperature in the PERCA reactor leads to slower radical chemistry, and reduces chain lengths. Increased temperatures reduce the effects of relative humidity and interfering radical chemistry. However, the temperature dependence of wall losses remains unclear and needs to be assessed prior in future experimental and modelling work. A similar TD-PERCA modelling study should be performed on dimethyl ether to assess its suitability as a chain carrier at elevated temperature.

Chapter Five: Development of a thermal dissociation peroxy radical chemical amplification cavity ring-down spectrometer

In this chapter, the design and development of a thermal dissociation peroxy radical chemical amplification cavity ring-down spectrometer (TD-PERCA-CRDS) is described. A TD-PERCA-CRDS instrument was built, characterized, and the amplification factor was calibrated at 250 °C. The measurement of peroxy nitric acid (PNA) and peroxy acyl nitrates (PAN), species of atmospheric importance, with TD-PERCA-CRDS is explored.

5.1 Introduction

The RO_x (= HO + HO_2 + ΣRO_2) radicals and the nitrogen oxides (NO_x = NO + NO_2) are important trace constituents of the atmosphere that drive diverse processes such as the photochemical production of O_3 in the troposphere,[104-105] the catalytic destruction of O_3 in the stratosphere,[106-107, 151-152] and the chemistry of organic aerosol formation.[108-110] In the troposphere, the concentrations of these species are frequently buffered by RO_x and NO_x reservoir species, of which peroxynitric acid (PNA, HO_2NO_2), alkyl peroxy nitrates such as methyl peroxynitrate ($CH_3O_2NO_2$, MPN), and the peroxyacyl nitrates (PANs, $RC(O)O_2NO_2$) are important examples.[153-154] Much insight into RO_x and NO_x chemistry has been gained by measuring the atmospheric abundances of these reservoirs. Significant PNA concentrations, for example, have been observed in the polar regions,[155-157] aloft in the free and upper troposphere,[158-159] in highly polluted environments such as the Uintah basin in winter,[160] and in urban atmospheres,[161-162] and have given valuable insights into radical budgets at these locations. The PANs and PNA are prone to thermal dissociation, such that higher concentrations are more commonly observed in cold regions, aloft in the free / upper troposphere, or in winter (Table 5.1). On the other hand, their rate

of production is greater in summer as the actinic flux intensifies. Mixing ratios of PNA peak in the range from 10s to a few 100s of parts-per-trillion by volume (pptv, 10^{-12}) and those of peroxyacetic nitric anhydride (PAN; $CH_3C(O)O_2NO_2$) can exceed ten ppbv.[163]

Table 5.1 Typical* PNA and PAN mixing ratios in various environments where both were quantified

Location	PNA (pptv)	PAN (pptv)	PNA/PAN
Antarctica - Summer	20 [155]	15.6 [164]	1.3
Antarctica - Summer	22 [157]	15.6 [164]	1.4
Antarctica – Summer	2.5 [157]	9.2 [165]	0.27
Remote troposphere – Spring	-	-	0.13** [159]
Free troposphere (Intex-NA) - Summer	45 [158]	280 [166]	0.16***
Uintah Basin – Winter 2013	500 [160]	2000 [167]	0.25
Uintah Basin – Winter 2014	100 [160]	300 [168]	0.33
Atlanta – Winter	3.7 [162]	640-800 [169]	<0.01
Atlanta – Summer	11.7 [162]	640-800 [169]	0.01-0.02

* Average values

** calculated assuming all non-PAN and PPN peroxy nitrate is PNA.

*** Averages of data posted on ftp://ftp-air.larc.nasa.gov/pub/INTEXA/DC8_AIRCRAFT/

There is ongoing interest to develop improved techniques for quantification of PANs[170-173] and PNA.[159-162] TD methods such as TD coupled to laser-induced fluorescence (TD-LIF),[60, 171, 174] to cavity ring-down spectroscopy (TD-CRDS),[55, 65, 71, 175-177] or to cavity phase-shift spectroscopy (TD-CAPS)[178] detection of NO_2 are attractive as they can be used to monitor all components of odd nitrogen (NO_y) in parallel, including NO_2 (inlet operated at ambient temperature), total peroxy nitrates (ΣPN = PNA + MPN + ...; inlet heated to ~100 °C), total peroxyacyl nitrates (ΣPAN =

PAN + peroxypropinoic nitric anhydride ($C_2H_5C(O)O_2NO_2$ + ...; ~ 250 °C), total alkyl nitrates + $ClNO_2$ (ΣAN; ~ 420 °C), and HNO_3 (~ 600 °C), by deploying multiple detection channels and setting appropriate inlet temperatures. Molecules such as NO and HONO can be quantified through addition of O_3 following TD.[79, 177, 179]

When used in polluted (i.e., high-NO_x) environments, however, a drawback of the TD methods is that quantification of ΣPN (and, to a lesser degree, also of ΣPAN) is compromised because of the large error introduced from subtraction of the NO_2 background, which is often 2 – 4 orders of magnitudes larger than the ΣPN abundance. In such high-NO_x environments, on the other hand, mixing ratios of RO_x radicals are generally much smaller, < 100 pptv,[131] than those of NO_2, such that a better strategy may be to quantify the peroxy and peroxyacyl radicals generated in in stoichiometric amounts during TD of ΣPN and/or ΣPAN rather than NO_2.

The RO_x radicals may be quantified by chemical ionization mass spectrometry (CIMS);[180-184] in fact, a TD-CIMS method has been developed to quantify PAN by titrating the peroxyacetyl radical with iodide reagent ion.[183] Other RO_x radical detection methods include LIF[185-188] and PERCA coupled to NO_2 detection.[113-114, 119, 126-127] The PERCA method is attractive as it allows the infrastructure of existing TD instruments with NO_2 detection to be utilized.

The measurement of peroxy radicals by PERCA is prone to interferences (see Chapter 4). For instance, a key operational parameter of any PERCA instrument is the radical chain length or amplification factor (CL), which must be carefully calibrated. Both experimental and theoretical data (Chapter 4) show that the CL is suppressed by water vapour, whose presence increases the rates of radical loss on the inner walls of the PERCA chamber and the rates of certain gas-phase reactions, e.g., the reaction between the hydroperoxyl radical - water dimer ($HO_2 \cdot H_2O$) with NO to peroxynitrous acid (HOONO) which isomerizes to nitric acid ($HONO_2$).[118, 132, 133]

The most obvious way to minimize wall reactions and to prevent weakly bound clusters such as $HO_2 \cdot H_2O$ from forming is to apply heat. When quantification of ambient RO_x radicals is the goal, this is avoided to prevent TD of ΣPN or ΣPAN (which are more abundant than free RO_x radicals) as these molecules would interfere.[118] On the other hand, if measurement of ΣPN or ΣPAN is desired (such as in this chapter), this interference is turned into a measurement principle. Only one previous attempt to quantify peroxy nitrates in this manner was found in the literature: Blanchard et al. thermally decomposed PAN eluting from a chromatographic column in the presence of NO and CO and quantified the amplified NO_2 using luminol chemiluminescence.[189]

In this chapter, the feasibility of selectively quantifying ΣPN and ΣPAN through their respective peroxy radical TD fragments by thermal decomposition peroxy radical chemical amplification cavity ring-down spectroscopy (TD-PERCA-CRDS) was probed. The instrument uses a 405 nm blue diode laser CRDS[65] to monitor NO_2 and the ethane-based chemical amplification scheme described by Wood et al.,[131] chosen because of ethane's lower toxicity compared to CO. Thermal dissociation profiles were determined for PAN, PPN, and PNA. Quantification of trace levels of PAN, PPN, and PNA by TD-PERCA-CRDS is demonstrated and compared to parallel measurements by iodide CIMS. The suitability of TD-PERCA-CRDS as a highly sensitive (sub-pptv) ΣPN and ΣPAN detection method for ambient measurements is discussed.

Table 5.2 List of chemical reactions relevant to TD-PERCA-CRDS of PANs*

Number	Reaction	k (cm^3 $molecule^{-1}$ s^{-1})	k_{298K} (cm^3 $molecule^{-1}$ s^{-1})
R5.1	$CH_3O_2 + NO \rightarrow CH_3O + NO_2$	$2.3\times10^{-12} \times e^{(360/T)}$	7.7×10^{-12}
R5.2	$CH_3O + O_2 \rightarrow HCHO + HO_2$	$7.2\times10^{-14} \times e^{(-1080/T)}$	1.9×10^{-15}
R5.3	$HO_2 + NO \rightarrow HO + NO_2$	$3.5\times10^{-12} \times e^{(270/T)}$	8.5×10^{-12}
R5.4	$C_2H_6 + HO + O_2 \rightarrow H_2O + C_2H_5O_2$	$6.9\times10^{-12} \times e^{(-1000/T)}$	2.4×10^{-13}
R5.5	$C_2H_5O_2 + NO \rightarrow C_2H_5O + NO_2$	$2.55\times10^{-12} \times e^{(380/T)} \times 0.99$***	9.1×10^{-12}
R5.6	$C_2H_5O + O_2 \rightarrow CH_3CHO + HO_2$	$2.4\times10^{-14} \times e^{(-325/T)}$	8.1×10^{-15}
R5.7	$PAN \rightarrow CH_3CO_3 + NO_2$	See Table 5.3	4.4×10^{-4} s^{-1}
R5.8	$CH_3C(O)O_2 + NO \rightarrow NO_2 + CH_3C(O)O \rightarrow NO_2 + CH_3 + CO_2$	$7.5\times10^{-12} \times e^{(290/T)}$	2.0×10^{-11}
R5.9	$PPN \rightarrow C_2H_5CO_3 + NO_2$	See Table 5.3	3.7×10^{-4} s^{-1}
R5.10	$C_2H_5CO_3+NO+O_2 \rightarrow C_2H_5O_2+NO_2+CO_2$	$6.7\times10^{-12} \times e^{(340/T)}$	2.1×10^{-11}
R5.11	$HO + NO + M \rightarrow HONO + M$	$7.4\times10^{-31} \times (T/300)^{-2.4} \times [M]$	9.7×10^{-12} **
R5.12	$HO_2 + NO_2 + M \rightarrow HO_2NO_2 + M$	(termolecular)	(termolecular)
R5.13	$HO_2 + HO_2 + M \rightarrow H_2O_2 + M$	(termolecular)	(termolecular)
R5.14	$CH_3CO_3 \rightarrow 0.7\ CH_3CO_2 + 0.3\ CH_3CO_2H$	$5.0\times10^{-12} \times \sum RO_2$	$5.0\times10^{-12} \times \sum RO_2$
R5.15	$C_2H_5CO_3 \rightarrow 0.7\ C2H_5CO_2 + 0.3\ C_2H_5CO_2H$	$5.0\times10^{-12} \times \sum RO_2$	$5.0\times10^{-12} \times \sum RO_2$
R5.16	$CH_3O_2 \rightarrow 0.330\ CH_3O + 0.335\ HCHO + 0.335\ CH_3OH$	$1.8\times10^{-13} \times e^{(416/T)} \times \sum RO_2$	$7.4\times10^{-13} \times \sum RO_2$
R5.17	$C_2H_5O_2 \rightarrow 0.6\ C_2H_5O + 0.2\ CH_3CHO + 0.2\ C_2H_5OH$	$3.1\times10^{-13} \times \sum RO_2$	$3.1\times10^{-13} \times \sum RO_2$

* Rate constant expressions are from the Master Chemical Mechanism (MCM),[138-139] version 3.3.1, except R7 and R9, which are from Kabir et al. [140]

** calculated using $[O_2] = 4.2\times10^{18}$ molecules cm^{-3}

5.2 Experimental Section

5.2.1 TD-PERCA-CRDS

The CRDS instrument utilized for these experiments is a 4-channel CRDS instrument as opposed to the 2-channel instrument described in chapter 2. The instrument was constructed by a previous member of the Osthoff group. Details including schematics of the CRDS used are shown in section 3.2.1 and figure 3.1 of the Odame-Ankrah Thesis.[190] Briefly, the instrument consisted of four identical channels. The channels are longer than those used in the 2-channel instrument measuring 111 cm in length (92 cm are filled with the sample). The channel have been used to monitor NO_x (= NO + NO_2), NO_2, ΣPN and ΣAN in parallel.[190] Mixing ratios of NO_x are quantified by adding an excess of O_3 (which titrates NO to NO_2) to the sample flow prior to detection.[179] Mixing ratios of ΣPN and ΣAN are quantified by difference following thermal dissociation to NO_2 in quartz channels heated to 250 °C and 450 °C, respectively.[55] Each channel was connected to a MFC set to a flow rate of ~0.84 slpm.

The blue diode laser (Power Technologies, model IQu2A105(405-120)G26/8983) was square-wave on/off modulated at a frequency of 1 kHz, and 1000 ring-down decay traces were co-added to yield 1 s data. Furthermore, τ_0 and τ were determined using the LRS algorithm.[54, 67] In the single-channel version (section 5.2.1.1 and Figure 1A), all four CRDS cells were connected to sample the gases exiting the single-channel TD-PERCA inlet, though in principle a single CRDS detection channel would have sufficed to carry out the measurements. In the dual-channel version (section 5.2.1.2 and Figure 5.1B), one unheated CRDS channel was tee'd into the sample line prior to the PERCA heater to monitor NO_2 plus NO_2 generated from oxidation of NO by O_3. In the four-channel differential temperature version (section 5.2.1.3), three PERCA chambers were

connected to CRDS cells and operated in parallel, while the fourth CRDS cell was run as a reference.

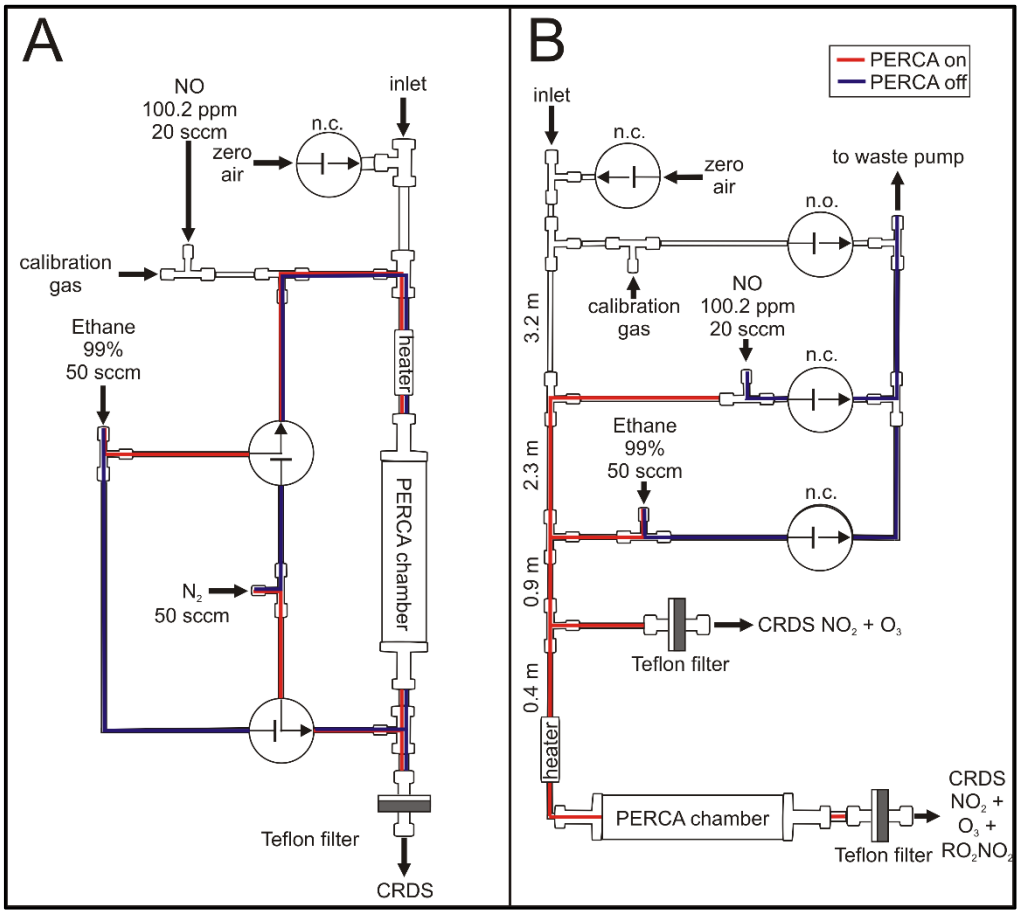

Figure 5.1 Schematics of thermal decomposition peroxy radical chemical amplification inlets. (A) Single-channel version used in initial lab experiments. The inlet consisted of a 60 cm long, 0.635 cm (¼") o.d. quartz heater and an 80 cm long, 1.27 cm (½") o.d. FEP Teflon™ reaction chamber. Reagent gases were added to either side of the reaction chamber via two 3-way solenoid valves and Teflon™ tubing. (B) Dual-channel TD-PERCA inlet. Reaction gases were added upstream of the PERCA chamber by closing the normally open valves connected to a waste pump via 50 µm critical orifices. Background NO_2 levels were monitored in a parallel detection channel by tapping into the inlet prior to thermal dissociation of peroxy nitrates.

5.2.1.1 Single-channel inlet

The majority of the experiments described in this chapter were conducted using a single-channel TD-PERCA inlet (Figure 5.1A). This configuration is reminiscent of early PERCA instrument designs in that the addition of the hydrocarbon reagent gas is alternated between points prior and after the main reaction chamber.[114-115] Nitric oxide in N_2 (100.2 ppmv, Scott-Marrin, Riverside, CA) was scrubbed of NO_2 by passing through iron(II) sulfate heptahydrate (99%, Sigma-Aldrich, Oakville, ON) prior to being combined with either a flow N_2 gas (Praxair) or ethane (CP grade, 99%, Matheson, Baskin Ridge, NJ). The gas mixture was directed towards the 80-cm long PERCA chamber (1.27 cm or ½" o.d.). When NO and N_2 were mixed prior to the PERCA chamber, a "PERCA off" signal was observed, and ethane was added after the PERCA chamber to maintain constant flow (and pressure) through the system. Conversely, when NO and ethane were directed towards the PERCA chamber a "PERCA on" signal was observed. To maintain flows and pressures through the system during "PERCA on" mode, N_2 was added to the inlet at an addition point after the PERCA chamber.

The inlet was connected to a four-channel CRDS described elsewhere.[190] Briefly, concentrations of NO_2 were monitored via its absorption at 405 nm.[65] A flow containing ppmv levels of O_3 in O_2 was added to one CRDS channel to monitor NO_x.[179] Each channel was connected to a MFC set to a flow rate of ~0.84 slpm. All four CRDS cells were connected to sample the gases exiting the single-channel TD-PERCA inlet, though in principle a single CRDS detection channel would have sufficed to carry out the measurements.

When radical free "zero" air was sampled with the single channel inlet, a negative offset (up to 1 ppbv) was observed when the 3-way solenoid valves were switched from PERCA "on" to "off" (data not shown). This artefact was not observed with the dual channel setup (section 5.2.1.2) and

was not further investigated but may have been caused by differences in the ethane flows through the needle valve induced by pressure changes (up to 15 Torr) during switching between PERCA on and off.

5.2.1.2 Dual-channel TD-PERCA-CRDS

Time resolution, signal-to-noise, and subtraction of background NO_2 can be significantly improved in a PERCA instrument by implementing dual detection channels where both amplified and background signals are simultaneously monitored.[119, 130] The dual channel TD-PERCA setup used in this work is shown in Figure 5.1B. The NO reagent gas is added at the same flow rate and concentration as in the single-channel version near the tip of the inlet (after the zero air and calibration gas ports). The residence time prior to the ethane addition point (~2.0 s) suffices to destroy RO_x radicals (via reaction with NO) prior to chemical amplification. Addition of either NO or ethane is on/off modulated using 2-way normally-open valves connected to a pump via 50 μm critical orifices (Lenox Laser, Glen Arm, MD) in a similar fashion as described earlier.[62]

A portion of the sample flow of ~0.74 slpm was diverted prior to TD to monitor the "background" NO_2 concentration in one CRDS channel. The remaining flow (~2.2 slpm) was passed through the heated quartz tube and PERCA chamber as described earlier and sampled by the other three CRDS channels to monitor background NO_2 plus the amplified NO_2 signal.

5.2.1.3 Four-channel differential temperature TD-PERCA-CRDS

An instrument with four identical measurement channels was set up to enable simultaneous quantification of NO_2, NO_2 + ΣPN and NO_2 + ΣPN + ΣPAN. This version was similar to dual channel setup described above and simply added two additional PERCA chambers; all three

PERCA chambers were connected to separate CRDS channels. The quartz PERCA chamber was replaced with three identical 1.27 cm (1/2") o.d. and 0.95 cm (3/8") i.d. Teflon™ tubes externally heated using stretch-to-fit heaters (Watlow, St. Louis, MO) to 60, 80 and 100 °C, respectively. A common inlet filter was placed between the PERCA chambers and the ethane addition point. A flow restriction was placed ahead of the common filter to achieve a pressure of 380 - 400 Torr at a flow rate of 0.8 slpm per channel (total flow rate ~3.2 slpm).

5.2.2 Chemical ionization mass spectrometry

The CIMS and its operation have been described elsewhere.[191-193] For measurements of PAN or PPN, the instrument was operated with iodide reagent in declustering mode (collisional dissociation chamber voltage = -24.7 V) and sampled through a short section of 1.27 cm (½") o.d. PFA Teflon™ tubing heated to 190 °C. The inlet flow was diluted with nitrogen saturated with water vapour to maintain a minimum RH of ~16% with the ion-molecule reaction region (IMR). PAN and PPN were quantified using the acetate and propionate ions (*m/z* 59 and 73). Ion counts were normalized to 10^6 reagent ion counts prior to presentation. Normalization prior to applying calibration factors (calculated with normalized data) removes the necessity to recalibrate as the reagent ion source output changes. The instrument response factor for PAN was calibrated against TD-CRDS[192] and was 11±3 Hz $pptv^{-1}$.

For PNA measurements, the CIMS was operated with an ambient temperature inlet and in clustering mode (collisional dissociation chamber voltage = -8.9 V); under these conditions, ~5×10^5 I^- and ~2×10^4 $I^-\cdot H_2O$ ions were observed. Mixing ratios of PNA were monitored primarily using NO_3^- at *m/z* 62, which is formed via PNA decomposition within the IMR.[193] The $HNO_3\cdot I^-$ and $HO_2NO_2\cdot I^-$ clusters at *m/z* 190 and *m/z* 206[160, 162] were also monitored.

The PNA response factors were determined using TD-CRDS (i.e., without added PERCA gases) with its inlet operated at 120 °C (Figure 5.2). Assuming that one equivalent of NO_2 is generated for each PNA molecule thermally dissociated, the CIMS response factors, normalized to 10^6 I^- counts, were 34.7±0.2 Hz $pptv^{-1}$ and 0.023±0.002 Hz $pptv^{-1}$ at *m/z* 62 (NO_3^-) and 206 ($HO_2NO_2 \cdot I^-$), respectively. These response factors are consistent with calibration factors by other groups,[160, 162] with the low response at *m/z* 206 rationalized by the low number of $I^- \cdot H_2O$ ions. Even though the CIMS response at *m/z* 62 is not specific,[193] it was used in the laboratory experiments presented here to monitor PNA rather than *m/z* 206 because of its larger response factor and thus higher sensitivity.

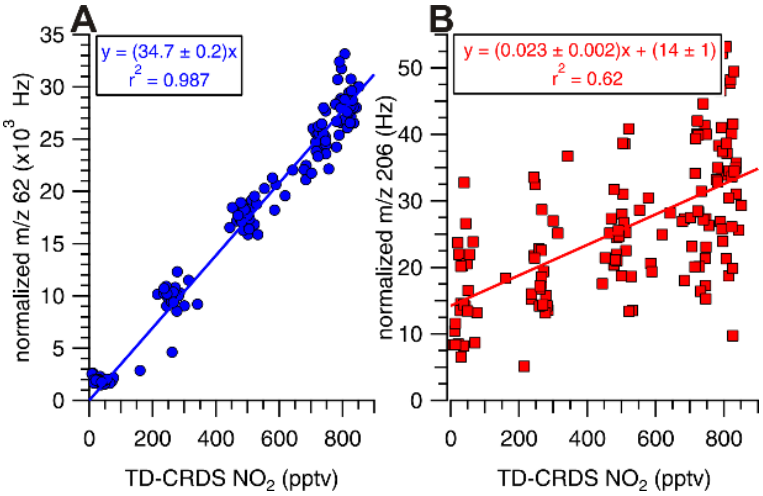

Figure 5.2 Calibration of CIMS response factors against TD-CRDS operated with its inlet heated to 120 °C and without amplification. (A) *m/z* 62 (NO_3^-). (B) *m/z* 206($HO_2NO_2 \cdot I^-$). CIMS counts were normalized to 10^6 I^- counts.

5.2.3 Synthesis and delivery of PAN and PPN

The synthesis of PAN and PPN from their corresponding anhydrides was described earlier.[192, 194] Aliquots in tridecane were stored in 2.0 mL centrifuge tubes (VWR) in a freezer until needed.

To separate PAN and PPN from impurities generated during synthesis and storage (i.e., NO_2, HNO_3 and alkyl nitrates),[195] a preparatory scale GC setup (Figure 5.3) was used.

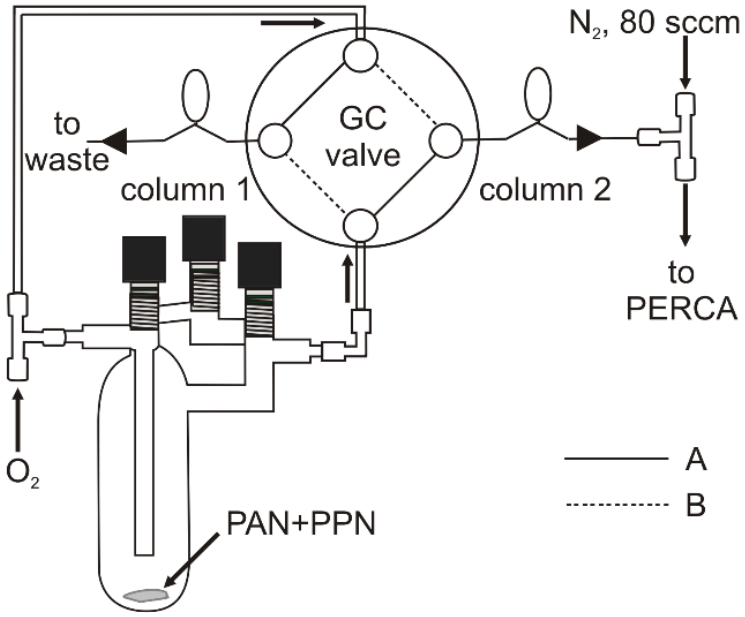

Figure 5.3 Setup for delivery of PAN and PPN using a gas chromatography column.

First, the contents of two tubes containing PAN and PPN in tridecane were combined in a 3-valve glass vessel. This vessel was connected to a 2-position GC-Valve (VICI Valco EH4C10WE, Houston, TX) and mildly pressurized (~0.1 atm above ambient) using oxygen (Praxair) delivered through a 10 μm critical orifice. Two megabore capillary gas chromatography (GC) columns (Restek RTX-1701, 0.53 mm i.d., 1.00 μm film thickness, State College, PA) of equal lengths (3 m) were connected to the ports adjacent to the one connected to the glass vessel. The outlet of one GC column was connected to the PERCA inlet, whereas the other was exhausted into a waste line. The port opposite to the glass vessel was also pressurized with oxygen such that both columns remained under flow at all times. Gases were delivered by switching the valve to position A (Figure

5.3) for ~40 s. The output of the preparatory-scale GC was diluted with ZA or air passed through a custom-built scrubber system to meet the sample flow requirements of the TD-PERCA CRDS and/or CIMS. The relative humidity (RH) of the gases delivered was monitored using a temperature/RH probe (VWR) placed inline.

The preparatory scale GC setup allowed delivery of short "bursts" of PAN and PPN. To deliver a constant and low PAN concentration over prolonged time periods, air was drawn from a 4,000 L Teflon chamber, initially filled with scrubbed (i.e., PAN-free) air and to which the head space above a PAN/tridecane solution had been added. An internal mixing fan ensured constant output.

5.2.4 Synthesis and delivery of PNA

5.2.4.1 Batch sample

A batch PNA sample was synthesized from reaction of nitronium tetrafluoroborate (NO_2BF_4; Sigma-Aldrich) with H_2O_2 as described by Chen et al.[162] Briefly, a 50% H_2O_2 solution (Sigma-Aldrich) was concentrated using a gentle N_2 flow over a period of several days. A small aliquot (200 µL) of concentrated H_2O_2 was placed in a 3-valve glass vessel cooled to 0 °C using an external circulating chiller, and 120 mg of NO_2BF_4 were added. The headspace of the glass vessel was flushed with a 50 sccm flow of N_2 delivered by a MFC. This flow delivered very high concentrations and contained substantial and variable amounts of impurities (mainly HNO_3), even when the vessel temperature was lowered to -20 °C. The batch sample was used to calibrate the CIMS against TD-CRDS (Figure 5.2A).

5.2.4.2 Photolysis source

Gas flows containing low and reproducible concentrations of PNA were generated dynamically in a similar fashion to the method described by Veres et al.[160] by combining the output of a HO_2 photochemical source with NO_2. Ultrapure N_2 (Praxair) was passed through a bubbler filled with deionized water at a flow rate of 100 sccm and combined with 2 sccm of O_2 (Praxair). This mixture was passed through a ¼" (0.635 cm) o.d. quartz tube partially illuminated by a low-pressure 185 nm mercury quartz lamp (Jelight 95-2100-2, Irvine, CA). This generated a mixture of O_3 (~30 ppbv after dilution), HO and HO_2, whose concentrations were controlled with a sliding metal sleeve (VWR) which modified the length of the quartz tubing that was illuminated. This flow was combined with between 4 and 16 ppmv NO_2 to yield a gas mixture containing PNA which was immediately (< 5 cm tube length) diluted with zero or scrubbed air flowing at a rate slightly greater than the amount sampled by the instruments. The NO_2 gas stream was generated by mixing between 1.4 and 3.0 sccm of NO (100.2 ppmv in N_2; Scott-Marrin, Riverside, CA) with a slightly less than stoichiometric amount of O_3 in ~20 sccm O_2, generated by illuminating O_2 with a low-pressure 254 nm mercury quartz lamp (Jelight).

5.3 Results

5.3.1 Thermal dissociation profiles

The TD profiles of PNA, PAN, and PPN were measured by TD-CRDS (i.e., without amplification) with the single-channel inlet and are shown in Figure 5.4. The superimposed trend lines are simulations based on the TD model introduced by Paul et al.[55] and the Arrhenius parameters in Table 5.3 and are consistent with the observations. The TD profiles of PNA and PAN/PPN partially overlap and are consistent with the 5%/95% ranges given in Figure 3 of Wooldridge et al.[171] PNA and PAN or PPN fully dissociated at temperatures of 120 °C and 250 °C, respectively. These temperatures were used in subsequent experiments when complete dissociation of either PNA or PAN/PPN was desired. Also shown in Figure 5.4 is the TD-PERCA-CRDS signal observed when sampling O_3, a potentially interfering species (see section 5.3.9.1).

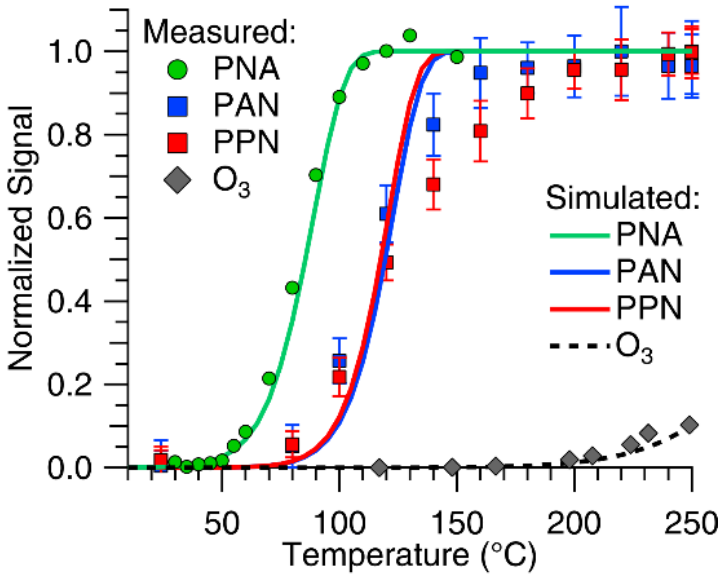

Figure 5.4 Normalized thermal dissociation profiles of PNA, PAN, PPN, and O_3 as a function of inlet set temperature. Superimposed trend lines are simulations based on the TD model introduced by Paul et al. [55]. The PNA, PAN, and PPN data were observed by TD-CRDS without amplification gases present, whereas the O_3 data were observed by TD-PERCA-CRDS. The error bars represent standard deviations of 1 s data.

Table 5.3 Arrhenius parameters for thermal dissociation of selected PN, PAN, PPN, and O_3.

Molecule	A (s^{-1})	E_a (kJ mol^{-1})	Reference	T needed to dissociate 99.9% (°C) **
HO_2NO_2 (PNA)	7.3×10^{14} *	88.1±4.4	[196]	123
$CH_3O_2NO_2$ (MPN)	1.1×10^{16}	88.1±4.4	[196]	86
$C_2H_5O_2NO_2$ (EPN)	8.8×10^{15}	86.5±8.7	[196]	82
$CH_3C(O)O_2NO_2$ (PAN)	2.8×10^{16}	113±2	[140]	174
$CH_3C(O)O_2NO_2$ (PPN)	2.36×10^{16}	113±2	[140]	176
O_3	1.26×10^{10} *	92.8	[197-198]	180***

* Calculated assuming a pressure of 550 Torr and temperature of 298 K.

** Assuming a contact time of 4 ms at the maximum temperature[55]

*** T needed to dissociate 0.1%

5.3.2 Measurement of PAN and PPN by TD-PERCA-CRDS

A time series demonstrating amplification of PAN and PPN in the TD-PERCA-CRDS operated with its inlet at 250 °C is shown in Figure 5.5. In this experiment, PAN and PPN were delivered via the preparatory-scale GC (Figure 5.3), and the single-channel setup (section 5.2.1.1) was used.

PAN and PPN eluted from the GC column after 3 min and 6 min, respectively. The compounds eluted as plateaus because of the relatively long injection time. In Figure 5.5A, PAN and PPN are observed only by the heated (NO_2+ ΣPAN) TD-CRDS channel, where they quantitatively (see Figure 5 of Paul, et al. [55]) decompose to NO_2 at mixing ratios of 2.00±0.09 ppbv and 1.86±0.12 ppbv, respectively (errors are 1 σ of 1 s data). After the PERCA heater was set to 250

°C as well, similar amounts of NO_2, 2.04±0.09 ppbv and 1.97±0.12 ppbv, were observed in the ambient temperature channel for PAN and PPN, respectively. Marginally higher amounts were observed in the heated CRDS channel (2.42±0.10 and 2.06±0.14 ppbv) (Figure 5.5B). The lower amounts observed in the unheated CRDS channel result from recombination of peroxyacyl radicals with NO_2 (mostly in the unheated PERCA chamber), which suppresses the signal in the unheated CRDS channel but not in the heated one. Hence, the NO_2 + ΣPAN data are a more accurate measure of the PAN and PPN concentrations delivered.

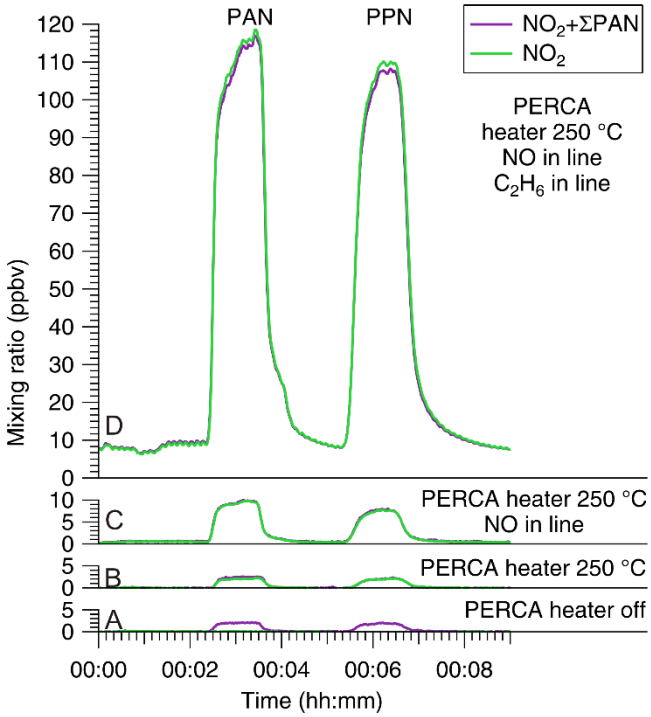

Figure 5.5 Peroxy radical chemical amplification of peroxyacetic and peroxypropionic nitric anhydride (PAN and PPN) delivered via a megabore GC column. (A) Time series of the signal observed by cavity ring-down spectroscopy in the ambient temperature (NO_2; green colour) and heated (NO_2 + ∑PAN; purple colour) channels with the PERCA heater off. (B) Same as (A) with the PERCA heater switched on. (C) Same as (B) with 0.75 ppmv NO added. (D) Same as (C) with 1.5% C_2H_6 added. The amplification factor is determined from the ratio of the ambient temperature (i.e., NO_2) CRDS signal observed in (D) divided by that observed in (B).

Because PAN and PPN dissociate with 1:1 stoichiometry, the amount of peroxyacyl radicals produced during thermal dissociation is the same as the amount of NO_2 generated. When ~0.75 ppmv of NO was added (Figure 5.5C), the peroxyacyl and, subsequently, the methyl (or ethyl) peroxy, and the hydroperoxyl radicals oxidize NO to NO_2 (reactions R5.8/R5.10, R5.1/R5.5, and R5.3; Table 5.2) and the NO_2 signal relative to the signal obtained in the absence of NO is amplified by a factor of four. The ratios observed (Figure 5.5C relative to Figure 5.5B) were

4.0±0.2 and 3.8±0.3 for PAN and PPN, respectively, and are consistent with earlier observations at lower NO mixing ratios (i.e., Figure 6 of Paul and Osthoff).[65]

Next, NO and ethane were added at mixing ratios (0.75 ppmv NO and 1.5% C_2H_6) that Wood et al.[131] determined to be optimal for ambient temperature PERCA. Under these conditions, the signals amplified to 116.0±1.3 ppbv and 109.3±0.7 ppbv (Figure 5.5D), corresponding to CLs (relative to Figure 5.5B) of 48±2 and 53±4 for PAN and PPN, respectively.

In the presence of ethane, marginally lower NO_2 concentrations (98.7% and 98.1%) were observed in the heated, NO_2 + ΣPAN TD-CRDS channel (compared to the absence of ethane). Partial scrubbing of NO_2 in heated quartz cells has been anecdotally observed in our group's and also others' (e.g. Womack, et al. [177]) TD instruments; this effect varies between quartz cells and with sample history. Since the effect was relatively minor, it was neglected in this work.

5.3.3 Optimization of TD-PERCA amplification factors

Sequences as shown in Figure 5.5 were used to determine conditions leading to optimum amplification factors. The largest amplification factors were obtained with an ethane mixing ratio of ~1.6% - 1.7%.

Figure 5.6 shows how the chain length varies with NO mixing ratio. In the absence of ethane, amplification factors of ~4 were observed (Figure 5.6, open symbols), consistent with the results shown in Figure 5.5C. When 1.7% ethane were added, the amplification factor increased with NO mixing ratio up to a maximum at 550±150 ppbv and then decreased, qualitatively consistent with the results reported by Wood et al.[131]

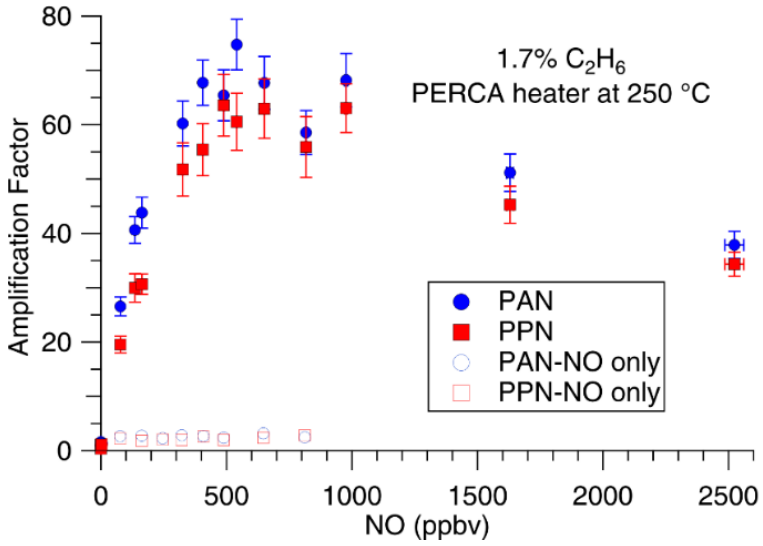

Figure 5.6 TD-PERCA-CRDS amplification factors of ~0.5 ppbv PAN and ~1.3 ppbv PPN as a function of NO mixing ratio at RH = 0%. The error bars represent standard deviations of 1 s data.

The amplification factors shown in Figure 5.6 were slightly larger for PAN than for PPN mainly because the PPN mixing ratio of ~1.3 ppbv exceeded the optimum concentration range for PERCA (see section 5.3.5.2).

5.3.4 Measurement of PNA by TD-PERCA-CRDS and CIMS

A sample time series showing TD-PERCA-CRDS measurements of photochemically generated PNA in scrubbed air is presented in Figure 5.7. Here, the TD-PERCA-CRDS was operated with the dual channel inlet (Figure 5.1B) at 120 °C and with 1.6% C_2H_6 and 316±3 ppbv of NO (suboptimal NO mixing ratios). Figure 5.7A shows the NO_2 mixing ratios in the reference, NO_2 channel (grey trace) and in the TD-PERCA-CRDS channel (green trace). In this example, the mixing ratio of PNA was changed approximately every 2 min by moving a sliding cover within the photochemical source.

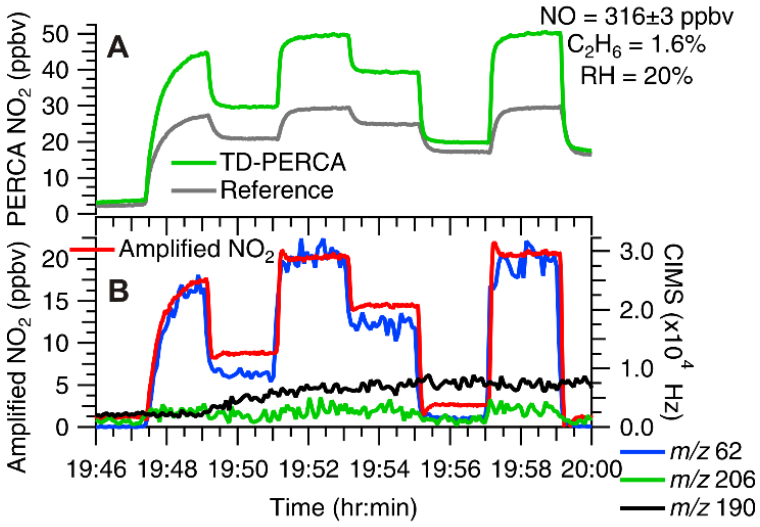

Figure 5.7 (A) Sample time series of PNA observed by TD-PERCA-CRDS in the reference, NO_2 channel (shown in green) and PERCA channel (grey). (B) (left) Difference signal between amplified and reference channel (shown in red). (right) CIMS counts (normalized to 10^6 I^-) at *m/z* 62, the major fragment (NO_3^-) expected from PNA, at *m/z* 206 (multiplied by a factor of 100 for clarity), the $HNO_4 \cdot I^-$ cluster, and at m/z 190, the $HNO_3 \cdot I^-$ cluster.

The difference between these two signals is displayed in Figure 5.7B (red trace, left-hand axis). Superimposed in Figure 5.7B (right-hand axis) are the CIMS responses at *m/z* 62 (NO_3^-), *m/z* 206 ($HNO_4 \cdot I^-$, multiplied by a factor of 100 for clarity), and *m/z* 190 ($HNO_3 \cdot I^-$).

The photochemical source co-generates HO which is lost on the inner walls of the quartz tubing or is titrated by NO_2 or (to lesser extent since less abundant) NO to HNO_3 or HONO, respectively. Conceivably, the co-generation of HNO_3 could interfere with quantification of PNA by CIMS at *m/z* 62. However, when the photolysis source was turned off at ~19:59 (Figure 5.7), HNO_3 was still observed for some time after at *m/z* 190 due to slow desorption from the inner walls of the connecting tubing, whereas the ion counts at *m/z* 62 quickly (< 10 s) returned to background values close to zero Hz, indicating that the contribution of HNO_3 to ion counts at *m/z* 62 was negligible.

The scatter plot of the TD-PERCA-CRDS and CIMS data at *m/z* 62, multiplied by the CIMS response factor determined in Figure 5.2A, is shown in Figure 5.8A as dark blue circles. The signals by the two instruments are highly correlated ($r^2 = 0.979$), consistent with both instruments measuring the same molecule, PNA. The slope of this plot (26.3±0.4) equals to the TD-PERCA-CRDS amplification factor for PNA. In contrast, the scatter plot of TD-PERCA-CRDS with the CIMS response at *m/z* 206 was unusable because of the latter's poor signal to noise ratio (Figure 5.2B).

5.3.5 Factors affecting amplification factors

The amplification factor for PNA shown in Figure 5.8A is less than observed for PAN in Figure 5.8B and for PAN and PPN under optimal conditions (Figure 5.6). Though in this particular example the lower amplification factor was due to the less than optimal amount of NO added, lower amplification factors for PNA than for PAN were generally observed, even when optimum NO mixing ratios were used.

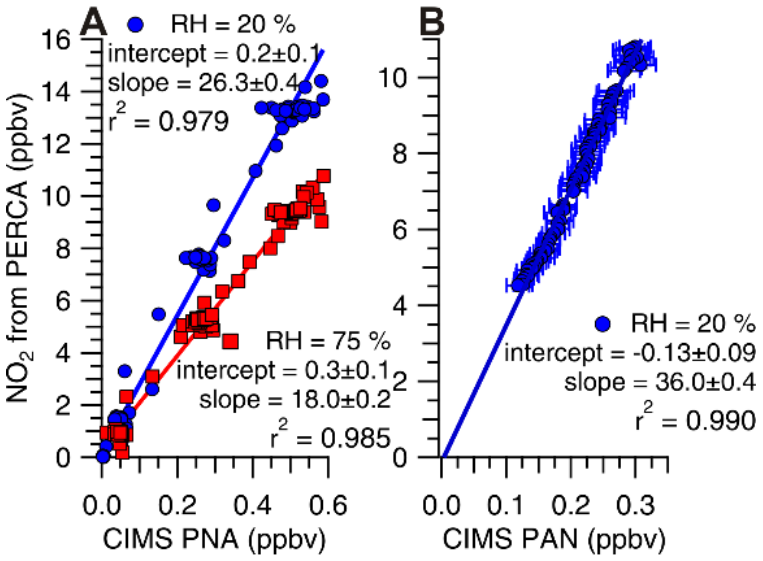

Figure 5.8 Scatter plots of TD-PERCA-CRDS and CIMS measurements. (A) Sample PNA calibrations at an NO mixing ratio of 316±3 ppbv and TD-PERCA inlet temperature of 120 °C (B) Sample PAN calibration at an NO mixing ratio of 662±2 ppbv and TD-PERCA inlet temperature of 250 °C.

The obvious difference is that different radicals, HO_2 in the case of PNA and a peroxyacyl radical ($RC(O)O_2$) in the case of PAN or PPN, are generated initially. However, in both cases, the HO_2/HO radical pair is the main carrier of the amplification, such that this initial difference should only have a marginal effect. Wood et al.[131] estimated the uncertainty arising from the range in peroxy radical reactivity to ±9%.

Experimental parameters that can affect the amplification factor include relative humidity, radical concentration, and the PERCA inlet temperature; these factors are probed separately in the following sections. In each case, the results from box model simulations presented in Chapter 4 were used to aid in the interpretation of the data.

5.3.5.1 Dependence of chain lengths on relative humidity

The experiment described in section 5.3.4 was repeated with the scrubbed air humidified to 75% RH by passing the make-up air through a bubbler. The resulting scatter plot is superimposed in Figure 5.8A (red squares). Indeed, the amplification factor for PNA was lowered from 26.3±0.4 to 18.0±0.2 when the RH was increased from 20% to 75%. Following these observations, the RH dependence was investigated systematically with TD-PERCA-CRDS operated under optimal conditions and with PAN and PPN at 250 °C inlet temperature. The results are summarized in Figure 5.9.

The amplification factor decreased by (2.0±0.6)% for every 10% increase in RH. This RH dependence is less than reported for ambient temperature PERCA: Between a RH of 0% and 50%, for example, the response of room temperature PERCA dropped by 30%,[131] whereas that of TD-PERCA decreased by 15%. A reduced RH dependence is expected as the elevated temperature suppresses formation of $HO_2 \cdot H_2O$,[143] whose reaction with NO is a major radical sink.[118, 132, 133] This interpretation is supported by box model simulations, which show a reduced RH dependence of the CL at higher temperatures (Figure 4.8). In addition, I speculate that reactions of radicals on the inner walls of PERCA tubing are reduced at higher inlet temperature.

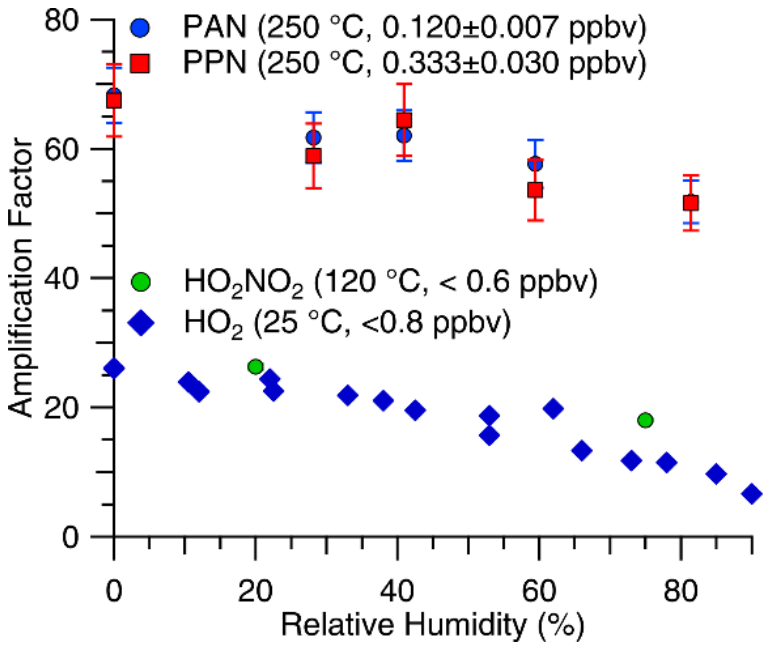

Figure 5.9 TD-PERCA-CRDS amplification factor as a function of relative humidity at an ethane mixing ratio of 1.6% and with NO mixing ratios of 644±2 and 316±3 ppbv for the PAN/PPN experiments and the PNA experiments, respectively. The PAN and PPN mixing ratios were 0.120±0.007 and 0.333±0.030 ppbv, respectively. The PNA mixing ratio was varied between 0 and 0.6 ppbv. The room temperature HO_2 data are from Wood et al. [131].

5.3.5.2 Dependence of chain lengths on radical concentration: dynamic range

It is well known in the PERCA community that the chain lengths decrease at high radical concentrations due to radical-radical reactions. Figures 5.8A and 5.8B demonstrate that the response of TD-PERCA-CRDS is linear at low, atmospherically relevant mixing ratios (i.e., below ~0.6 ppbv). Figure 5.10 summarizes the PERCA responses as functions at larger PAN/PPN mixing ratios. The largest amplification factor, 69±5, was observed when the TD-PERCA inlet was operated at 250 °C with PAN or PPN mixing ratios ≤ 0.6 ppbv. Shorter chain lengths were observed at higher mixing ratios (e.g., 62±2 at 1.3 ppbv, 53±4 at 2.1 ppbv, and 48±2 at 2.4 ppbv, respectively). Thus, the amplification factor is concentration dependent at RO_2 mixing ratios above ~0.6 ppbv and is constant under atmospherically relevant trace conditions.

PERCA reactors utilizing CO as a chain carrier show non-linearity at RO_2 mixing ratios above ~200 pptv,[114] while room temperature ethane based PERCA have a reported linear dynamic range up to ~800 pptv.[131] The greater dynamic range with ethane arises because of lower chain lengths and radical concentrations in the reactor and hence reduced radical-radical termination reactions.[131] The linear range of the ethane TD-PERCA reactor of ~600 pptv falls in between these two extremes, as the CL and radical concentrations are greater than ethane PERCA at room temperature but less than those achievable with CO PERCA.

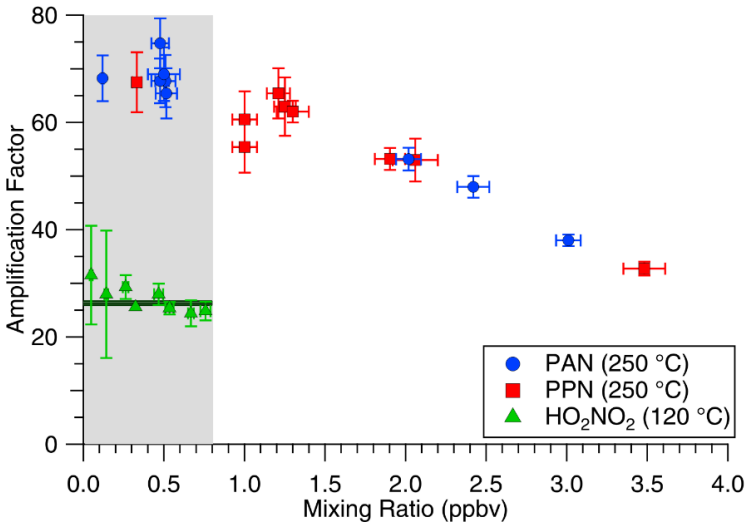

Figure 5.10 TD-PERCA-CRDS amplification factors as a function of PAN, PPN, and PNA mixing ratio. Errors bars correspond to ±1σ standard deviation. Mixing ratios of NO and ethane were 500±50 ppbv and ~1.6%, respectively. The grey underlay indicates the linear range. The dark green line corresponds to 26.3±0.4 (slope of data shown in Figure 5.8A).

5.3.5.3 Dependence of chain lengths on inlet temperature

Next, the temperature dependence of the TD-PERCA-CRDS signal when sampling photochemically generated PNA at constant RH and PNA mixing ratio was investigated.

Figure 5.11 shows such a temperature scan of ~180 pptv PNA (measured in parallel by CIMS). The non-amplified TD profile observed by TD-CRDS is superimposed for comparison.

A striking feature in Figure 5.11 is the very large increase in the amplified NO_2 signal observed at temperatures above ~150 °C. This is an artefact that arises from O_3 co-emitted by the photochemical source and is commented on further in section 5.3.9.

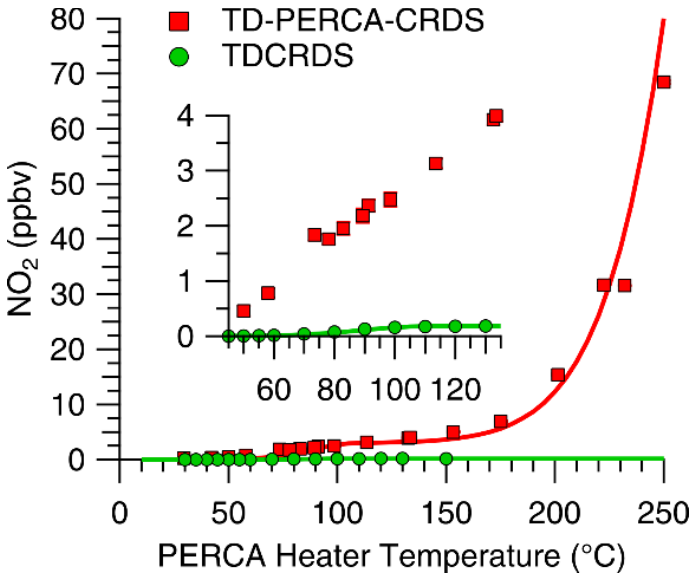

Figure 5.11 Amplification of photochemically generated PNA (red) as a function of PERCA heater temperature (RH=24%). Simultaneous quantification by CIMS and UV absorption showed that the gas stream contained 180±28 pptv PNA and 3.5±0.2 ppbv O_3. The non-amplified TD-CRDS signal (from Figure 5.4), multiplied by 0.18, is shown in green for comparison.

It is obvious from Figure 5.11 that the amplification factors are strongly dependent on inlet temperature: Even though PNA fully dissociates at temperatures > ~90 °C in our inlets (Figure 5.4), the amplified signal increased by ~60% in the region from 90 to 135 °C (Figure 5.11, insert), corresponding to amplification factors of ~15 and ~22, respectively. This increase is qualitatively consistent with the higher amplification factor observed with PAN or PPN at 250 °C.

Box model simulations (Figure 4.7) show that the CL is expected to decrease with increasing temperature, opposite to what is observed. This occurs because the chain-carrying reactions of HO_2 and RO_2 with NO (e.g., R5.3, Table 5.2) have negative activation energies and are hence slower at higher temperatures, lowering the CL. This effect is partially offset when the chemistry of $HO_2 \cdot H_2O$ is added to the mechanism (Figures 4.8 and 4.9).

5.3.6 Interferences

5.3.6.1 Interference from O_3 in the measurement of ΣPAN at 250 °C

When sampling ambient air (data not shown) or when sampling photochemically generated PNA (Figure 5.11) the amplified NO_2 increases sharply at PERCA inlet temperatures above ~150 °C. These observations can be rationalized by thermal decomposition of O_3. Even though only a small fraction of O_3 dissociates to O_2 + O at ~150 °C in the TD inlet (~0.1%; Figure 5.5),[197-198] a comparatively large signal is generated because the O atom reacts with C_2H_6 to form two radicals, HO and C_2H_5.[199] This reaction is competitive in the PERCA inlet (compared to reaction of O with O_2) because of the high C_2H_6 concentration (1.7%): The lifetime of O with respect to reaction with C_2H_6 is ~0.34 ms, which is of similar magnitude as the expected lifetime of O with respect to reaction with O_2 of ~0.15 ms.[200]

An alternate inlet configuration in which the inlet length between the NO and ethane addition points is increased to allow for sufficient residence time to completely titrate O_3 with the added NO was considered. However, at the optimum NO mixing ratio for PERCA, the 1/e lifetime of O_3 is ~6 s, making this approach unfeasible.

Hence, if O_3 is sampled with an ethane-based TD-PERCA instrument heated above 150 °C, radicals are generated that are amplified by PERCA. Since O_3 is typically present at mixing ratios

in the tens of ppbv in ambient air, quantification of ΣPAN with an ethane-based TD-PERCA-CRDS would be challenging. In contrast, TD-PERCA instruments using CO will not have this limitation, as CO reacts with O to CO_2 and would not generate RO_x radicals.

5.3.6.2 Interference from ΣPAN in the measurement of ΣPN at 95 °C – 110 °C

A temperature of 95°C (110 °C) is required to dissociate >90% (>99.9%) of PNA in the TD-PERCA inlet; at these temperatures, ~12% (~39%) of PAN dissociates (Figure 5.4). Since [PAN] > [PNA] (Table 5.1) and hence ΣPAN > ΣPN in most environments, the contribution of ΣPAN to the ΣPN signal in ambient air is substantial (and likely also variable given the slope of the PAN TD curve in this region). Hence, measurement of ΣPN in ambient air by TD-PERCA-CRDS with a single channel relative to an NO_2 background measurement is unfeasible.

5.3.7 Differential temperature TD-PERCA-CRDS for measurement of ΣPN and ΣPAN

5.3.7.1 Synthetic air mixtures

To overcome the limitations outlined in section 5.3.6, a multichannel, differential temperature approach was used. Here, two channels were operated at constant temperatures set in the 60 °C to 110 °C range to avoid the interference from O_3 dissociation and ensure that response for ΣPAN remains linear (by dissociating only a fraction of its concentration). Since the amount of NO_2 generated by TD-PERCA is a function of temperature and radical chain length (CL_T) as well as a fraction dissociated (F_T) of PNA and ΣPAN, the responses in the two PERCA channels operated at different temperatures, T1 and T2, are:

$$[NO_2]_{T1} = CL_{T1} \times F_{PAN,T1} \times [\Sigma PAN] + CL_{T1} \times F_{PNA,T1} \times [\Sigma PN] + [NO_2]_{ref} \quad (5.1a)$$

$$[NO_2]_{T2} = CL_{T2} \times F_{PAN,T2} \times [\Sigma PAN] + CL_{T2} \times F_{PNA,T2} \times [\Sigma PN] + [NO_2]_{ref} \quad (5.1b)$$

If the CL_T and F_T values are measured at temperatures T1 and T2 independently (i.e., offline), and $[NO_2]_{ref}$ is quantified in an unheated, parallel reference channel, the mixing ratios of ΣPN and ΣPAN can be calculated by rearranging equations (5.1a) and (5.1b):

$$[\Sigma PAN] = \frac{([NO_2]_{T1}-[NO_2]_{ref})\times CL_{T2}F_{PNA,T2}-([NO_2]_{T2}-[NO_2]_{ref})\times CL_{T1}F_{PNA,T1}}{CL_{T2}F_{PNA,T2}\times CL_{T1}F_{PAN,T1}-CL_{T2}F_{PAN,T2}\times CL_{T1}F_{PNA,T1}} \quad (5.2a)$$

$$[\Sigma PN] = \frac{([NO_2]_{T2}-[NO_2]_{ref})-CL_{T2}F_{PAN,T2}\times[\Sigma PAN]}{CL_{T2}F_{PNA,T2}} \quad (5.2b)$$

A time series demonstrating this approach using the four-channel setup is presented in Figure 5.12A. Here, a constant mixing ratio of PNA (along with NO_2 and O_3 from the photolysis source) was added to the inlet between 21:44 and 21:55. At 21:48:30 and at 21:50:45, PAN was added via the GC pre-column. The product of CL and F for PAN and PNA at 110 °C, 80 °C, and 60 °C were determined offline and are summarized in Table 5.4 and assumed to be the same for all ΣPN and ΣPAN species.

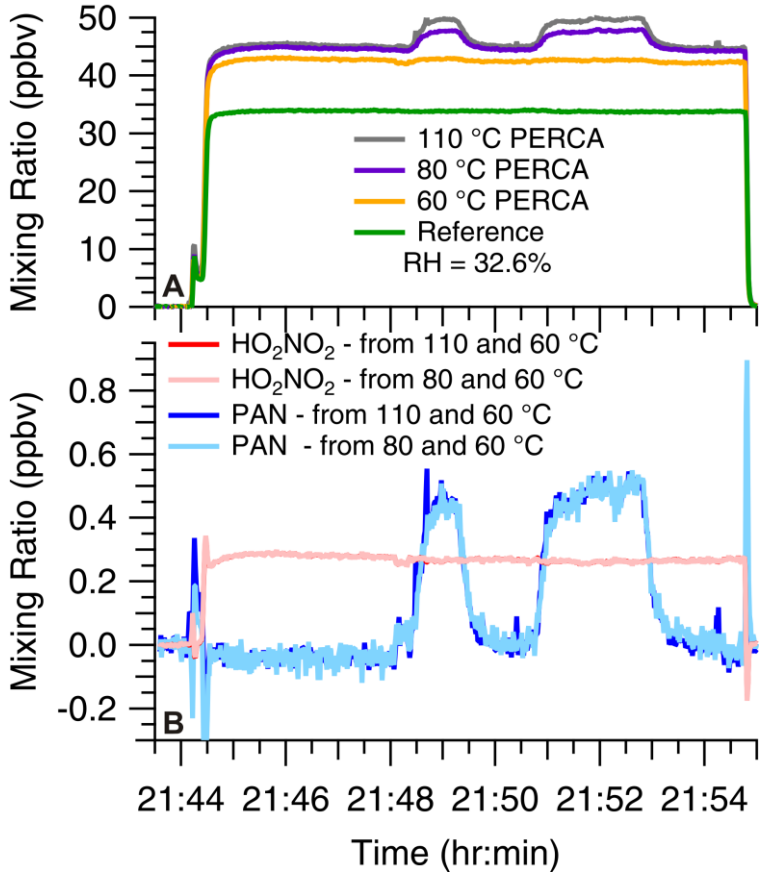

Figure 5.12 Demonstration of differential temperature TD-PERCA-CRDS. (A) Time series of NO_2 mixing ratios observed by an unheated reference channel and three TD-PERCA channels operated at 60 °C, 80 °C, and 110 °C, respectively. PNA was sampled from 21:44:30 to 21:54:45, and PAN was added at ~21:49 and ~21:52. (B) Mixing ratios of PAN and PNA calculated from (A).

Table 5.4 Products of CL and F for PNA and PAN at 110 °C, 80 °C, and 60 °C (RH = 34%)

	$CL_{110\,°C} \times F_{110\,°C}$	$CL_{80\,°C} \times F_{80\,°C}$	$CL_{60\,°C} \times F_{60\,°C}$
PNA	41.8 ± 0.2	39.5 ± 0.2	31.9 ± 0.1
ΣPAN	10 ± 1	7.6 ± 0.9	1.2 ± 0.2

Table 5.5 Statistics (average ± 1 standard deviation) of the 1 s data shown in Figure 5.12.

	PNA (pptv)			PAN (pptv)		
Time period	T1 = 110 °C T2 = 60 °C	T1 = 110 °C T2 = 80 °C	T1 = 80 °C T2 = 60 °C	T1 = 110 °C T2 = 60 °C	T1 = 110 °C T2 = 80 °C	T1 = 80 °C T2 = 60 °C
21:48:45 – 21:49:15	266 ± 4	254 ± 17	267 ± 4	447 ± 26	495 ± 75	430 ± 31
21:51:15 – 21:52:45	261 ± 5	258 ± 14	261 ± 6	480 ± 32	491 ± 68	476 ± 38

The time series of PNA and PAN mixing ratios derived from equations 5.2a and 5.2b are presented in Figure 5.12B. Consistent results were obtained independent of which pair of channels was used in the calculations (Table 5.5).

5.3.7.2 Laboratory air

The differential temperature TD-PERCA-CRDS was then used to sample and determine ΣPN and ΣPAN in laboratory air. The calibration parameters summarized in Table 5.4 were used since they were determined with scrubbed air, which has the same RH as the air intake (i.e., the laboratory). The results are summarized in Table 5.6.

Table 5.6 Statistics (average ± 1 standard deviation) of the 1 s data of laboratory air (first time period), laboratory air spiked with ~260 pptv PNA (second period), and laboratory air spiked with 260 pptv PNA and ~480 pptv PAN (third period).

	ΣPN (ppbv)			ΣPAN (ppbv)		
Time period	T1 = 110 °C T2 = 60 °C	T1 = 110 °C T2 = 80 °C	T1 = 80 °C T2 = 60 °C	T1 = 110 °C T2 = 60 °C	T1 = 110 °C T2 = 80 °C	T1 = 80 °C T2 = 60 °C
Room air	-0.08 ± 0.01	-0.29 ± 0.03	-0.068 ± 0.004	4.21 ± 0.04	5.1 ± 0.1	3.89 ± 0.03
Room air + PNA	0.19 ± 0.01	-0.03 ± 0.02	0.20 ± 0.01	3.50 ± 0.03	4.4 ± 0.1	3.17 ± 0.04
Δ(ΣPN)	0.27 ± 0.01	0.26 ± 0.04	0.27 ± 0.01			
Room air + PNA + PAN	0.19 ± 0.01	-0.02 ± 0.02	0.20 ± 0.01	3.99 ± 0.04	4.8 ± 0.1	3.70 ± 0.03
Δ(ΣPAN)				0.49± 0.04	0.40 ± 0.14	0.52 ± 0.05

The determined room air ΣPN values mixing ratios are negative (i.e., not physically possible). The ΣPAN mixing ratios are unreasonably large as such high mixing ratios have never been observed in the Osthoff group laboratory by GC, TD-CRDS, or by CIMS and suggests that there is (or are) species that dissociate in the TD inlet and generate RO_x radicals or, perhaps, atomic oxygen other than ΣPAN. These unknown interfering species seem to have different TD profiles than PAN and PNA as the differential response differs when different pairs of channels are used in the calculation. Furthermore, the response to the unknown species is more prominent when the hottest (110 °C) channel is used in the calculation.

When ~260 pptv of PNA and ~480 pptv PAN (using the same setup as for Figure 5.12 and Table 5.4) were added to the sampled laboratory air, the responses (i.e., Δ(ΣPN) and Δ(ΣPAN) are

consistent in all channels, which suggests that the chain lengths and dissociated fractions had not changed. This observation corroborates that the ethane based TD-PERCA-CRDS in reality quantifies ΣPAN*, which includes PAN, PPN, etc. plus one or more unidentified species. In section 4, the potential identity of these unknown species is discussed. It is unclear if a CO-based TD-PERCA would suffer from this interference as well.

5.3.8 Figures of merit

The ability of TD-PERCA-CRDS to detect radicals is limited by the instrument's ability to detect differences in NO_2 concentration after amplification, calculated using:[66]

$$[NO_2]_{min} = \frac{R_L}{c\sigma}\left(\frac{\Delta\tau_{min}}{\tau_0^2}\right) \quad (5.3)$$

Here, $[NO_2]_{min}$ is the smallest NO_2 concentration that can be detected, $\Delta\tau_{min}$ is the smallest measurable difference between ring-down time constants in the presence (τ) and absence (τ_0) of NO_2, c is the speed of light, σ is the NO_2 absorption cross-section at 405 nm (6.1×10^{19} cm^2 $molecule^{-1}$),[65] and R_L is a correction factor. $\Delta\tau_{min}$ is approximately:[66]

$$\Delta\tau_{min} = \sqrt{2} \times \sigma(\tau_0) \quad (5.4)$$

When sampling zero air, the LOD for NO_2 was 49 pptv (1 s, 1 σ). In the presence of NO and ethane reagent gases, the LOD increases to 87 pptv (1 s, 1 σ).

Employing the dual-channel-TD-PERCA-CRDS with the PERCA heater at 250 °C, a CL of 69 factored in, and in the absence of NO_2, the 1 s, 1 σ LOD for ΣPAN* was 1.3 pptv. At an inlet temperature of 120 °C and with a CL of 26, the LOD for PNA was 3.4 pptv. When averaging for 90 s, the minimum of an Allan variance plot (Figure 7 of Paul and Osthoff)[65] the LOD improves to 8.7 pptv for NO_2 , 0.13 pptv for ΣPAN*, and 0.33 pptv for PNA.

The accuracy of TD-PERCA-CRDS is limited by uncertainties in CL (±7% for dry air), variability in the response to different type of peroxy radicals (±9%),[131] and of the NO_2 measurement (±4%) which is dominated by uncertainties in the absorption cross-section and R_L.[65] Adding these in quadrature gives a combined uncertainty of ±12% for dry air.

An additional uncertainty factor for the differential temperature TD-PERCA-CRDS is the uncertainty in F_T. The chambers are operated at temperatures where F_T is highly sensitive to temperature (Figure 4). Judging from the scatter observed (for example, in Table 5.4), An additional ±5% random error is expected to be introduced, raising the combined measurement uncertainty to ±13%. Not included in this estimate are systematic errors that might arise from the unknown and potentially variable TD profile of the interferences included in ΣPAN*.

5.3.9 Interference Tests

A series of qualitative tests using a semi-random collection of chemicals in the laboratory was conducted to evaluate the selectivity of the TD-PERCA-CRDS. At 110 °C, there was no response to the head space vapors above samples of hydrogen peroxide (H_2O_2), dinitrogen pentoxide (N_2O_5), acetone, water, or sodium hypochlorite solution.

Small negative signals were observed when sampling near surfaces such as human hand or from within an enclosed space, rationalized by dry deposition of O_3 and NO_2 to these surfaces.[201] Additionally, negative signals were observed when acetic acid, 4-heptanone, or iodine were sampled.

5.4 Discussion

The goals of this chapter were to (1) develop an ethane based TD-PERCA-CRDS, (2) determine the CL at elevated temperatures, and (3) to evaluate the feasibility of using ethane-based TD-PERCA to quantify ΣPN and ΣPAN in ambient air. The TD-PERCA-CRDS was calibrated and characterized. The TD-PERCA-CRDS owes its good sensitivity to its high CL, which increases with temperature. Attempts to rationalize the observations in light of the model simulations (Chapter 4) were limited because models simulating PERCA need to take wall loss rates into account and are generally poor predictors of experimental chain lengths. From a gas-phase kinetics perspective, reactions of HO_2 and RO_2 with NO (e.g., R5.3, Table 5.2) have a negative activation energy and are thus expected to slow down at higher temperatures, decreasing turnover rates and the CL. On the other hand, the RH dependence is reduced by heating, in part because one of the radical chain-terminating reaction, $HO_2+NO\rightarrow HNO_3$, proceeds via a water adduct ($HO_2\cdot H_2O$).[144-145] The temperatures within the PERCA reaction heater are sufficiently elevated to dissociate this intermediate, shutting down this radical sink reaction. In addition, the elevated temperatures inside the reactor may lessen reactions at the reactor inner wall surfaces (by driving off adsorbed water molecules, for example) though direct evidence for this happening is lacking.

However, several stumbling blocks were encountered that on aggregate indicate that the measurement of ΣPN and ΣPAN in ambient air would be difficult and error-prone in practice. On the one hand, the ethane-based TD-PERCA-CRDS has demonstrated great LODs (<1 pptv for ΣPAN* and PNA). This constitutes a considerable improvement compared to our previous generation TD-CRDS, whose LOD was in the 100s of pptv,[65] and represents the first optical absorption measurement of PNA at concentration levels of the same magnitude as found in

ambient air (Table 5.1). In addition, the measurement can tolerate a large NO_2 background through selective amplification of the desired signal: In Figure 5.12, for example, the NO_2 background was >30 ppbv, yet PNA and PAN were quantified with a 1 s, 1 σ precision of <6 pptv and <40 pptv, respectively (Table 5.5). Moreover, the sensitivity of the ethane-based TD-PERCA is better than the room temperature measurement of RO_x radicals (1.6 pptv; 90 s, 2 σ),[131] mainly because of the greater amplification (~69 vs. ~25) and in spite of the CAPS sensor being slightly more sensitive to NO_2 than our CRDS. Furthermore, the instrument's sensitivity is comparable to (or better than) what is achievable with commonly used GC and CIMS methods. For example, at an inline temperature of 120 °C, the sensitivity of TD-PERCA-CRDS for PNA was of the same order of magnitude as our CIMS at its non-specific ion at *m/z* 62 and the optimized CIMS recently described by Chen et al.[162]

On the other hand, however, the TD-PERCA-CRDS method has several drawbacks, some of which still need to be overcome to make ambient measurements of ΣPN and ΣPAN a reality. The first challenge is posed by the TD profiles of PAN and PNA (Figure 5.4) which are not completely separated. This overlap is particularly problematic in ambient air because the signal generated by the typically much smaller PNA concentrations could be overshadowed by a much larger ΣPAN signal. In this work, the overlap of the TD profiles of PNA and PAN (and, the rather limited dynamic range of <500 pptv) was overcome by the differential temperature / linear combination method (section 5.3.7) in which ΣPAN was only partially dissociated and PNA close to completely dissociated.

A complication is that methyl and ethyl peroxy nitrate have TD profiles that are similar, but not identical, to that of PNA; these molecules dissociate at lower temperatures than PNA (Table 5.3).

This does not matter if the TD-PERCA inlets are operated at temperatures at which all three molecules are fully dissociated (or nearly so) as in this work.

The differential temperature approach has the additional advantage of avoiding the O_3 interference that occurs above 150 °C, which would otherwise have been a serious issue because of the typically much larger O_3 than PAN or PNA concentrations in ambient air, and gave consistent results in synthesized air mixtures and room air.

A second drawback of TD-PERCA is the RH dependent CL, which necessitates frequent calibrations to determine CL×F at each channel's temperature, though this could in principle be straightforward with photochemical sources of PNA and PAN and automated switching. At the same time, frequent calibrations of CL and F would relax the need to carefully match the responses in each of the TD channels, which is a requirement in conventional TD instruments.

A third and most substantial drawback are the interferences. The O_3 interference is easily avoided by switching the instrument from ethane to CO operation. With CO, any O generated from O_3 dissociation would react to form CO_2 and be of no further consequence. However, CO-PERCA is somewhat unappealing because of CO's high toxicity and lack of smell, making its use impractical and impermissible in some university laboratories due to legitimate safety concerns. Mihele and Hastie[118] used PAN as a radical source by heating a short section of the inlet of their CO-PERCA to 200 °C and found the CL to be the same as other radical sources (which included passing H_2 past a heated wire and a Cl_2 photolysis source), which suggests that the CL in a CO based PERCA is less dependent on temperature than with an ethane based PERCA, which would be another advantage of CO based PERCA.

The unknown interference observed in laboratory air is by far the biggest hurdle. The identity of the molecule or class of molecules interfering, and if the interference is present in ambient air,

away from anthropogenic sources, or found only within a chemistry laboratory remains unclear. Some interferences were conducted (Chapter 6, section 6.3.6) but were inconclusive. More work is needed to identify which molecules or class of molecules interferes in TD-PERCA-CRDS and are included in ΣPAN*. It is possible that the interfering species thermally dissociate(s) to release O atoms; if that's the case, this interference would not be present in a CO based TD-PERCA. Hence, measurements using a CO-based TD-PERCA should be attempted.

5.5 Conclusion

A TD-PERCA-CRDS instrument was constructed, characterized and calibrated. The TD-PERCA-CRDS has an amplification factor of up to 69±5 at 250 °C, which provides for a LOD (1 s, 1 σ) of 1.3 pptv. For the measurement of ΣPAN and PNA in ambient air a differential temperature TD-PERCA-CRDS setup was developed and evaluated. The setup was capable of simultaneously measuring both ΣPAN and PNA on top of a large background of NO_2. In ambient air, however, the instrument suffers from an unidentified interference. Identifying this interference and assessing whether or not this interference is present in TD-PERCA-CRDS instruments employing CO as a chain carrier would be a logical next step.

Chapter Six: Detecting TATP with TD-PERCA-CRDS

Parts of this chapter have been accepted for publication by *Analytical and Bioanalytical Chemistry*, doi: 10.1007/s00216-018-1072-0.[202]

This chapter focuses on the detection of the peroxide explosive TATP by TD-PERCA-CRDS. A sample of TATP was synthesized and characterized with FTIR.

6.1 Introduction

TATP, is the most commonly encountered peroxide explosive, and is increasingly being used in terrorist attacks.[15] The lack of metallic elements or easy to identify functionality (e.g. NO_2) has made the detection of peroxide explosives challenging.[2, 12] Recent advances in explosive detection technology have made great strides, yet, the rapid and efficient detection of TATP, and other peroxide explosives, without the need for sample pre-concentration or swabbing has yet to be realized.[23-24] The thermal decomposition of TATP is believed to proceed via a series of radical intermediates[12] which may be exploited in a detection scheme. Here, the detection of TATP, via the radical intermediates of its thermal decomposition, will be attempted by TD-PERCA-CRDS.

6.2 Materials and methods

6.2.1 Preparation of explosive samples

Because TATP is an explosive material that is shock- and heat-sensitive, care was used in its preparation. TATP was synthesized by amalgamating several literature procedures.[12, 14] Briefly, hydrogen peroxide solution (50%), acetone (HPLC grade), and sulfuric acid (99.999%) were purchased from Sigma-Aldrich (Oakville, ON) and were used as received. All reagents and glassware were pre-cooled using an external ice-water bath. 0.5 mL acetone, 0.5 mL H_2O_2 and a

drop of sulfuric acid were added to a 50 mL round bottom flask and allowed to warm up to room temperature. After 24 hours, a white solid had formed which was dissolved in 10 mL pentane, washed with 10 mL water in a 125-mL separatory funnel, dried by filtering through anhydrous $MgSO_4$ (Sigma-Aldrich), and allowed to evaporate to dryness in a 3-valve glass vessel (similar to the one shown in Figure 5.2), forming, a clear, colorless, and cubic crystal.

Analysis of the head space vapor by FTIR (see below) revealed the presence of an impurity, which was removed by subsequent recrystallization from methanol.[203] Some experiments were replicated with a commercial TATP sample (Accustandard, New Haven, CT) shipped as a 100 μg mL^{-1} solution in acetonitrile (ACN) contained in a sealed 1 mL ampule. This sample was transferred to a clean 3-valve glass vessel for sample delivery. Results (not shown) with the commercial sample were identical to those obtained with the material synthesized in house.

6.2.2 Fourier Transform Infrared Spectroscopy

The mid-infrared spectrum of TATP vapor was recorded on a Bruker Tensor 27 FTIR equipped with a multi-pass cell (Gemini Spectral Sciences, Garfield, NJ, Venus Series) with 6.4 m optical path length. The resolution of the spectrometer was 0.5 cm^{-1}. Background spectra were acquired by flushing the multipass-cell with ultrapure, "zero" grade air (ZA; Praxair). The absorption cell was then filled with TATP vapor by flushing the head space above the TATP crystal with ~5 sccm of ZA through the cell. 16 sample and 16 background scans were averaged.

6.2.3 Generation of gas streams containing TATP

The explosive sample was placed in a 3-valve glass vessel, whose head space was purged with O_2, whose flow rate was controlled at 15 sccm using a 100 sccm MFC. This flow was sent through

the FTIR multipass cell and combined with a flow of ZA that was slightly greater than the sampling flow rate of the TD-PERCA-CRDS (~3 slpm).

In addition, ambient air experiments were conducted in which the glass vessel containing the TATP sample was placed next to the TD-PERCA-CRDS inlet with the opening of the glass vessel at a distance no greater than ~ 5 cm. The glass vessel was opened to ambient air and the contained vapor allowed to diffuse into the room for ~ 2 minutes as the TD-PERCA-CRDS sampled the air nearby. To reduce air currents generated by the lab's overhead ventilation system, the glass vessel was placed beneath a desk covered on all sides with a linen cloth. In addition to the TATP samples, blanks consisting of cleaned (empty) glass vessels were sampled.

6.3 Results

6.3.1 Mid-infrared spectrum of TATP vapor

The gas-phase FTIR spectrum of TATP is shown in Figure 6.1. The observed frequencies and intensities are summarized below (Table 6.1). Prior to recrystallization, the spectrum contained a strong peak at 3442.5 cm^{-1} (Figure 6.1, gray trace). Recrystallization of TATP from methanol following the procedure by Oxley et al.[203] removed this peak and several shoulders from the other transitions (plus many water and CO_2 lines present initially as impurities).

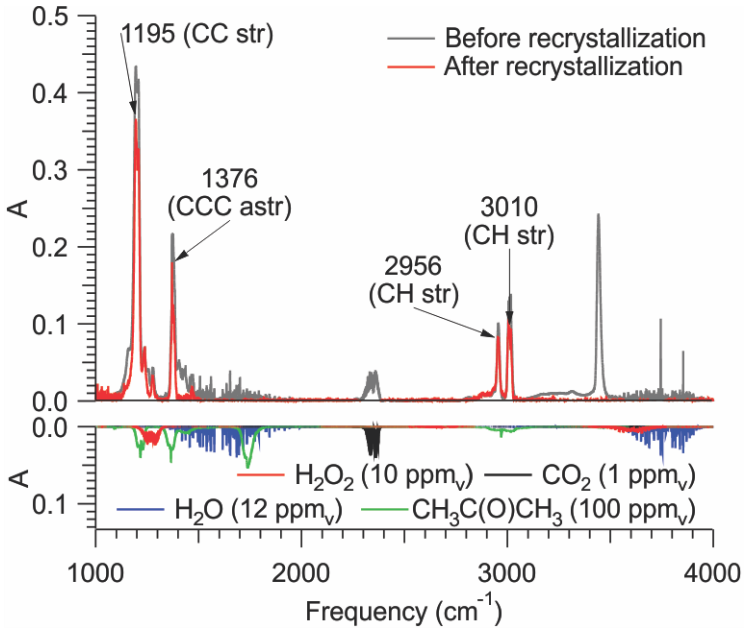

Figure 6.1 (Top) FTIR absorption spectra of TATP vapor before (gray color) and after recrystallization (red color). The strongest TATP transitions are labeled with the main atoms involved in and the type of vibrational motion (str = stretching motion, astr = asymmetric stretching motion). (Bottom) Reference spectra[63] of water (blue color), carbon dioxide (black color), hydrogen peroxide (red color) and acetone (green color) scaled to the mixing ratios indicated in the legend

Table 6.1 Infrared transitions of TATP. n/o = not observed

Frequency observed (cm^{-1})	Intensity (absorbance units)	DATP – Literature[20] [4] gas phase values (cm^{-1})	TATP - Literature[20] [5] gas phase values (cm^{-1})	TATP - average solid state (cm^{-1})[206]	Assignment[206]	Absorption cross-section* (10^{-20} cm^2 $molecule^{-1}$)
1146	0.018	1151.6	-	1129	CCO b, CO str	1.8
1195.3	0.366		1193.8	1186	CC str, CCO b	37
		1205.5				
1208.8	0.327		-	1202	CCC b, OCO b	33
1238.7	0.069		-	1234,1246	CC str, CCO b OCO b, CO str	7
		1270.9				
1277.9	0.033		-	1275	CCO b, CO str	3
1366.5	0.076		-	1369	CCC asym str	8
1370.8	0.178		-	1369	CCO b	18
1376.5	0.125		-			13
1380.6	0.109	1380.3	-	1386	CCC sym str	11
1384.5	0.078		-			8
		1431.3				
1443.4	0.009		1441.2	1434 1448	CH_2 b CH_2 b	0.9
1468.7	0.019	1469.8	-	1460	CH_2 b	1.9
n/o	-		-	2718	overtone/combination	
2877.1	0.011		-	2867	CH str	1.1
2955.3	0.082	2954.1	2944.7	2948	CH str	8
3002.4 3005.7 3010.4 3013.1 3017.5	0.082 0.114 0.093 0.080 0.093	3006.5	3010	2997 3004 3004	CH str CH str CH str	8 11 9 8 9
		3033.4				

* Lower limit as it is assumed that saturation vapor pressure was achieved; uncertainty of ±44%.

Even though there are 93 vibrational modes in TATP plus combination and overtone transitions, the mid-IR spectrum of TATP is relatively simple as many transitions overlap and are not resolved. There is agreement between the spectrum in Figure 6.1 and the (literature average) transitions given by Brauer et al.[206] (Table 6.1) in that all expected transitions were present. Furthermore, transitions belonging to starting materials (i.e., of acetone and hydrogen peroxide) were not observed.

Assuming that TATP achieved saturation vapor pressure of $(6.3\pm2.8)\times10^{-5}$ atm at 25 °C,[28] the spectrum after recrystallization shown in Figure 6.1 allows an estimation of the (upper limits of the) TATP absorption cross-sections. For the major peak in the spectrum at 1195 cm^{-1}, for example, the absorption cross section is $(3.7\pm1.6)\times10^{-19}$ cm^2 $molecule^{-1}$. Cross-sections for the other peaks are summarized in Table 6.1.

6.3.2 TD-PERCA-CRDS measurements of background air and air spiked with TATP

A time series showing the response of TD-PERCA-CRDS, with its inlet heated to 250 °C, to reagent gases, background air, and TATP is presented in Figure 6.2. In this example, the zero-concentration level was established beforehand by sampling ZA (not shown).

At 20:38, ~655 ppbv of NO were added to the sampled air, producing a small offset (~3.3 ppbv in this example). At 20:39, the ZA flow was stopped and the instrument sampled room air.

Indoor air contains PAN and O_3 at concentrations that are smaller than found in outside air but can nevertheless be non-negligible.[201, 207] The NO added to the inlet will react with O_3:

$$NO + O_3 \rightarrow O_2 + NO_2 \qquad \text{R6.1}$$

At 250 °C, the PANs are fully dissociated, generating four equivalents of NO_2.[65] In the example shown in Figure 6.2, a total of ~20.6 ppbv of NO was oxidized to NO_2 by these pathways.

At 20:41, ~1.5% ethane was added to the inlet, initiating PERCA and raising the NO_2 level to ~275 ppbv. Most of this signal is due to chemical amplification of PA radicals generated from TD of PAN. In addition, this signal is due to the partial dissociation of O_3 to O as discussed in chapter 5.3.6.

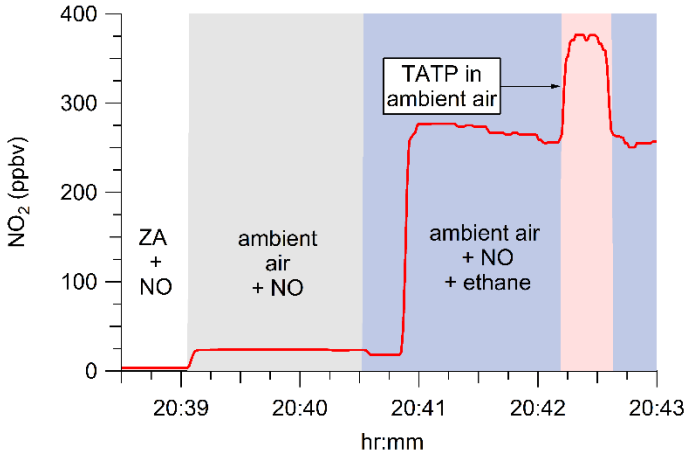

Figure 6.2 Time series showing the response of TD-PERCA-CRDS, with its inlet heated to 250 °C, to zero air plus 655±3 ppbv NO (white background), ambient air plus NO (gray background), NO and (1.5±0.1)% ethane plus ambient air (blue background), and with additional TATP vapor (red background)

At 20:42 (Figure 6.2), a TATP sample was placed in front of the inlet, and a sharp increase in signal, ~115 ppbv above the background level, was observed.

6.3.3 Optimization of TD-PERCA-CRDS response to TATP vapor

Figure 6.3 summarizes the TD-PERCA-CRDS response to TATP in ZA as a function of inlet temperature. In the absence of TATP and presence of NO and ethane, there was no response by TD-PERCA-CRDS regardless of sampling temperature (Figure 6.3, black circles). Likewise, there

was no response to TATP in the absence of PERCA gases (i.e., NO, or NO and ethane) over this temperature range (data not shown).

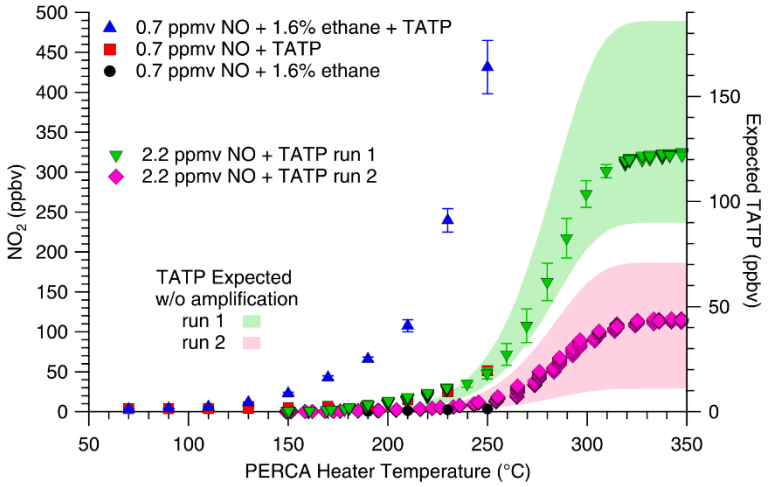

Figure 6.3 Mixing ratios of NO_2 observed by TD-PERCA-CRDS during headspace analysis of a TATP sample as a function of inlet temperature. Black circles: reagent gases only. Red squares, green inverted triangles, and purple diamonds: TATP plus NO. Blue triangles: NO plus ethane. The error bars represent the standard deviation (±1 σ) of consecutive measurements at a given temperature. Superimposed on the right-hand axis (shaded areas) are the TATP mixing ratios expected for two trial runs with TATP at mixing ratios calculated from TATP's saturation vapor pressure multiplied by its expected extent of dissociation and flow dilution factor (see text). The shaded regions represent the uncertainty (±1 σ) associated with the vapor pressure of TATP

When sampling the TATP headspace in the presence of 0.7 ppmv NO (Figure 6.3, red squares), a temperature dependent signal that increased up to 51±5 ppbv at 250 °C was observed. The same dissociation profile (Figure 6.3, magenta diamonds and green triangles) was observed independent of TATP concentration. Upon addition of ethane, this signal was amplified further, up to 431±33 ppbv of NO_2 at 250 °C (Figure 6.3, blue triangles).

Shown on the right-hand axis of Figure 6.3 is the amount of TATP expected to decompose, which was calculated as follows: Assuming saturation vapor pressure $(6.3\pm2.8)\times10^{-5}$ atm at

25 °C[28] within the 3-neck flask, and applying a dilution factor the TATP mixing ratio reaching the inlet heater was calculated. For example, during run 1 (Figure 6.3) the dilution factor was $(1.9\pm0.4)\times10^{-3}$ (TATP sample flow/ total instrument flow = (5±1) sccm / (2602±100) sccm) and the TATP mixing ratio reaching the inlet was determined to be 138±48 ppbv. For run 2, the dilution factor was $(6\pm4)\times10^{-4}$, giving a TATP mixing ratio of 41±30 ppbv. Of these amounts, only a fraction (depending on inlet temperature) decomposes at temperatures < ~325 °C, as explained below.

The thermal decomposition of TATP follows first-order kinetics.[14] The amount that thermally decomposes in the heated inlet, $[TATP]_{dec}$, was estimated using:[55]

$$[TATP]_{dec} = (1 - e^{-kt})\,[TATP]_0 \qquad (6.1)$$

Here, $[TATP]_0$ is the amount of TATP present initially, and t is the residence of TATP in the inlet. The rate coefficient for thermal decomposition, k, is calculated using the Arrhenius equation ($A\times e^{(-Ea/(RT)}$) where R is the universal gas constant (8.314 J mol^{-1} K^{-1}), and A and E_a are equal to 3.75×10^{13} s^{-1} and 151 kJ mol^{-1}, respectively.[14]

The residence time in the converter, t, was calculated using the inner dimensions of the quartz heater and the flow rate and was ~0.24 s. The thermal dissociation profiles were calculated by multiplying equation (1), the equilibrium vapor pressure of TATP, and the flow dilution factor for the conditions of runs 1 and 2 and are shown as underlays in Figure 6.3.

In the presence of NO, the shape of the experimental TD profiles matched those of the expected profiles. The relative concentrations, however, require an NO-only amplification factor of 2.6±0.5. This amplification factor was constant for NO mixing ratio > ~700 ppbv (Figure 6.4).

Sampling TATP in the presence of both PERCA gases, i.e., NO and ethane, results in up to 431±33 ppbv (Figure 6.3, blue triangles) of NO_2 at 250 °C. Higher temperatures were not investigated as the amount of NO_2 that could be generated would have been limited by the amount of NO. This much larger response in the presence of ethane shows that TD of TATP produces radicals that are chemically amplified to produce a large analytical signal.

Unlike the NO-only amplification, the amplification factor in the presence of ethane and NO is non-linear and scales roughly inversely with radical concentration, mainly due to radical – radical self-reactions at these large concentrations.[131] Nevertheless, an amplification factor of 22±3 (temperature range 190 – 250 °C) was achieved, corresponding to additional amplification by a factor of ~9 per TATP decomposed.

6.3.4 Dependence of TATP signal on NO mixing ratio

The concentration dependence on NO mixing ratio was verified by sampling a constant mixing ratio of TATP with the TD-PERCA-CRDS operated in NO-only mode at an inlet temperature of 325 °C. The experiment was conducted twice, at TATP mixing ratios of ~1 and ~6 ppbv; these mixing ratios were calculated assuming saturation vapor pressure and flow dilution as described in section 6.3.3. For clarity, the observed NO_2 mixing ratios were normalized (i.e., divided by their respective maximum values) before presentation.

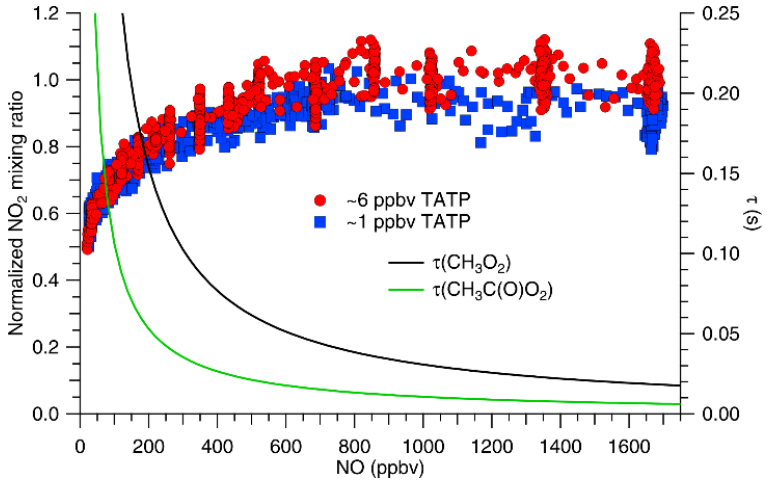

Figure 6.4 Dependence of observed normalized TATP signal on NO mixing ratios with TD-PERCA-CRDS operated in NO-only mode

The results (Figure 6.4) show that above ~700 ppbv of NO the amount of NO_2 generated is independent of NO mixing ratio. Shown on the right hand-side of Figure 6.4 are pseudo-first lifetimes of CH_3O_2 and $CH_3C(O)O_2$ with respect to reaction with NO (the rate coefficients are listed in Table 5.2). At the lower NO mixing ratios in Figure 6.4, the lifetimes of these peroxy radicals approaches the residence time of the gases in the PERCA inlet (~0.24 s), preventing the reaction from going to completion prior to measurement of NO_2.

6.3.5 Figures of Merit

When sampling ZA in the presence of ~2 ppm NO, the CRDS has a minimum detectable NO_2 mixing ratio (calculated using equation 6 of [66]) of ~56 pptv for data averaged over 1 s. At ~325 °C in NO-only mode, the TATP detection limit is then ~22 pptv, more than six orders of magnitude below this compound's saturation vapor pressure. In the presence of ethane and NO at 250 °C, the minimum detectable NO_2 mixing ratio was ~100 pptv for 1 s data, corresponding to ~5 pptv of TATP.

6.3.6 Interference tests

A positive signal was observed when skin moisturizer cream or anti-perspirant was held up to the inlet; the signal intensity was several orders of magnitude less than observed for TATP (not shown). Ingredients possibly causing this interference are discussed below.

6.4 Discussion

6.4.1 Mid-infrared spectrum of TATP vapor

The mid-IR spectrum of TATP vapor reported here fills an important void in the current literature as there are few IR spectra of TATP reported, and most of those reported are in the solid state (and not of TATP vapor) or the description of the spectra was not comprehensive (e.g., no cross-sections, tables of transitions etc.). Knowledge of the TATP gas phase spectrum is needed to enable its detection by IR sensors.

Brauer and coworkers[206] provided a comprehensive summary of TATP infrared transitions. They assigned the mid-IR spectrum of TATP on the basis of available solution and solid-state spectra and their own theoretical predictions. Many of the transitions observed in this work are blue-shifted by a few cm^{-1} relative to those reported by Brauer et al.,[206] likely because of a lack of intermolecular interactions (such as hydrogen bond bridges)[12] that occur in the solid or liquid phase but not in the gas phase.

Our observations are consistent with other gas phase spectra reported in the literature such as the Raman transitions reported by Pacheco-Londono et al.[205] and the spectrum shown by Hildenbrand et al.,[94] who unfortunately did not tabulate the IR frequencies they observed.

Recently, Guo and coworkers reported the gas-phase IR spectrum of diacetone diperoxide (DADP);[204] several peaks that they reported for DADP were not present in Figure 6.1, indicating

the absence of DADP in this work. Overall, the IR spectrum confirms that the head space above the synthesized TATP sample contained TATP in high purity.

The transitions of impurities prior to recrystallization are documented as such transitions may be utilized for forensic "fingerprinting". The impurity peak at 3442.5 cm^{-1} observed originally (Figure 6.1, gray trace) likely originated from an intermediate formed during TATP synthesis that co-precipitated. One potential candidate is $(CH_3)_2C(OH)$-OO-$C(CH_3)_2OOH$, a molecule which was observed by Pacheco-Londono and coworkers during TATP synthesis.[205]

6.4.2 Implications on the mechanism of TATP decomposition

The results presented here shows that CH_3 is formed during the thermal decomposition of TATP. A proposed mechanism is shown in Figure 6.5. The main decomposition pathway for TATP follows a non-redox mechanism and involves several acetone elimination steps to yield O_3 (Figure 6.5, top row).[12, 14, 208] Upon formation of a first equivalent of acetone an alkoxy peroxyl diradical intermediate species (I) is formed. This diradical is believed to proceed to form a 7-membered ring (II) before further thermal decomposition yields a second equivalent of acetone and an alkoxy trioxyl diradical (III). (III) then forms a third equivalent of acetone and releases an O_3 molecule.

When sampling TATP in NO-only mode (e.g., Figure 6.3, run 1 and run 2), an NO_2 signal a factor of 2.6±0.5 larger than that expected from TATP saturation vapor pressure and flow dilution was observed. This amplification factor is a lower limit since TATP may not have achieved saturation vapor pressure in the glass vessel. The amplification indicates that the thermal dissociation does not exclusively proceed via pathway 1 as this pathway only generates 1 equivalent O_3 which reacts with NO to NO_2. A plausible explanation is that radical intermediate (I) is sufficiently long-lived to react with NO rather than eliminating acetone.

Upon reaction of the alkoxy peroxyl diradical (I) with NO, the dialkoxy diradical (IV) is formed. (IV) is the ring opening product of DADP and may proceed via a C-O cleavage to stepwise eliminate two acetone molecules leaving an O_2 molecule. This pathway provides for 1 equivalent of NO_2.

Alternatively, (IV) may proceed via C-C cleavage to produce a methyl radical and intermediate (V). (V) may then decompose via a C-C cleavage to form two more methyl radicals. In NO-only mode, the methyl radical proceeds via reactions R1, R3, R5 and R2 to produce two equivalents of NO_2; thus, this pathway yields 9 equivalents of NO_2.

Alternatively, (V) could potentially eliminate acetone to form the PA radical which converts NO molecules to NO_2. On aggregate, this pathway yields 6 NO_2 molecules per molecule of TATP. Since no single pathway rationalizes the yield of 2.6 radicals per TATP, the thermal decomposition of TATP in the presence of NO likely involves a combination of the above pathways.

Sampling TATP in the presence of NO and C_2H_6 resulted in signals amplified to such a degree that a large fraction of the ~0.7 ppmv of NO reagent were depleted (Figure 6.3, blue triangles). This large amplification upon addition of ethane corroborates the notion that peroxy radicals are generated during the decomposition of TATP and is consistent with the conclusions of the NO-only experiments.

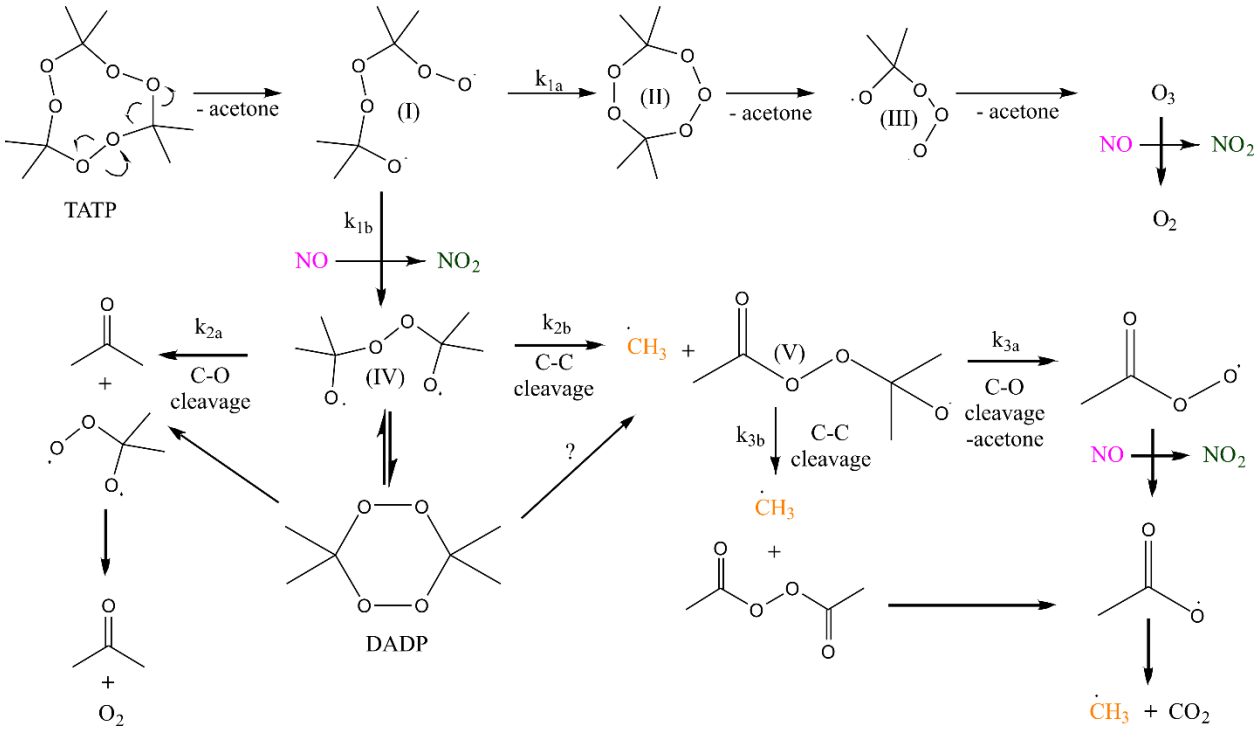

Figure 6.5 Proposed mechanism for TATP decomposition in the presence of NO

6.4.3 TD-PERCA-CRDS as a TATP detection method

The TD-PERCA-CRDS method developed enables highly sensitive (~5 pptv), rapid (1 Hz), continuous, and robust detection of TATP in ambient air. The figures of merit top most TATP detection methods reported in the recent literature (Table 6.3), all while deploying the easiest possible sample introduction method, direct gas analysis. The highest sensitivity (5 pptv; 0.5 pg equivalent) was achieved when the TD-PERCA-CRDS was operated with both ethane and NO. Though less sensitive by an order of magnitude, the NO only mode would be more attractive for routine screening applications as it requires fewer reagent gases and produces easier to handle exhaust, though it would be straightforward to switch in ethane for boosted sensitivity if desired. The ultrahigh sensitivity of TD-PERCA-CRDS is a considerable advantage as it would help in

overcoming deliberate concealment of TATP (e.g., in a sealed plastic bag), which reduces the observed mixing ratios of an explosive by a factor of ~1,000.[17]

The TD-PERCA-CRDS is expected to be robust as it builds on the now 30-yr old CRDS technique, which has matured to a point that turn-key instruments have become commercially available from multiple manufacturers. Even though multiple detection channels are used in this work, a single CRDS channel would suffice for TD-PERCA-CRDS and enable a more compact instrument design.

One disadvantage of TD-PERCA-CRDS is the background arising from presence of O_3 and PAN in ambient air, which is considerably larger when operated in ethane-PERCA mode. While this background will drift over the course of a day (as indoor air is exchanged with outdoor air and O_3 is produced photochemically), it is not expected to change suddenly, certainly not on a time scale of a few seconds needed for screening. TATP (when present) generates a large signal (e.g., Figure 6.2) that is easily distinguishable from the slowly varying background. Furthermore, many buildings (e.g., hospitals) use scrubbers that condition intake air and remove much of the PAN and O_3, hence reducing the atmospheric background signal.

Table 6.2. A comparison of selected TATP vapor detection methods. More methods are given by [209] and references therein

Detection Method	Sampling Method	LOD	Sampling and analysis time	Reference
IR laser spectroscopy	Collected onto hollow fibers prior to delivery into detection cell	430 ppbv	5 min	[94]
Hybrid organic semiconductor sensor	Direct gas analysis	100 ppbv	30 s	[210]
Chemiluminescence	Swabbing and digestion prior to analysis	40 ppbv	5-10 min	[96]
IR photoacoustic spectroscopy	Direct gas analysis	18 ppbv	30 min	[89]
Proton transfer reaction mass spectrometry	Direct gas analysis	15 ppbv	1 s	[211]
Metal oxide semiconductor sensor	Direct gas analysis	12 ppbv	30 minutes	[101]
Selected ion flow tube mass spectrometry	Direct gas analysis	10 ppbv	1 s	[212]
Colorimetric sensor array	acid catalyzed gas analysis followed by assay	2 ppbv	5 min	[99]
Ion mobility spectrometry (IMS)	Gas collected using planar solid-phase micro extraction (SPME)	10 mg	35 s	[30]
IMS	Swabbing prior to vapor desorption	2-4 μg	4 – 10 s	[213]
Electrospray ionization MS	Liquid sample injection	62.5 ng	60 s	[214]
GC-IMS	Swabbing prior to vapour desorption	10 ng	220 s	[42]
Solid-phase micro-extraction (SPME) – GC – MS	Gas collected using SPME	5 ng	10+10 min	[215]
Desorption electrospray ionization mass spectrometry (DESI-MS)	Pneumatically-assisted electrospray from a surface	1 ng	5 s	[216]
GC-TOF-MS	Solution	50 pg	20 min	[217]
TD-PERCA-CRDS (NO only mode)	Direct gas analysis	22 pptv (2 pg)	1 s	This work
TD-PERCA-CRDS (ethane PERCA)	Direct gas analysis	5 pptv (0.5 pg)	1 s	This work

A major disadvantage is the response to anti-perspirant and skin cream/moisturizer products. These products contain numerous compounds, including cyclopentasiloxane (D5). Cyclic siloxanes are slightly volatile and thermally decompose to release methyl radicals,[218] though the Arrhenius parameters for decomposition[219] are such that this molecule is not expected at inlet temperatures used in this work. However, recent studies[220] suggest that pyrolysis of polysiloxanes may occur at temperatures as low as 70 °C. TD of polysiloxanes generates dimethylsilonane ($(CH_3)_2SiO$, D1) as an intermediate, whose further decomposition generates two CH_3 radicals[218] and, in the presence of excess NO, four equivalents of NO_2. Organosiloxanes have become ubiquitous in the environment and are commonly used.[221] This compromises the utility of TD-PERCA-CRDS at security checkpoints as it makes it prone to false positives, though TD-PERCA-CRDS may nevertheless be useful as a first screening tool.

On the other hand, it is likely (and an advantage) that this instrument would respond to peroxide explosives other than TATP: For instance, DADP likely decomposes via a radical mechanism[14] similar to that of TATP and hence is expected to be detectable by the TD-PERCA-CRDS. Furthermore, the instrument would respond to the vapors of certain NO_2-containing explosives (e.g., PETN) though only if these were present in very high concentration.

6.5 Conclusion

The detection of TATP was demonstrated using TD-PERCA-CRDS. Radicals generated during the thermal decomposition of TATP were reacted with NO and measured indirectly as NO_2. In NO only mode, the TD-PERCA-CRDS LOD with respect to TATP was found to be 22 pptv. In ethane PERCA mode the TD-PERCA-CRDS LOD with respect to TATP was 5 pptv. Despite ambient air interferences, TD-PERCA-CRDS provides a sensitive and robust TATP detection method.

Chapter Seven: Thesis summary, conclusions, and future work

My research has focused on the development of indirect explosive detection methods capable of detecting explosive vapours in ambient air. My work was motivated by the need to develop improved explosive detection instrumentation. Current explosive detection technologies often fail to provide real-time detection of explosives or require inefficient and invasive grab samples or swabs to be obtained. To overcome this limitation, several real-time explosive sensors based on the indirect detection of explosive vapours in the gas phase were developed and are described in this thesis. Nitroaromatic explosives were thermally converted, with the aid of a Pt catalyst (chapters 2), to NO_2, which is the common molecule detected via blue diode CRDS. The use of pre-concentration to lower detection limits was explored in chapter 3. Similarly, the peroxide explosive TATP was thermally decomposed, and its radical decomposition products converted to NO_2 (chapter 6) via a radical amplification scheme (Chapters 4-6).

Chapters two and three of the thesis focused on the measurement of nitroaromatic explosive vapours. An explosives sensor based upon the catalytic thermal dissociation of nitroaromatic explosives to NO_2 and subsequent detection using blue diode laser CRDS has been described (chapter 2). A two-channel prototype, dubbed cTD-CRDS, was constructed. One channel contained PtO_2 heated to 350 °C to catalytically convert nitroaromatic explosives to NO_2, whereas the other was operated as a reference channel. Initial tests with FTIR and large mixing ratios (~250 ppbv of nitroaromatics) demonstrated the quantitative conversion of nitroaromatics to NO_2. Upon switching to the less volatile TNT, the conversion did not appear to be quantitative for reasons that are unclear. Nonetheless, the prototype had a limit of detection of 0.5 ppbv at 1 Hz data collection. Molecules other than nitroaromatics generated background signals in the heated

channels and still need to be fully explored and assessed. While cTD-CRDS was able to detect NB, DNB, DNT and TNT it lacked the sensitivity to detect the less volatile nitroaromatic explosives (such as PETN, Tetryl and RDX).

To improve the cTD-CRDS sensitivity, pre-concentration of nitroaromatics on Tenax prior to catalytic thermal dissociation was attempted (chapter 3). Ozone was added to the instrument between the catalytic converter and CRDS detection channels to convert any NO, that may form in the converter, back to NO_2. This led to improved conversion efficiencies. However, although pre-concentration was indeed possible, sample recoveries from the trap were very low (3.6±0.3 %). Sample recovery was likely low due to poor trapping of the nitroaromatics on Tenax or decomposition of nitroaromatics during the desorption phase. Furthermore, the mismatch in the flows of the trap and the cTD-CRDS instrument required large dilutions of the trap outflow prior to quantification in the CRDS cavities. Therefore, pre-concentration failed to provide significant gains in signal to noise whilst reducing the instruments time resolution from 1s to several minutes (dependent on pre-concentration time). Additionally, Tenax was found to degrade upon use with TNT further diminishing the utility of pre-concentration based cTD-CRDS for explosive measurement in the real world.

Attempts to preconcentrate PETN, Tetryl or RDX on Tenax revealed an unexplained interference. Moving forward, the identity of these interferences must be assessed, and the decomposition mechanisms taking place in the cTD-CRDS catalytic converter should be studied. Alternative trapping materials, less prone to decomposition (e.g. graphitized carbon blacks, carbon molecular sieves, etc.) and with greater affinity for nitroaromatics (i.e. nitroaromatic selective cavitand), should be explored in future testing. Furthermore, alternative trap designs that are more suitable for use with large flows should be explored.

Chapters four, five, and six focused on the development of a radical conversion scheme that would allow the indirect detection of peroxide explosives which thermally decompose to radicals. These radicals were amplified via a PERCA scheme that requires the addition of NO and a radical chain carrier. PERCA commonly employs CO as a radical chain, a major issue due to the hazard that CO would pose if employed as a component of an explosive detection instrument.

A modelling study was carried out considering other PERCA radical chain carriers (chapter 4). Alkanes, alkenes, alkynes, ethanol and dimethyl ether were explored as potential chain carriers. Ethanol was found to be the most effective radical chain carrier but would condense under optimum conditions. The alkenes also provided suitable chain lengths, but would suffer from substantial background due to ozonolysis. Dimethyl ether and ethane both produced adequate chain lengths in the simulations and were found to be viable alternatives to CO. As ethane was successfully used by Wood et al.,[131] prior to conclusion of the modelling study it was the focus of the remaining modelling and experimental work. In the future, as dimethyl ether was also found as a viable alternative to CO the temperature dependence of its radical chemistry should also be assessed.

As detection of peroxy explosives by PERCA requires heat, the effect of temperature on radical chain length for an ethane based TD-PERCA reactor was examined. The modelling study (chapter 4 section 4.2.2) suggested that increased temperature in the PERCA reactor slows the radical chemistry and reduces the radical chain length. On the other hand, increased temperatures reduced the dependence of CL on relative humidity and removed several radical sinks such alkyl peroxy nitrate formation. The modelling suggested that TD-PERCA would be feasible, though with reduced chain lengths.

The largest unknown factor during modelling was the temperature dependence of radical wall loss reactions. Moving forward, the temperature dependence of wall losses must be investigated experimentally and temperature dependent wall loss terms incorporated into future modelling. This is paramount for modelling results to accurately reproduce experimental results.

An ethane based TD-PERCA-CRDS instrument was constructed and characterized (chapter 5). The instrument was ultimately calibrated with PAN, PPN and PNA and the CL characterized with respect to relative humidity and dynamic range. The instrument has a CL of 69±5 at 250 °C, and has reduced sensitivity towards humidity compared to conventional room temperature PERCA systems. This provided for an LOD (1 s, 1 σ) of 1.3 pptv at 250 °C. As the instrument was calibrated with PANs and PNA the feasibility of employing the instrument for atmospheric measurements of these species was explored.

Ozone decomposition at temperatures greater than 150 °C was discovered as a major interference. TD of O_3 produces atomic oxygen which abstracted a hydrogen from ethane in the PERCA reactor and produces HO and $C_2H_5O_2$ radicals. To avoid this interference and to quantify both ΣPAN and PNA, whose thermal dissociation profiles overlap, a multiple channel differential temperature PERCA prototype was constructed. By setting two channels to two distinct temperatures below 150 °C and measuring alongside a cold reference channel both ΣPAN and PNA mixing ratios could be retrieved. This worked well for lab generated samples. Measurement of laboratory air led to the discovery of an additional unknown interference. The molecule or molecules responsible thermally dissociate to HO, RO_2 or O at low temperature (<100 °C). If only O is generated the interference would not be present in a CO based TD-PERCA setup. Nonetheless, identifying this interference would be the next logical step.

With the CL of the TD-PERCA-CRDS setup calibrated at 250 °C, the measurement of TATP was attempted (chapter 6). TATP was synthesized in the lab and its identity and purity established using FTIR. The TATP sample was then analyzed using TD-PERCA-CRDS. Radicals generated during thermal decomposition of TATP were reacted with NO and measured indirectly as NO_2. TATP decomposition, in NO only mode, resulted in an NO_2 signal that was a factor of 2.6±0.5 larger than that expected from TATP saturation vapour pressure. In NO only mode, The LOD of TD-PERCA-CRDS with respect to TATP was 22 pptv. In ethane PERCA mode, TATP decomposition resulted in a NO_2 signal that was a factor of 22±3 larger than that expected from TATP saturation vapour pressure, and the LOD was 5 pptv. In both cases, the TD-PERCA-CRDS LOD was many orders of magnitude lower than TATP's saturation vapour pressure.

Interference tests of the ethane TD-PERCA-CRDS showed that the instrument responded to the headspace above anti-perspirants and skin cream/moisturizer products. It is unclear why this interference exists but is likely a result of radicals produced during the thermal decomposition of one of the numerous compounds that make up these products (e.g. cyclopentasiloxane (D5)). Identifying the compound(s) behind the interference is required prior to proceeding with further testing. However, despite ambient air interferences, TD-PERCA-CRDS provides a sensitive and robust TATP detection method.

References

1. Akhavan, J., *The Chemistry of Explosives*. 3rd edition ed.; The Royal Society of Chemistry: Cambridge, 2011.
2. Marshall, M.; Oxley, J., *Aspects of Explosives Detection*. Elsevier: 2008; p 302.
3. Le Chatelier, H., The development and propagation of the explosive shock waves. *C. R. Hebd. Seances Acad. Sci.* **1900,** *130*, 1755-1758.
4. Meyer, R.; Köhler, J.; Homburg, A., *Explosives*. Seventh, 7th; ed.; Wiley-VCH Verlag GmbH & Company KGaA: Weinheim, Germany, 2015.
5. Kistiakowsky, G. B.; Wilson, E. B., *The Hydrodynamic Theory of Detonation and Shock Waves*. Office of the Publication Board, Department of Commerce: 1941; p 100.
6. Kamlet, M. J.; Jacobs, S. J., Chemistry of Detonations .I. A Simple Method for Calculating Detonation Properties of C-H-N-O Explosives. *J. Chem. Phys.* **1968,** *48* (1), 23-&.
7. Mohan, V. K.; Hay, J. E., Reparamaterization of the Becker-Kistiakowsky-Wilson equation of state for water-gel explosives. *Combustion and Flame* **1983,** *50*, 207-218.
8. Politzer, P.; Murray, J. S., The Role of Product Composition in Determining Detonation Velocity and Detonation Pressure. *Cent. Eur. J. Energ. Mater.* **2014,** *11* (4), 459-474.
9. Lefferts, M. J.; Castell, M. R., Vapour sensing of explosive materials. *Analytical Methods* **2015,** *7* (21), 9005-9017.
10. Zawadzka-Małota, I., Testing of mining explosives with regard to the content of carbon oxides and nitrogen oxides in their detonation products. *Journal of Sustainable Mining* **2015,** *14* (4), 173-178.
11. Byrd, E. F. C.; Rice, B. M., Improved prediction of heats of formation of energetic materials using quantum mechanical calculations. *J. Phys. Chem. A* **2006,** *110* (3), 1005-1013.
12. Dubnikova, F.; Kosloff, R.; Almog, J.; Zeiri, Y.; Boese, R.; Itzhaky, H.; Alt, A.; Keinan, E., Decomposition of triacetone triperoxide is an entropic explosion. *Journal of the American Chemical Society* **2005,** *127* (4), 1146-1159.
13. Rice, B. M.; Pai, S. V.; Hare, J., Predicting heats of formation of energetic materials using quantum mechanical calculations. *Combustion and Flame* **1999,** *118* (3), 445-458.
14. Oxley, J. C.; Smith, J. L.; Chen, H., Decomposition of a multi-peroxidic compound: Triacetone triperoxide (TATP). *Propellants Explosives Pyrotechnics* **2002,** *27* (4), 209-216.
15. Jacoby, M., Explosives used in Brussels isn't hard to detect. *Chemistry and Engineering News* 2016, pp 17-18.
16. Explosives Act. Explosives Act. Revised Statutes of Canada, c. E-15, s. 1: 1985.
17. Kolla, P., The application of analytical methods to the detection of hidden explosives and explosive devices. *Angewandte Chemie-International Edition in English* **1997,** *36* (8), 800-811.
18. Ewing, R. G.; Atkinson, D. A.; Eiceman, G. A.; Ewing, G. J., A critical review of ion mobility spectrometry for the detection of explosives and explosive related compounds. *Talanta* **2001,** *54* (3), 515-529.
19. Moore, D. S., Instrumentation for trace detection of high explosives. *Review of Scientific Instruments* **2004,** *75* (8), 2499-2512.
20. Germain, M. E.; Knapp, M. J., Optical explosives detection: from color changes to fluorescence turn-on. *Chemical Society Reviews* **2009,** *38* (9), 2543-2555.
21. Lehnert, A. L.; Kearfott, K. J., The detection of explosive materials: Review of considerations and methods. *Nucl. Technol.* **2010,** *172* (3), 325-334.

22. Kemp, M. C. In *A Review of Sensor Data Fusion for Explosives and Weapons Detection*, Conference on Chemical, Biological, Radiological, Nuclear, and Explosives (CBRNE) Sensing XIV, Baltimore, MD, Apr 30-May 03; Baltimore, MD, 2013.
23. Brown, K. E.; Greenfield, M. T.; McGrane, S. D.; Moore, D. S., Advances in explosives analysis-part I: animal, chemical, ion, and mechanical methods. *Analytical and Bioanalytical Chemistry* **2016,** *408* (1), 35-47.
24. Brown, K. E.; Greenfield, M. T.; McGrane, S. D.; Moore, D. S., Advances in explosives analysis-part II: photon and neutron methods. *Analytical and Bioanalytical Chemistry* **2016,** *408* (1), 49-65.
25. Kangas, M. J.; Burks, R. M.; Atwater, J.; Lukowicz, R. M.; Williams, P.; Holmes, A. E., Colorimetric Sensor Arrays for the Detection and Identification of Chemical Weapons and Explosives. *Crit. Rev. Anal. Chem.* **2017,** *47* (2), 138-153.
26. Gares, K. L.; Hufziger, K. T.; Bykov, S. V.; Asher, S. A., Review of explosive detection methodologies and the emergence of standoff deep UV resonance Raman. *J. Raman Spectrosc.* **2016,** *47* (1), 124-141.
27. Giannoukos, S.; Brkic, B.; Taylor, S.; Marshall, A.; Verbeck, G. F., Chemical Sniffing Instrumentation for Security Applications. *Chemical Reviews* **2016,** *116* (14), 8146-8172.
28. Ewing, R. G.; Waltman, M. J.; Atkinson, D. A.; Grate, J. W.; Hotchkiss, P. J., The vapor pressures of explosives. *Trac-Trends in Analytical Chemistry* **2013,** *42*, 35-48.
29. Östmark, H.; Wallin, S.; Ang, H. G., Vapor Pressure of Explosives: A Critical Review. *Propellants, Explosives, Pyrotechnics* **2012,** *37* (1), 12-23.
30. Fan, W.; Young, M.; Canino, J.; Smith, J.; Oxley, J.; Almirall, J. R., Fast detection of triacetone triperoxide (TATP) from headspace using planar solid-phase microextraction (PSPME) coupled to an IMS detector. *Analytical and Bioanalytical Chemistry* **2012,** *403* (2), 401-408.
31. Guerra-Diaz, P.; Gura, S.; Almirall, J. R., Dynamic Planar Solid Phase Microextraction-Ion Mobility Spectrometry for Rapid Field Air Sampling and Analysis of Illicit Drugs and Explosives. *Analytical Chemistry* **2010,** *82* (7), 2826-2835.
32. Gura, S.; Guerra-Diaz, P.; Lai, H.; Almirall, J. R., Enhancement in sample collection for the detection of MDMA using a novel planar SPME (PSPME) device coupled to ion mobility spectrometry (IMS). *Drug Testing and Analysis* **2009,** *1* (7-8), 355-362.
33. Gazit, I.; Terkel, J., Explosives detection by sniffer dogs following strenuous physical activity. *Applied Animal Behaviour Science* **2003,** *81* (2), 149-161.
34. Ong, T.-H.; Mendum, T.; Geurtsen, G.; Kelley, J.; Ostrinskaya, A.; Kunz, R., Use of mass spectrometric vapor analysis to improve canine explosive detection efficiency. *Analytical Chemistry* **2017,** *89* (12), 6482.
35. Carlsten, E. S.; Wicks, G. R.; Repasky, K. S.; Carlsten, J. L.; Bromenshenk, J. J.; Henderson, C. B., Field demonstration of a scanning lidar and detection algorithm for spatially mapping honeybees for biological detection of land mines. *Applied optics* **2011,** *50* (14), 2112.
36. Askim, J. R.; Mahmoudi, M.; Suslick, K. S., Optical sensor arrays for chemical sensing: the optoelectronic nose. *Chemical Society reviews* **2013,** *42* (22), 8649-8682.
37. Diehl, K. L.; Anslyn, E. V., Array sensing using optical methods for detection of chemical and biological hazards. *Chemical Society reviews* **2013,** *42* (22), 8596-8611.

38. Kozole, J.; Levine, L. A.; Tomlinson-Phillips, J.; Stairs, J. R., Gas phase ion chemistry of an ion mobility spectrometry based explosive trace detector elucidated by tandem mass spectrometry. *Talanta* **2015,** *140*, 10-19.
39. Ewing, R. G.; Waltman, M. J.; Atkinson, D. A., Characterization of Triacetone Triperoxide by Ion Mobility Spectrometry and Mass Spectrometry Following Atmospheric Pressure Chemical Ionization. *Analytical Chemistry* **2011,** *83* (12), 4838-4844.
40. Mäkinen, M.; Nousiainen, M.; Sillanpää, M., Ion spectrometric detection technologies for ultra-traces of explosives: A review. *Mass Spectrometry Reviews* **2011,** *30* (5), 940-973.
41. Buttigieg, G. A.; Knight, A. K.; Denson, S.; Pommier, C.; Bonner Denton, M., Characterization of the explosive triacetone triperoxide and detection by ion mobility spectrometry. *Forensic Science International* **2003,** *135* (1), 53-59.
42. Cook, G. W.; LaPuma, P. T.; Hook, G. L.; Eckenrode, B. A., Using Gas Chromatography with Ion Mobility Spectrometry to Resolve Explosive Compounds in the Presence of Interferents. *Journal of Forensic Sciences* **2010,** *55* (6), 1582-1591.
43. Crawford, C. L.; Hill, J. H. H., Evaluation of false positive responses by mass spectrometry and ion mobility spectrometry for the detection of trace explosives in complex samples. *Analytica chimica acta* **2013,** *795*, 36.
44. Fuchs, F.; Jarvis, J. P.; Hugger, S.; Kinzer, M.; Yang, Q.; Bronner, W.; Driad, R.; Aidam, R., Imaging Standoff Detection of Explosives by Diffuse Reflectance IR Laser Spectroscopy. In *Future Security: 7th Security Research Conference, Future Security 2012, Bonn, Germany, September 4-6, 2012. Proceedings*, Aschenbruck, N.; Martini, P.; Meier, M.; Tölle, J., Eds. Springer Berlin Heidelberg: Berlin, Heidelberg, 2012; pp 388-399.
45. Boyson, T. K.; Rittman, D. R.; Spence, T. G.; Calzada, M. E.; Kallapur, A. G.; Petersen, I. R.; Paul Kirkbride, K.; Moore, D. S.; Harb, C. C., Pulsed quantum cascade laser based hypertemporal real-time headspace measurements. *Opt. Express* **2014,** *22* (9), 10519.
46. Macleod, N. A.; Molero, F.; Weidmann, D., Broadband standoff detection of large molecules by mid-infrared active coherent laser spectrometry. *Opt. Express* **2015,** *23* (2), 912.
47. Ramos, C.; Dagdigian, P. J., Detection of vapors of explosives and explosive-related compounds by ultraviolet cavity ringdown spectroscopy. *Applied Optics* **2007,** *46* (4), 620-627.
48. Snels, M.; Venezia, T.; Belfiore, L., Detection and identification of TNT, 2,4-DNT and 2,6-DNT by near-infrared cavity ringdown spectroscopy. *Chemical Physics Letters* **2010,** *489* (1-3), 134-140.
49. Usachev, A. D.; Miller, T. S.; Singh, J. P.; Yueh, F. Y.; Jang, P. R.; Monts, D. L., Optical properties of gaseous 2,4,6-trinitrotoluene in the ultraviolet region. *Applied Spectroscopy* **2001,** *55* (2), 125-129.
50. Wojtas, J.; Stacewicz, T.; Bielecki, Z.; Rutecka, B.; Medrzycki, R.; Mikolajczyk, J., Towards optoelectronic detection of explosives. *Opto-Electron. Rev.* **2013,** *21* (2), 210-219.
51. Todd, M. W.; Provencal, R. A.; Owano, T. G.; Paldus, B. A.; Kachanov, A.; Vodopyanov, K. L.; Hunter, M.; Coy, S. L.; Steinfeld, J. I.; Arnold, J. T., Application of mid-infrared cavity-ringdown spectroscopy to trace explosives vapor detection using a broadly tunable (6-8 mm) optical parametric oscillator. *Applied Physics B-Lasers and Optics* **2002,** *75* (2-3), 367-376.
52. Brown, S. S., Absorption spectroscopy in high-finesse cavities for atmospheric studies. *Chemical Reviews* **2003,** *103* (12), 5219-5238.

53. Okeefe, A.; Deacon, D. A. G., Cavity ring-down optical spectrometer for absorption-measurements using pulsed laser sources. *Review of Scientific Instruments* **1988,** *59* (12), 2544-2551.
54. Taha, Y. M.; Odame-Ankrah, C. A.; Osthoff, H. D., Real-time vapor detection of nitroaromatic explosives by catalytic thermal dissociation blue diode laser cavity ring-down spectroscopy. *Chemical Physics Letters* **2013,** *582*, 15-20.
55. Paul, D.; Furgeson, A.; Osthoff, H. D., Measurement of total alkyl and peroxy nitrates by thermal decomposition cavity ring-down spectroscopy. *Review of Scientific Instruments* **2009,** *80*, 114101.
56. Brill, T. B.; James, K. J., Kinetics and mechanisms of thermal decomposition of nitroaromatic explosives. *Chemical Reviews* **1993,** *93* (8), 2667-2692.
57. Gray, P.; Griffiths, J. F.; Hasegawa, K., Non-Isothermal Decomposition Of Methyl Nitrate - Anomalous Reaction Order And Activation-Energies And Their Correction. *Int. J. Chem. Kinet.* **1981,** *13* (9), 817-831.
58. Pollard, F. H.; Marshall, H. S. B.; Pedler, A. E., The Thermal Decomposition of Ethyl Nitrate. *Transactions of the Faraday Society* **1956,** *52* (1), 59-68.
59. Pritchard, H. O., Thermal decomposition of isooctyl nitrate. *Combustion and Flame* **1989,** *75* (3-4), 415-416.
60. Day, D. A.; Wooldridge, P. J.; Dillon, M. B.; Thornton, J. A.; Cohen, R. C., A thermal dissociation laser-induced fluorescence instrument for in situ detection of NO2, peroxy nitrates, alkyl nitrates, and HNO3. *Journal of Geophysical Research-Atmospheres* **2002,** *107* (D5-6).
61. Content, S.; Trogler, W. C.; Sailor, M. J., Detection of Nitrobenzene, DNT, and TNT Vapors by Quenching of Porous Silicon Photoluminescence. *Chemistry – A European Journal* **2000,** *6* (12), 2205-2213.
62. Odame-Ankrah, C. A.; Osthoff, H. D., A compact diode laser cavity ring-down spectrometer for atmospheric measurements of NO_3 and N_2O_5 with automated zeroing and calibration. *Applied Spectroscopy* **2011,** *65* (11), 1260-1268.
63. Sharpe, S. W.; Johnson, T. J.; Sams, R. L.; Chu, P. M.; Rhoderick, G. C.; Johnson, P. A., Gas-phase databases for quantitative infrared spectroscopy. *Applied Spectroscopy* **2004,** *58* (12), 1452-1461.
64. Hanst, P. L.; Hanst, S. T., *Gas Analysis Manual for Analytical Chemists: Infrared measurement of gases and vapors. Quantitative reference spectra for gas analysis*. Infrared Analysis, Incorporated: 1990.
65. Paul, D.; Osthoff, H. D., Absolute Measurements of Total Peroxy Nitrate Mixing Ratios by Thermal Dissociation Blue Diode Laser Cavity Ring-Down Spectroscopy. *Analytical Chemistry* **2010,** *82* (15), 6695-6703.
66. Brown, S. S.; Stark, H.; Ciciora, S. J.; McLaughlin, R. J.; Ravishankara, A. R., Simultaneous in situ detection of atmospheric NO_3 and N_2O_5 via cavity ring-down spectroscopy. *Review of Scientific Instruments* **2002,** *73* (9), 3291-3301.
67. Everest, M. A.; Atkinson, D. B., Discrete sums for the rapid determination of exponential decay constants. *Review of Scientific Instruments* **2008,** *79* (2), 023108-9.
68. Halmer, D.; von Basum, G.; Hering, P.; Murtz, M., Fast exponential fitting algorithm for real-time instrumental use. *Review of Scientific Instruments* **2004,** *75* (6), 2187-2191.
69. Pella, P. A., Measurement of the vapor pressures of TNT, 2,4-DNT, 2,6-DNT, and EGDN. *The Journal of Chemical Thermodynamics* **1977,** *9* (4), 301-305.

70. Ferro, D.; Piacente, V.; Gigli, R.; D'Ascenzo, G., Determination of the vapour pressures of o-, m-, and p-dinitrobenzene by the torsion-effusion method. *The Journal of Chemical Thermodynamics* **1976,** *8* (12), 1137-1143.
71. Thaler, R. D.; Mielke, L. H.; Osthoff, H. D., Quantification of Nitryl Chloride at Part Per Trillion Mixing Ratios by Thermal Dissociation Cavity Ring-Down Spectroscopy. *Analytical Chemistry* **2011,** *83* (7), 2761-2766.
72. Rounbehler, D. P.; MacDonald, S. J.; Lieb, D. P.; Fine, D. H. In *Analysis of explosives using high speed gas chromatography with chemiluminescencent detection*, First International Symposium on Explosive Detection Technology, Atlantic City, NJ, Khan, S. M., Ed. U.S. Department of Transportation: Atlantic City, NJ, 1991; pp 703-713.
73. Riris, H.; Carlisle, C. B.; McMillen, D. F.; Cooper, D. E., Explosives detection with a frequency modulation spectrometer. *Appl. Opt.* **1996,** *35* (24), 4694-4704.
74. Lemire, G. W.; Simeonsson, J. B.; Sausa, R. C., Monitoring of vapor-phase nitro compounds using 226-nm radiation: fragmentation with subsequent NO resonance-enhanced multiphoton ionization detection. *Analytical Chemistry* **1993,** *65* (5), 529-533.
75. Ye, C. Z. Development of Purge-and-Trap Sample Preconcentrator for Enhanced Detection of Alkyl Nitrates by Thermal Dissociation Cavity Ring-Down Spectroscopy. University of Calgary, 2016.
76. Kleno, J. G.; Wolkoff, P.; Clausen, P. A.; Wilkins, C. K.; Pedersen, T., Degradation of the adsorbent Tenax TA by nitrogen oxides, ozone, hydrogen peroxide, OH radical, and limonene oxidation products. *Environmental Science & Technology* **2002,** *36* (19), 4121-4126.
77. Schneider, M.; Ballschmiter, K., C-3-C-14 alkyl nitrates in remote South Atlantic air. *Chemosphere* **1999,** *38* (1), 233-244.
78. Wojtas, J.; Rutecka, B.; Popiel, S.; Nawala, J.; Wesolowski, M.; Mikolajczyk, J.; Cudzilo, S.; Bielecki, Z., Explosives Vapors-Concentrating And Optoelectronic Detection. *Metrology and Measurement Systems* **2014,** *21* (2), 177-190.
79. Wild, R. J.; Edwards, P. M.; Dube, W. P.; Baumann, K.; Edgerton, E. S.; Quinn, P. K.; Roberts, J. M.; Rollins, A. W.; Veres, P. R.; Warneke, C.; Williams, E. J.; Yuan, B.; Brown, S. S., A Measurement of Total Reactive Nitrogen, NO_y, together with NO_2, NO, and O_3 via Cavity Ring-down Spectroscopy. *Environmental Science & Technology* **2014,** *48* (16), 9609-9615.
80. Rogers, R. N., Combined pyrolysis and thin layer chromatography - a method for study of decomposition mechanisms. *Analytical Chemistry* **1967,** *39* (7), 730-733.
81. Dacons, J. C.; Adolph, H. G.; Kamlet, M. J., Some Novel Observations Concerning Thermal Decomposition of 2,4,6-Trinitrotoluene. *Journal of Physical Chemistry* **1970,** *74* (16), 3035-3040.
82. Ng, W. L.; Field, J. E.; Hauser, H. M., Study Of Thermal-Decomposition Of Pentaerythritol Tetranitrate. *Journal of the Chemical Society-Perkin Transactions 2* **1976,** (6), 637-639.
83. Mohsen, Y.; Sanchez, J.-B.; Berger, F.; Lahlou, H.; Bezverkhyy, I.; Fierro, V.; Weber, G.; Celzard, A.; Bellat, J.-P., Selection and characterization of adsorbents for the analysis of an explosive-related molecule traces in the air. *Sensors and Actuators B-Chemical* **2013,** *176*, 124-131.
84. Clausen, P. A.; Wolkoff, P., Degradation products of Tenax TA formed during sampling and thermal desorption analysis: Indicators of reactive species indoors. *Atmospheric Environment* **1997,** *31* (5), 715-725.

85. Bianchi, F.; Bedini, A.; Riboni, N.; Pinalli, R.; Gregori, A.; Sidisky, L.; Dalcanale, E.; Careri, M., Cavitand-Based Solid-Phase Microextraction Coating for the Selective Detection of Nitroaromatic Explosives in Air and Soil. *Analytical Chemistry* **2014,** *86* (21), 10646-10652.
86. Oxley, J. C.; Smith, J. L.; Shinde, K.; Moran, J., Determination of the vapor density of triacetone triperoxide (TATP) using a gas chromatography headspace technique. *Propellants Explosives Pyrotechnics* **2005,** *30* (2), 127-130.
87. Mbah, J.; Knott, D.; Steward, S., Thermogravimetric study of vapor pressure of TATP synthesized without recrystallization. *Talanta* **2014,** *129*, 586-593.
88. Schulte-Ladbeck, R.; Vogel, M.; Karst, U., Recent methods for the determination of peroxide-based explosives. *Analytical and Bioanalytical Chemistry* **2006,** *386* (3), 559-565.
89. Dunayevskiy, I.; Tsekoun, A.; Prasanna, M.; Go, R.; Patel, C. K. N., High-sensitivity detection of triacetone triperoxide (TATP) and its precursor acetone. *Applied Optics* **2007,** *46* (25), 6397-6404.
90. Oxley, J. C.; Smith, J. L.; Huang, J. R.; Luo, W., Destruction of Peroxide Explosives. *Journal of Forensic Sciences* **2009,** *54* (5), 1029-1033.
91. Mayhew, C. A.; Sulzer, P.; Petersson, F.; Haidacher, S.; Jordan, A.; Mark, L.; Watts, P.; Mark, T. D., Applications of proton transfer reaction time-of-flight mass spectrometry for the sensitive and rapid real-time detection of solid high explosives. *International Journal of Mass Spectrometry* **2010,** *289* (1), 58-63.
92. Bauer, C.; Willer, U.; Schade, W., Use of quantum cascade lasers for detection of explosives: progress and challenges. *Optical Engineering* **2010,** *49* (11).
93. Fialkov, A. B.; Morag, M.; Amirav, A., A low thermal mass fast gas chromatograph and its implementation in fast gas chromatography mass spectrometry with supersonic molecular beams. *J. Chromatogr. A* **2011,** *1218* (52), 9375-9383.
94. Hildenbrand, J.; Herbst, J.; Wollenstein, J.; Lambrecht, A., Explosive detection using infrared laser spectroscopy. In *Quantum Sensing and Nanophotonic Devices Vi*, Razeghi, M.; Sudharsanan, R.; Brown, G. J., Eds. Spie-Int Soc Optical Engineering: Bellingham, 2009; Vol. 7222, p 72220B.
95. Mills, A.; Grosshans, P.; Snadden, E., Hydrogen peroxide vapour indicator. *Sensors and Actuators B: Chemical* **2009,** *136* (2), 458-463.
96. Girotti, S.; Ferri, E.; Maiolini, E.; Bolelli, L.; D'Elia, M.; Coppe, D.; Romolo, F. S., A quantitative chemiluminescent assay for analysis of peroxide-based explosives. *Analytical and Bioanalytical Chemistry* **2011,** *400* (2), 313-320.
97. Schulte-Ladbeck, R.; Karst, U., Determination of triacetonetriperoxide in ambient air. *Analytica Chimica Acta* **2003,** *482* (2), 183-188.
98. Lu, D.; Cagan, A.; Munoz, R. A. A.; Tangkuaram, T.; Wang, J., Highly sensitive electrochemical detection of trace liquid peroxide explosives at a Prussian-blue 'artificial-peroxidase' modified electrode. *Analyst* **2006,** *131* (12), 1279-1281.
99. Lin, H.; Suslick, K. S., A Colorimetric Sensor Array for Detection of Triacetone Triperoxide Vapor. *Journal of the American Chemical Society* **2010,** *132* (44), 15519-15521.
100. Walter, M. A.; Pfeifer, D.; Kraus, W.; Emmerling, F.; Schneider, R. J.; Panne, U.; Weller, M. G., Triacetone Triperoxide (TATP): Hapten Design and Development of Antibodies. *Langmuir* **2010,** *26* (19), 15418-15423.

101. Warmer, J.; Wagner, P.; Schoning, M. J.; Kaul, P., Detection of triacetone triperoxide using temperature cycled metal-oxide semiconductor gas sensors. *Phys. Status Solidi A-Appl. Mat.* **2015,** *212* (6), 1289-1298.
102. Lightfoot, P. D.; Cox, R. A.; Crowley, J. N.; Destriau, M.; Hayman, G. D.; Jenkin, M. E.; Moortgat, G. K.; Zabel, F., Organic Peroxy-Radicals - Kinetics, Spectroscopy And Tropospheric Chemistry. *Atmospheric Environment Part A-General Topics* **1992,** *26* (10), 1805-1961.
103. Monks, P. S., Gas-phase radical chemistry in the troposphere. *Chemical Society Reviews* **2005,** *34* (5), 376-395.
104. Kirchner, F.; Stockwell, W. R., Effect of peroxy radical reactions on the predicted concentrations of ozone, nitrogenous compounds, and radicals. *Journal of Geophysical Research-Atmospheres* **1996,** *101* (D15), 21007-21022.
105. Fleming, Z. L.; Monks, P. S.; Rickard, A. R.; Heard, D. E.; Bloss, W. J.; Seakins, P. W.; Still, T. J.; Sommariva, R.; Pilling, M. J.; Morgan, R.; Green, T. J.; Brough, N.; Mills, G. P.; Penkett, S. A.; Lewis, A. C.; Lee, J. D.; Saiz-Lopez, A.; Plane, J. M. C., Peroxy radical chemistry and the control of ozone photochemistry at Mace Head, Ireland during the summer of 2002. *Atmospheric Chemistry and Physics* **2006,** *6*, 2193-2214.
106. Bates, D. R.; Nicolet, M., THE PHOTOCHEMISTRY OF ATMOSPHERIC WATER VAPOR. *J. Geophys. Res.* **1950,** *55* (3), 301-327.
107. Stenke, A.; Grewe, V., Simulation of stratospheric water vapor trends: impact on stratospheric ozone chemistry. *Atmospheric Chemistry and Physics* **2005,** *5*, 1257-1272.
108. Ziemann, P. J.; Atkinson, R., Kinetics, products, and mechanisms of secondary organic aerosol formation. *Chemical Society Reviews* **2012,** *41* (19), 6582-6605.
109. Ehn, M.; Thornton, J. A.; Kleist, E.; Sipila, M.; Junninen, H.; Pullinen, I.; Springer, M.; Rubach, F.; Tillmann, R.; Lee, B.; Lopez-Hilfiker, F.; Andres, S.; Acir, I.-H.; Rissanen, M.; Jokinen, T.; Schobesberger, S.; Kangasluoma, J.; Kontkanen, J.; Nieminen, T.; Kurten, T.; Nielsen, L. B.; Jorgensen, S.; Kjaergaard, H. G.; Canagaratna, M.; Maso, M. D.; Berndt, T.; Petaja, T.; Wahner, A.; Kerminen, V.-M.; Kulmala, M.; Worsnop, D. R.; Wildt, J.; Mentel, T. F., A large source of low-volatility secondary organic aerosol. *Nature* **2014,** *506* (7489), 476-479.
110. Crounse, J. D.; Nielsen, L. B.; Jorgensen, S.; Kjaergaard, H. G.; Wennberg, P. O., Autoxidation of Organic Compounds in the Atmosphere. *J. Phys. Chem. Lett.* **2013,** *4* (20), 3513-3520.
111. Griffith, S. M.; Hansen, R. F.; Dusanter, S.; Michoud, V.; Gilman, J. B.; Kuster, W. C.; Veres, P. R.; Graus, M.; de Gouw, J. A.; Roberts, J.; Young, C.; Washenfelder, R.; Brown, S. S.; Thalman, R.; Waxman, E.; Volkamer, R.; Tsai, C.; Stutz, J.; Flynn, J. H.; Grossberg, N.; Lefer, B.; Alvarez, S. L.; Rappenglueck, B.; Mielke, L. H.; Osthoff, H. D.; Stevens, P. S., Measurements of hydroxyl and hydroperoxy radicals during CalNex-LA: Model comparisons and radical budgets. *Journal of Geophysical Research-Atmospheres* **2016,** *121* (8), 4211-4232.
112. Cantrell, C. A.; Stedman, D. H., A Possible Technique For The Measurement Of Atmospheric Peroxy-Radicals. *Geophysical Research Letters* **1982,** *9* (8), 846-849.
113. Cantrell, C. A.; Stedman, D. H.; Wendel, G. J., Measurement of atmospheric peroxy-radicals by chemical amplification. *Analytical Chemistry* **1984,** *56* (8), 1496-1502.
114. Hastie, D. R.; Weissenmayer, M.; Burrows, J. P.; Harris, G. W., Calibrated chemical amplifier for atmospheric RO_x measurements. *Analytical Chemistry* **1991,** *63* (18), 2048-2057.

115. Cantrell, C. A.; Shetter, R. E.; Lind, J. A.; McDaniel, A. H.; Calvert, J. G.; Parrish, D. D.; Fehsenfeld, F. C.; Buhr, M. P.; Trainer, M., An Improved Chemical Amplifier Technique For Peroxy Radical Measurements. *J. Geophys. Res.* **1993,** *98* (D2), 2897-2909.
116. Hu, J.; Stedman, D. H., Free-Radical Detector For Tropospheric Measurement Using Chemical Amplification. *Analytical Chemistry* **1994,** *66* (20), 3384-3393.
117. Clemitshaw, K. C.; Carpenter, L. J.; Penkett, S. A.; Jenkin, M. E., A calibrated peroxy radical chemical amplifier for ground-based tropospheric measurements. *Journal of Geophysical Research-Atmospheres* **1997,** *102* (D21), 25405-25416.
118. Mihele, C. M.; Hastie, D. R., Optimized operation and calibration procedures for radical amplifier-type detectors. *J. Atmos. Ocean. Technol.* **2000,** *17* (6), 788-794.
119. Green, T. J.; Reeves, C. E.; Fleming, Z. L.; Brough, N.; Rickard, A. R.; Bandy, B. J.; Monks, P. S.; Penkett, S. A., An improved dual channel PERCA instrument for atmospheric measurements of peroxy radicals. *Journal of Environmental Monitoring* **2006,** *8* (5), 530-536.
120. Sadanaga, Y.; Matsumoto, J.; Sakurai, K.; Isozaki, R.; Kato, S.; Nomaguchi, T.; Bandow, H.; Kajii, Y., Development of a measurement system of peroxy radicals using a chemical amplification/laser-induced fluorescence technique. *Review of Scientific Instruments* **2004,** *75* (4), 864-872.
121. Li, X. Q.; Qi, B.; Zeng, L. M.; Tang, X. Y., Development and deployment of an instrument for measurement of atmospheric peroxy radical by chemical amplification. *Science in China Series D-Earth Sciences* **2009,** *52* (3), 333-340.
122. Liu, Y.; Morales-Cueto, R.; Hargrove, J.; Medina, D.; Zhang, J., Measurements of Peroxy Radicals Using Chemical Amplification-Cavity Ringdown Spectroscopy. *Environmental Science & Technology* **2009,** *43* (20), 7791-7796.
123. Miyazaki, K.; Parker, A. E.; Fittschen, C.; Monks, P. S.; Kajii, Y., A new technique for the selective measurement of atmospheric peroxy radical concentrations of HO2 and RO2 using a denuding method. *Atmos. Meas. Tech.* **2010,** *3* (6), 1547-1554.
124. Kartal, D.; Andres-Hernandez, M. D.; Reichert, L.; Schlager, H.; Burrows, J. P., Technical Note: Characterisation of a DUALER instrument for the airborne measurement of peroxy radicals during AMMA 2006. *Atmospheric Chemistry and Physics* **2010,** *10* (6), 3047-3062.
125. Wood, E. C.; Charest, J. R., Chemical Amplification - Cavity Attenuated Phase Shift Spectroscopy Measurements of Atmospheric Peroxy Radicals. *Analytical Chemistry* **2014,** *86* (20), 10266-10273.
126. Liu, Y.; Zhang, J., Atmospheric Peroxy Radical Measurements Using Dual-Channel Chemical Amplification Cavity Ringdown Spectroscopy. *Analytical Chemistry* **2014,** *86* (11), 5391-5398.
127. Horstjann, M.; Andres Hernandez, M. D.; Nenakhov, V.; Chrobry, A.; Burrows, J. P., Peroxy radical detection for airborne atmospheric measurements using absorption spectroscopy of NO2. *Atmos. Meas. Tech.* **2014,** *7* (5), 1245-1257.
128. Wang, Z.; Yang, B.; Zhang, T., A method for the selective measurement of HO2 and RO2 radical concentrations using a Nafion-PERCA system. *Journal of Atmospheric Chemistry* **2016,** *73* (4), 397-406.
129. Chen, Y.; Yang, C.; Zhao, W.; Fang, B.; Xu, X.; Gai, Y.; Lin, X.; Chen, W.; Zhang, W., Ultra-sensitive measurement of peroxy radicals by chemical amplification broadband cavity-enhanced spectroscopy. *Analyst* **2016,** *141* (20), 5870-5878.

130. Cantrell, C. A.; Shetter, R. E.; Calvert, J. G., Dual-inlet chemical amplifier for atmospheric peroxy radical measurements. *Analytical Chemistry* **1996,** *68* (23), 4194-4199.
131. Wood, E. C.; Deming, B. L.; Kundu, S., Ethane-Based Chemical Amplification Measurement Technique for Atmospheric Peroxy Radicals. *Environmental Science & Technology Letters* **2016,** *4* (1), 15-19.
132. Mihele, C. M.; Hastie, D. R., The sensitivity of the radical amplifier to ambient water vapour. *Geophysical Research Letters* **1998,** *25* (11), 1911-1913.
133. Mihele, C. M.; Mozurkewich, M.; Hastie, D. R., Radical loss in a chain reaction of CO and NO in the presence of water: Implications for the radical amplifier and atmospheric chemistry. *Int. J. Chem. Kinet.* **1999,** *31* (2), 145-152.
134. Lure, B. A.; Svetlov, B. S., The kinetic-parameters of the primary stage of thermal-decomposition of organic nitrates. *Kinet. Catal.* **1994,** *35* (2), 145-154.
135. Griffiths, J. F.; Gilligan, M. F.; Gray, P., Pyrolysis of isopropyl nitrate .1. Decomposition at low-temperatures and pressures. *Combustion and Flame* **1975,** *24* (1), 11-19.
136. Ewing, R. G.; Clowers, B. H.; Atkinson, D. A., Direct Real-Time Detection of Vapors from Explosive Compounds. *Analytical Chemistry* **2013,** *85* (22), 10977-10983.
137. Anastasi, C.; Gladstone, R. V.; Sanderson, M. G., Chemical amplifiers for detection of peroxy-radicals in the atmosphere. *Environmental Science & Technology* **1993,** *27* (3), 474-482.
138. Jenkin, M. E.; Saunders, S. M.; Pilling, M. J., The tropospheric degradation of volatile organic compounds: a protocol for mechanism development. *Atmospheric Environment* **1997,** *31* (1), 81-104.
139. Saunders, S. M.; Jenkin, M. E.; Derwent, R. G.; Pilling, M. J., Protocol for the development of the Master Chemical Mechanism, MCM v3 (Part A): tropospheric degradation of non-aromatic volatile organic compounds. *Atmospheric Chemistry and Physics* **2003,** *3*, 161-180.
140. Kabir, M.; Jagiella, S.; Zabel, F., Thermal Stability of n-Acyl Peroxynitrates. *Int. J. Chem. Kinet.* **2014,** *46* (8), 462-469.
141. Jenkin, M. E.; Wyche, K. P.; Evans, C. J.; Carr, T.; Monks, P. S.; Alfarra, M. R.; Barley, M. H.; McFiggans, G. B.; Young, J. C.; Rickard, A. R., Development and chamber evaluation of the MCM v3.2 degradation scheme for β-caryophyllene. *Atmospheric Chemistry and Physics* **2012,** *12* (11), 5275-5308.
142. Sandu, A.; Sander, R., Technical note: Simulating chemical systems in Fortran90 and Matlab with the Kinetic PreProcessor KPP-2.1. *Atmospheric Chemistry and Physics* **2006,** *6*, 187-195.
143. Kanno, N.; Tonokura, K.; Koshi, M., Equilibrium constant of the HO_2-H_2O complex formation and kinetics of HO_2+HO_2-H_2O: Implications for tropospheric chemistry. *Journal of Geophysical Research-Atmospheres* **2006,** *111* (D20).
144. Butkovskaya, N.; Kukui, A.; Le Bras, G., HNO3 forming channel of the HO2+NOreaction as a function of pressure and temperature in the ranges of 72-600 torr and 223-323 K. *J. Phys. Chem. A* **2007,** *111* (37), 9047-9053.
145. Butkovskaya, N.; Rayez, M. T.; Rayez, J. C.; Kukui, A.; Le Bras, G., Water Vapor Effect on the HNO_3 Yield in the HO_2 + NO Reaction: Experimental and Theoretical Evidence. *J. Phys. Chem. A* **2009,** *113* (42), 11327-11342.
146. Burkholder, J. B.; Sander, S. P.; Abbatt, J. P. D.; Barker, J. R.; Huie, R. E.; Kolb, C. E.; Kurylo, M. J.; Orkin, V. L.; Wilmouth, D. M.; Wine, P. H., *Chemical Kinetics and*

Photochemical Data for Use in Atmospheric Studies, Evaluation Number 18. National Aeronautics and Space Administration, Jet Propulsion Laboratory, California Institute of Technology: Pasadena, California, 2015.
147. Steacie, E. W. R.; Shaw, G. T., The homogeneous unimolecular decomposition of gaseous methyl nitrite. *Proceedings of the Royal Society of London Series a-Containing Papers of a Mathematical and Physical Character* **1934,** *146* (A857), 0388-0395.
148. Atkinson, R.; Baulch, D. L.; Cox, R. A.; Crowley, J. N.; Hampson, R. F.; Hynes, R. G.; Jenkin, M. E.; Rossi, M. J.; Troe, J., Evaluated kinetic and photochemical data for atmospheric chemistry: Volume I - gas phase reactions of O-x, HOx, NOx and SOx species. *Atmospheric Chemistry and Physics* **2004,** *4*, 1461-1738.
149. Kretschmer, C. B.; Wiebe, R., Liquid-Vapor Equilibrium of Ethanol--Toluene Solutions. *Journal of the American Chemical Society* **1949,** *71* (5), 1793-1797.
150. Perring, A. E.; Pusede, S. E.; Cohen, R. C., An Observational Perspective on the Atmospheric Impacts of Alkyl and Multifunctional Nitrates on Ozone and Secondary Organic Aerosol. *Chemical Reviews* **2013,** *113* (8), 5848-5870.
151. Solomon, S., Stratospheric ozone depletion: A review of concepts and history. *Rev. Geophys.* **1999,** *37* (3), 275-316.
152. Portmann, R. W.; Brown, S. S.; Gierczak, T.; Talukdar, R. K.; Burkholder, J. B.; Ravishankara, A. R., Role of nitrogen oxides in the stratosphere: A reevaluation based on laboratory studies. *Geophysical Research Letters* **1999,** *26* (15), 2387-2390.
153. Singh, H. B.; Herlth, D.; Ohara, D.; Zahnle, K.; Bradshaw, J. D.; Sandholm, S. T.; Talbot, R.; Crutzen, P. J.; Kanakidou, M., RELATIONSHIP OF PEROXYACETYL NITRATE TO ACTIVE AND TOTAL ODD NITROGEN AT NORTHERN HIGH-LATITUDES - INFLUENCE OF RESERVOIR SPECIES ON NOX AND O3. *Journal of Geophysical Research-Atmospheres* **1992,** *97* (D15), 16523-16530.
154. Roberts, J. M., The atmospheric chemistry of organic nitrates. *Atmos. Environ. A* **1990,** *24* (2), 243-287.
155. Slusher, D. L.; Pitteri, S. J.; Haman, B. J.; Tanner, D. J.; Huey, L. G., A chemical ionization technique for measurement of pernitric acid in the upper troposphere and the polar boundary layer. *Geophysical Research Letters* **2001,** *28* (20), 3875-3878.
156. Davis, D.; Chen, G.; Buhr, M.; Crawford, J.; Lenschow, D.; Lefer, B.; Shetter, R.; Eisele, F.; Mauldin, L.; Hogan, A., South Pole NOx chemistry: an assessment of factors controlling variability and absolute levels. *Atmospheric Environment* **2004,** *38* (32), 5375-5388.
157. Jones, A. E.; Brough, N.; Anderson, P. S.; Wolff, E. W., HO_2NO_2 and HNO_3 in the coastal Antarctic winter night: a "lab-in-the-field" experiment. *Atmospheric Chemistry and Physics* **2014,** *14* (21), 11843-11851.
158. Kim, S.; Huey, L. G.; Stickel, R. E.; Tanner, D. J.; Crawford, J. H.; Olson, J. R.; Chen, G.; Brune, W. H.; Ren, X.; Lesher, R.; Wooldridge, P. J.; Bertram, T. H.; Perring, A.; Cohen, R. C.; Lefer, B. L.; Shetter, R. E.; Avery, M.; Diskin, G.; Sokolik, I., Measurement of HO_2NO_2 in the free troposphere during the Intercontinental Chemical Transport Experiment–North America 2004. *Journal of Geophysical Research: Atmospheres* **2007,** *112* (D12), n/a-n/a.
159. Murphy, J. G.; Thornton, J. A.; Wooldridge, P. J.; Day, D. A.; Rosen, R. S.; Cantrell, C.; Shetter, R. E.; Lefer, B.; Cohen, R. C., Measurements of the sum of HO_2NO_2 and $CH_3O_2NO_2$ in the remote troposphere. *Atmospheric Chemistry and Physics* **2004,** *4*, 377-384.

160. Veres, P. R.; Roberts, J. M.; Wild, R. J.; Edwards, P. M.; Brown, S. S.; Bates, T. S.; Quinn, P. K.; Johnson, J. E.; Zamora, R. J.; de Gouw, J., Peroxynitric acid (HO_2NO_2) measurements during the UBWOS 2013 and 2014 studies using iodide ion chemical ionization mass spectrometry. *Atmospheric Chemistry and Physics* **2015,** *15* (14), 8101-8114.
161. Spencer, K. M.; McCabe, D. C.; Crounse, J. D.; Olson, J. R.; Crawford, J. H.; Weinheimer, A. J.; Knapp, D. J.; Montzka, D. D.; Cantrell, C. A.; Hornbrook, R. S.; Mauldin, R. L.; Wennberg, P. O., Inferring ozone production in an urban atmosphere using measurements of peroxynitric acid. *Atmospheric Chemistry and Physics* **2009,** *9* (11), 3697-3707.
162. Chen, D.; Huey, L. G.; Tanner, D. J.; Li, J.; Ng, N. L.; Wang, Y., Derivation of Hydroperoxyl Radical Levels at an Urban Site via Measurement of Pernitric Acid by Iodide Chemical Ionization Mass Spectrometry. *Environmental Science & Technology* **2017,** *51* (6), 3355-3363.
163. Tuazon, E. C.; Winer, A. M.; Pitts, J. N., TRACE POLLUTANT CONCENTRATIONS IN A MULTIDAY SMOG EPISODE IN THE CALIFORNIA SOUTH COAST AIR BASIN BY LONG PATH-LENGTH FOURIER-TRANSFORM INFRARED-SPECTROSCOPY. *Environmental Science & Technology* **1981,** *15* (10), 1232-1237.
164. Eisele, F.; Davis, D. D.; Helmig, D.; Oltmans, S. J.; Neff, W.; Huey, G.; Tanner, D.; Chen, G.; Crawford, J.; Arimoto, R.; Buhr, M.; Mauldin, L.; Hutterli, M.; Dibb, J.; Blake, D.; Brooks, S. B.; Johnson, B.; Roberts, J. M.; Wang, Y. H.; Tan, D.; Flocke, F., Antarctic Tropospheric Chemistry Investigation (ANTCI) 2003 overview. *Atmospheric Environment* **2008,** *42* (12), 2749-2761.
165. Mills, G. P.; Sturges, W. T.; Salmon, R. A.; Bauguitte, S. J. B.; Read, K. A.; Bandy, B. J., Seasonal variation of peroxyacetylnitrate (PAN) in coastal Antarctica measured with a new instrument for the detection of sub-part per trillion mixing ratios of PAN. *Atmospheric Chemistry and Physics* **2007,** *7* (17), 4589-4599.
166. Singh, H. B.; Brune, W. H.; Crawford, J. H.; Jacob, D. J.; Russell, P. B., Overview of the summer 2004 Intercontinental Chemical Transport Experiment–North America (INTEX-A). *Journal of Geophysical Research: Atmospheres* **2006,** *111* (D24), n/a-n/a.
167. Ahmadov, R.; McKeen, S.; Trainer, M.; Banta, R.; Brewer, A.; Brown, S.; Edwards, P. M.; de Gouw, J. A.; Frost, G. J.; Gilman, J.; Helmig, D.; Johnson, B.; Karion, A.; Koss, A.; Langford, A.; Lerner, B.; Olson, J.; Oltmans, S.; Peischl, J.; Pétron, G.; Pichugina, Y.; Roberts, J. M.; Ryerson, T.; Schnell, R.; Senff, C.; Sweeney, C.; Thompson, C.; Veres, P. R.; Warneke, C.; Wild, R.; Williams, E. J.; Yuan, B.; Zamora, R., Understanding high wintertime ozone pollution events in an oil- and natural gas-producing region of the western US. *Atmospheric Chemistry and Physics* **2015,** *15* (1), 411-429.
168. Lee, L.; Wooldridge, P. J.; deGouw, J.; Brown, S. S.; Bates, T. S.; Quinn, P. K.; Cohen, R. C., Particulate organic nitrates observed in an oil and natural gas production region during wintertime. *Atmospheric Chemistry and Physics* **2015,** *15* (16), 9313-9325.
169. Lee, J. B.; Yoon, J. S.; Jung, K.; Eom, S. W.; Chae, Y. Z.; Cho, S. J.; Kim, S. D.; Sohn, J. R.; Kim, K. H., Peroxyacetyl nitrate (PAN) in the urban atmosphere. *Chemosphere* **2013,** *93* (9), 1796-1803.
170. Roberts, J. M., PAN and Related Compounds. In *Volatile Organic Compounds in the Atmosphere*, Koppmann, R., Ed. Blackwell Publishing: Oxford, UK, 2007; pp 221-268.
171. Wooldridge, P. J.; Perring, A. E.; Bertram, T. H.; Flocke, F. M.; Roberts, J. M.; Singh, H. B.; Huey, L. G.; Thornton, J. A.; Wolfe, G. M.; Murphy, J. G.; Fry, J. L.; Rollins, A. W.;

LaFranchi, B. W.; Cohen, R. C., Total Peroxy Nitrates (SPNs) in the atmosphere: the Thermal Dissociation-Laser Induced Fluorescence (TD-LIF) technique and comparisons to speciated PAN measurements. *Atmos. Meas. Tech.* **2010,** *3* (3), 593-607.
172. Zheng, W.; Flocke, F. M.; Tyndall, G. S.; Swanson, A.; Orlando, J. J.; Roberts, J. M.; Huey, L. G.; Tanner, D. J., Characterization of a thermal decomposition chemical ionization mass spectrometer for the measurement of peroxy acyl nitrates (PANs) in the atmosphere. *Atmospheric Chemistry and Physics* **2011,** *11* (13), 6529-6547.
173. Tokarek, T. W.; Huo, J. A.; Odame-Ankrah, C. A.; Hammoud, D.; Taha, Y. M.; Osthoff, H. D., A gas chromatograph for quantification of peroxycarboxylic nitric anhydrides calibrated by thermal dissociation cavity ring-down spectroscopy. *Atmospheric Measurement Techniques* **2014,** *7* (10), 3263-3283.
174. Di Carlo, P.; Aruffo, E.; Busilacchio, M.; Giammaria, F.; Dari-Salisburgo, C.; Biancofiore, F.; Visconti, G.; Lee, J.; Moller, S.; Reeves, C. E.; Bauguitte, S.; Forster, G.; Jones, R. L.; Ouyang, B., Aircraft based four-channel thermal dissociation laser induced fluorescence instrument for simultaneous measurements of NO2, total peroxy nitrate, total alkyl nitrate, and HNO3. *Atmospheric Measurement Techniques* **2013,** *6* (4), 971-980.
175. Thieser, J.; Schuster, G.; Schuladen, J.; Phillips, G. J.; Reiffs, A.; Parchatka, U.; Pöhler, D.; Lelieveld, J.; Crowley, J. N., A two-channel thermal dissociation cavity ring-down spectrometer for the detection of ambient NO_2, RO_2NO_2 and $RONO_2$. *Atmos. Meas. Tech.* **2016,** *9* (2), 553-576.
176. Sobanski, N.; Schuladen, J.; Schuster, G.; Lelieveld, J.; Crowley, J. N., A five-channel cavity ring-down spectrometer for the detection of NO_2, NO_3, N_2O_5, total peroxy nitrates and total alkyl nitrates. *Atmos. Meas. Tech.* **2016,** *9* (10), 5103-5118.
177. Womack, C. C.; Neuman, J. A.; Veres, P. R.; Eilerman, S. J.; Brock, C. A.; Decker, Z. C. J.; Zarzana, K. J.; Dube, W. P.; Wild, R. J.; Wooldridge, P. J.; Cohen, R. C.; Brown, S. S., Evaluation of the accuracy of thermal dissociation CRDS and LIF techniques for atmospheric measurement of reactive nitrogen species. *Atmospheric Measurement Techniques* **2017,** *10* (5), 1911-1926.
178. Sadanaga, Y.; Takaji, R.; Ishiyama, A.; Nakajima, K.; Matsuki, A.; Bandow, H., Thermal dissociation cavity attenuated phase shift spectroscopy for continuous measurement of total peroxy and organic nitrates in the clean atmosphere. *Review of Scientific Instruments* **2016,** *87* (7), 074102.
179. Fuchs, H.; Dube, W.; Lerner, B.; Wagner, N.; Williams, E.; Brown, S., A Sensitive and Versatile Detector for Atmospheric NO2 and NOx Based on Blue Diode Laser Cavity Ring-Down Spectroscopy. *Environmental Science & Technology* **2009,** *43* (20), 7831-7836.
180. Hanke, M.; Uecker, J.; Reiner, T.; Arnold, F., Atmospheric peroxy radicals: ROXMAS, a new mass-spectrometric methodology for speciated measurements of HO_2 and $\sum RO_2$ and first results. *International Journal of Mass Spectrometry* **2002,** *213* (2), 91-99.
181. Edwards, G. D.; Cantrell, C. A.; Stephens, S.; Hill, B.; Goyea, O.; Shetter, R. E.; Mauldin, R. L.; Kosciuch, E.; Tanner, D. J.; Eisele, F. L., Chemical ionization mass spectrometer instrument for the measurement of tropospheric HO_2 and RO_2. *Analytical Chemistry* **2003,** *75* (20), 5317-5327.
182. Chen, G.; Davis, D.; Crawford, J.; Hutterli, L. M.; Huey, L. G.; Slusher, D.; Mauldin, L.; Eisele, F.; Tanner, D.; Dibb, J.; Buhr, M.; McConnell, J.; Lefer, B.; Shetter, R.; Blake, D.; Song,

C. H.; Lombardi, K.; Arnoldy, J., A reassessment of HOx South Pole chemistry based on observations recorded during ISCAT 2000. *Atmospheric Environment* **2004,** *38* (32), 5451-5461.
183. Slusher, D. L.; Huey, L. G.; Tanner, D. J.; Flocke, F. M.; Roberts, J. M., A thermal dissociation-chemical ionization mass spectrometry (TD-CIMS) technique for the simultaneous measurement of peroxyacyl nitrates and dinitrogen pentoxide. *Journal of Geophysical Research-Atmospheres* **2004,** *109* (D19).
184. Hornbrook, R. S.; Crawford, J. H.; Edwards, G. D.; Goyea, O.; Mauldin, R. L.; Olson, J. S.; Cantrell, C. A., Measurements of tropospheric HO_2 and RO_2 by oxygen dilution modulation and chemical ionization mass spectrometry. *Atmospheric Measurement Techniques* **2011,** *4* (4), 735-756.
185. Faloona, I. C.; Tan, D.; Lesher, R. L.; Hazen, N. L.; Frame, C. L.; Simpas, J. B.; Harder, H.; Martinez, M.; Di Carlo, P.; Ren, X. R.; Brune, W. H., A laser-induced fluorescence instrument for detecting tropospheric OH and HO_2: Characteristics and calibration. *Journal Of Atmospheric Chemistry* **2004,** *47* (2), 139-167.
186. Heard, D. E., Atmospheric field measurements of the hydroxyl radical using laser-induced fluorescence spectroscopy. *Annual Review Of Physical Chemistry* **2006,** *57*, 191-216.
187. Fuchs, H.; Holland, F.; Hofzumahaus, A., Measurement of tropospheric RO_2 and HO_2 radicals by a laser-induced fluorescence instrument. *Review of Scientific Instruments* **2008,** *79* (8), 084104-12.
188. Dusanter, S.; Vimal, D.; Stevens, P. S.; Volkamer, R.; Molina, L. T., Measurements of OH and HO_2 concentrations during the MCMA-2006 field campaign – Part 1: Deployment of the Indiana University laser-induced fluorescence instrument. *Atmospheric Chemistry and Physics* **2009,** *9* (5), 1665-1685.
189. Blanchard, P.; Shepson, P. B.; Schiff, H. I.; Drummond, J. W., Development of a gas-chromatograph for trace-level measurement of peroxyacetyl nitrate using chemical amplification. *Analytical Chemistry* **1993,** *65* (18), 2472-2477.
190. Odame-Ankrah, C. A. Improved detection instrument for nitrogen oxide species. University of Calgary, http://hdl.handle.net/11023/2006, Calgary, 2015.
191. Mielke, L. H.; Furgeson, A.; Osthoff, H. D., Observation of $ClNO_2$ in a mid-continental urban environment. *Environmental Science & Technology* **2011,** *45* (20), 8889-8896.
192. Mielke, L. H.; Osthoff, H. D., On quantitative measurements of peroxycarboxylic nitric anhydride mixing ratios by thermal dissociation chemical ionization mass spectrometry. *International Journal of Mass Spectrometry* **2012,** *310*, 1-9.
193. Abida, O.; Mielke, L. H.; Osthoff, H. D., Observation of gas-phase peroxynitrous and peroxynitric acid during the photolysis of nitrate in acidified frozen solutions. *Chemical Physics Letters* **2011,** *511* (4-6), 187-192.
194. Furgeson, A.; Mielke, L. H.; Paul, D.; Osthoff, H. D., A photochemical source of peroxypropionic and peroxyisobutanoic nitric anhydride. *Atmospheric Environment* **2011,** *45* (28), 5025-5032.
195. Grosjean, D.; Grosjean, E.; Williams, E. L., Thermal decomposition of PAN, PPN and vinyl-PAN. *J. Air Waste Manage. Assoc.* **1994,** *44* (4), 391-396.
196. Atkinson, R.; Baulch, D. L.; Cox, R. A.; Hampson, R. F.; Kerr, J. A.; Rossi, M. J.; Troe, J., Evaluated kinetic, photochemical and heterogeneous data for atmospheric chemistry .5. IUPAC Subcommittee on Gas Kinetic Data Evaluation for Atmospheric Chemistry. *J. Phys. Chem. Ref. Data* **1997,** *26* (3), 521-1011.

197. Jones, W. M.; Davidson, N., Thermal decomposition of ozone in a shock tube. *Journal of the American Chemical Society* **1962,** *84* (15), 2868-&.
198. Heimerl, J. M.; Coffee, T. P., Unimolecular ozone decomposition reaction. *Combustion and Flame* **1979,** *35* (2), 117-123.
199. Baulch, D. L.; Cobos, C. J.; Cox, R. A.; Frank, P.; Hayman, G.; Just, T.; Kerr, J. A.; Murrells, T.; Pilling, M. J.; Troe, J.; Walker, R. W.; Warnatz, J., Summary table of evaluated kinetic data for combustion modeling: Supplement 1. *Combustion and Flame* **1994,** *98* (1), 59-79.
200. Hippler, H.; Rahn, R.; Troe, J., TEMPERATURE AND PRESSURE-DEPENDENCE OF OZONE FORMATION RATES IN THE RANGE 1-1000-BAR AND 90-370-K. *J. Chem. Phys.* **1990,** *93* (9), 6560-6569.
201. Weschler, C. J., Ozone in indoor environments: Concentration and chemistry. *Indoor Air-International Journal of Indoor Air Quality and Climate* **2000,** *10* (4), 269-288.
202. Taha, Y. M.; Saowapon, M. T.; Osthoff, H., Detection of triacetone triperoxide by thermal decomposition peroxy radical chemical amplification coupled to cavity ring-down spectroscopy. *Analytical and Bioanalytical Chemistry* **2018**.
203. Oxley, J. C.; Smith, J. L.; Bowden, P. R.; Rettinger, R. C., Factors Influencing Triacetone Triperoxide (TATP) and Diacetone Diperoxide (DADP) Formation: Part I. *Propellants, Explosives, Pyrotechnics* **2013,** *38* (2), 244-254.
204. Guo, C.; Persons, J.; Woodford, J. N.; Harbison, G. S., Gas-Phase Infrared and NMR Investigation of the Conformers of Diacetone Diperoxide (DADP). *The Journal of Physical Chemistry A* **2015,** *119* (40), 10221-10228.
205. Pacheco-Londono, L.; Pena, A. J.; Primera, O. M.; Hernandez-Rivera, S. P.; Mina, N.; Garcia, R.; Chamberlain, R. T.; Lareau, R., An experimental and theoretical study of the synthesis and vibrational spectroscopy of triacetone triperoxide (TATP). In *Sensors, and Command, Control, Communications, and Intelligence(C31) Technologies for Homeland Security and Homeland Defense Iii, Pts 1 and 2*, Carapezza, E. M., Ed. Spie-Int Soc Optical Engineering: Bellingham, 2004; Vol. 5403, pp 279-287.
206. Brauer, B.; Dubnikova, F.; Zeiri, Y.; Kosloff, R.; Gerber, R. B., Vibrational spectroscopy of triacetone triperoxide (TATP): Anharmonic fundamentals, overtones and combination bands. *Spectroc. Acta Pt. A-Molec. Biomolec. Spectr.* **2008,** *71* (4), 1438-1445.
207. Jakobi, G.; Fabian, P., Indoor/outdoor concentrations of ozone and peroxyacetyl nitrate (PAN). *International Journal of Biometeorology* **1997,** *40* (3), 162-165.
208. Bulatov, V.; Reany, O.; Grinko, R.; Schechter, I.; Keinan, E., Time-resolved, laser initiated detonation of TATP supports the previously predicted non-redox mechanism. *Physical Chemistry Chemical Physics* **2013,** *15* (16), 6041-6048.
209. Burks, R. M.; Hage, D. S., Current trends in the detection of peroxide-based explosives. *Analytical and Bioanalytical Chemistry* **2009,** *395* (2), 301-313.
210. Capua, E.; Cao, R.; Sukenik, C. N.; Naaman, R., Detection of triacetone triperoxide (TATP) with an array of sensors based on non-specific interactions. *Sensors and Actuators B: Chemical* **2009,** *140* (1), 122-127.
211. Shen, C.; Li, J.; Han, H.; Wang, H.; Jiang, H.; Chu, Y., Triacetone triperoxide detection using low reduced-field proton transfer reaction mass spectrometer. *International Journal of Mass Spectrometry* **2009,** *285* (1), 100-103.

212. Wilson, P. F.; Prince, B. J.; McEwan, M. J., Application of Selected-Ion Flow Tube Mass Spectrometry to the Real-Time Detection of Triacetone Triperoxide. *Analytical Chemistry* **2006,** *78* (2), 575-579.
213. Oxley, J.; Smith, J.; Brady, J.; Dubnikova, F.; Kosloff, R.; Zeiri, L.; Zeiri, Y., Raman and infrared fingerprint spectroscopy of peroxide-based explosives. *Applied Spectroscopy* **2008,** *62* (8), 906-915.
214. Sigman, M. E.; Clark, C. D.; Caiano, T.; Mullen, R., Analysis of triacetone triperoxide (TATP) and TATP synthetic intermediates by electrospray ionization mass spectrometry. *Rapid communications in mass spectrometry : RCM* **2008,** *22* (2), 84-90.
215. Kende, A.; Lebics, F.; Eke, Z.; Torkos, K., Trace level triacetone-triperoxide identification with SPME-GC-MS in model systems. *Microchimica Acta* **2008,** *163* (3-4), 335-338.
216. Cotte-Rodriguez, I.; Chen, H.; Cooks, R. G., Rapid trace detection of triacetone triperoxide (TATP) by complexation reactions during desorption electrospray ionization. *Chemical Communications* **2006,** (9), 953-955.
217. Yamaguchi, S.; Uchimura, T.; Imasaka, T.; Imasaka, T., Gas chromatography/time-of-flight mass spectrometry of triacetone triperoxide based on femtosecond laser ionization. *Rapid Communications in Mass Spectrometry* **2009,** *23* (19), 3101-3106.
218. Almond, M. J.; Becerra, R.; Bowes, S. J.; Cannady, J. P.; Ogden, J. S.; Walsh, R., A mechanistic study of cyclic siloxane pyrolyses at low pressures. *Physical Chemistry Chemical Physics* **2008,** *10* (45), 6856-6861.
219. Davidson, I. M.; Thompson, J. F., DIMETHYLSILANONE FROM PYROLYSIS OF OCTAMETHYLCYCLOTETRASILOXANE. *Journal of the Chemical Society D-Chemical Communications* **1971,** (6), 251-&.
220. Kulyk, K.; Zettergren, H.; Gatchell, M.; Alexander, J. D.; Borysenko, M.; Palianytsia, B.; Larsson, M.; Kulik, T., Dimethylsilanone Generation from Pyrolysis of Polysiloxanes Filled with Nanosized Silica and Ceria/Silica. *Chempluschem* **2016,** *81* (9), 1003-1013.
221. Rucker, C.; Kummerer, K., Environmental Chemistry of Organosiloxanes. *Chemical Reviews* **2015,** *115* (1), 466-524.